Rotary ultrasonic machining of difficult-to-machine materials: experimental and theoretical investigations

by

Palamandadige Fernando

B.S., University of Colombo, 2009
B.Tech., The Open University of Sri Lanka, 2010

AN ABSTRACT OF A DISSERTATION

submitted in partial fulfillment of the requirements for the degree

DOCTOR OF PHILOSOPHY

Department of Industrial & Manufacturing Systems Engineering
Carl R. Ice College of Engineering

KANSAS STATE UNIVERSITY
Manhattan, Kansas

2020

Abstract

High-performance materials such as composite materials, metal alloys, and advanced ceramics are attractive to engineering applications in aerospace, automobile and sport industries. Materials with superior properties are often difficult-to-machine due to their high strength, high hardness, and high toughness, which make the cutting force and temperature at the cutting interface very high and result to a short tool life. This limits their market expansion due to the high cost of machining with current machining procedures. However, the demand for high-performance materials is increasing in certain industries such as aerospace and automotive. In addition to machining of high performance materials, some of the conventional materials such as rocks also can be categorized into difficult-to-machine materials. Some causes which made rock drilling complicated are expose to several rock types in a single drilling, an infinite variability of rock properties, relatively high hardness and high abrasiveness of rocks, friction between rock and tool, severe wear and damage to tools etc. Therefore, it is crucial to develop more cost-effective machining processes for difficult-to-machine materials.

Rotary ultrasonic machining (RUM), a hybrid non-traditional machining process combining the material removal mechanisms of abrasive grinding and ultrasonic machining, has the potential for low-cost and high quality machining of difficult-to-machine materials. Researchers have shown that RUM can attain a higher material removal rate than both ultrasonic machining (USM) and grinding. RUM can also drill deep holes with high accuracy, improved surface finish, and low cutting force and torque.

The objectives of this research are to investigate the relationships between input variables and output variables of RUM of difficult-to-machine materials, to study the measurement methods

of ultrasonic vibration amplitude and the effects of tool natural frequency on ultrasonic vibration amplitude, and to model RUM of rocks.

In this dissertation, research has been conducted by experimental, numerical, and theoretical investigations on output variables including cutting force, torque, surface roughness, edge chipping, and delamination. The goal of this research is to provide new knowledge based on machining difficult-to-machine materials on RUM in order to improve the quality of the machined holes while decreasing the machining cost and to study the effects of machining variables (feedrate, tool rotation speed, and ultrasonic power) and tool variables (abrasive size and concentration, tool diameter, and tool geometry) on output variables.

This dissertation firstly provides the introduction to difficult-to-machine materials and rotary ultrasonic machining. After that Chapter 2 investigates the effects of input variables on cutting force, torque, and surface roughness, and study the effects of machining variables, tool end angle, and the use of a backing plate on the delamination of RUM of CFRP. Chapter 3 studies the comparison between intermittent RUM and continuous RUM when machining K9 glass from the perspectives of cutting force, surface roughness, and chipping size. Chapter 4 investigates the effects of input variables on cutting force, torque, surface roughness, and edge chipping of the RUM of basalt, travertine, and marble, and development of a mechanistic predictive cutting force model for RUM of rocks based on the ductile mode removal and brittle fracture mode removal of rock under the indentation of a single abrasive particle. Chapter 5 discusses the effects of tool natural frequency on ultrasonic vibration amplitude. Finally, conclusions and contributions on RUM drilling are discussed in Chapter 6.

Rotary ultrasonic machining of difficult-to-machine materials: experimental and theoretical investigations

by

Palamandadige Fernando

B.S., University of Colombo, 2009
B.Tech., The Open University of Sri Lanka, 2010

A DISSERTATION

submitted in partial fulfillment of the requirements for the degree

DOCTOR OF PHILOSOPHY

Department of Industrial & Manufacturing Systems Engineering
Carl R. Ice College of Engineering

KANSAS STATE UNIVERSITY
Manhattan, Kansas

2020

Approved by:

Co-major Professor
Dr. Meng Zhang

Approved by:

Co-major Professor
Dr. Zhijian Pei

Copyright

Abstract

High-performance materials such as composite materials, metal alloys, and advanced ceramics are attractive to engineering applications in aerospace, automobile and sport industries. Materials with superior properties are often difficult-to-machine due to their high strength, high hardness, and high toughness, which make the cutting force and temperature at the cutting interface very high and result to a short tool life. This limits their market expansion due to the high cost of machining with current machining procedures. However, the demand for high-performance materials is increasing in certain industries such as aerospace and automotive. In addition to machining of high performance materials, some of the conventional materials such as rocks also can be categorized into difficult-to-machine materials. Some causes which made rock drilling complicated are expose to several rock types in a single drilling, an infinite variability of rock properties, relatively high hardness and high abrasiveness of rocks, friction between rock and tool, severe wear and damage to tools etc. Therefore, it is crucial to develop more cost-effective machining processes for difficult-to-machine materials.

Rotary ultrasonic machining (RUM), a hybrid non-traditional machining process combining the material removal mechanisms of abrasive grinding and ultrasonic machining, has the potential for low-cost and high quality machining of difficult-to-machine materials. Researchers have shown that RUM can attain a higher material removal rate than both ultrasonic machining (USM) and grinding. RUM can also drill deep holes with high accuracy, improved surface finish, and low cutting force and torque.

The objectives of this research are to investigate the relationships between input variables and output variables of RUM of difficult-to-machine materials, to study the measurement methods

of ultrasonic vibration amplitude and the effects of tool natural frequency on ultrasonic vibration amplitude, and to model RUM of rocks.

In this dissertation, research has been conducted by experimental, numerical, and theoretical investigations on output variables including cutting force, torque, surface roughness, edge chipping, and delamination. The goal of this research is to provide new knowledge based on machining difficult-to-machine materials on RUM in order to improve the quality of the machined holes while decreasing the machining cost and to study the effects of machining variables (feedrate, tool rotation speed, and ultrasonic power) and tool variables (abrasive size and concentration, tool diameter, and tool geometry) on output variables.

This dissertation firstly provides the introduction to difficult-to-machine materials and rotary ultrasonic machining. After that Chapter 2 investigates the effects of input variables on cutting force, torque, and surface roughness, and study the effects of machining variables, tool end angle, and the use of a backing plate on the delamination of RUM of CFRP. Chapter 3 studies the comparison between intermittent RUM and continuous RUM when machining K9 glass from the perspectives of cutting force, surface roughness, and chipping size. Chapter 4 investigates the effects of input variables on cutting force, torque, surface roughness, and edge chipping of the RUM of basalt, travertine, and marble, and development of a mechanistic predictive cutting force model for RUM of rocks based on the ductile mode removal and brittle fracture mode removal of rock under the indentation of a single abrasive particle. Chapter 5 discusses the effects of tool natural frequency on ultrasonic vibration amplitude. Finally, conclusions and contributions on RUM drilling are discussed in Chapter 6.

Table of Contents

List of Figures

List of Tables

Acknowledgements

First, I would like to express my sincere gratitude to my co-major research advisors, Dr. Meng Zhang and D. ZJ Pei, for their incredible support, guidance, and encouragement throughout my Ph.D. I am very grateful to them for their contributions of time to discuss research questions, sharing their immense knowledge, experience, patience and suggestions with positive deposition. Their strict attitude on research and guidance inspired me all the time in research and my personal life to improve day by day. I could not have imagined having better advisors for my Ph.D. study.

Besides my advisors, I would also like to thank my committee members, Dr. Shuting Lei, Dr. Gurpreet Singh, and outside chairperson Dr. Andrew Ivanov for their valuable time to serve as my committee members and for their insightful comments and suggestions. I really appreciate the help from Dr. Weilong Cong especially at the beginning of my Ph.D. research career and his valuable comments, encouragement, and suggestions.

I would really appreciate the encouragement and help from the head of the department, Dr. Bradley A. Kramer and all the faculty and staff members in the Department of Industrial and Manufacturing Systems Engineering.

I would like to thank Dr. Christopher Jones (Department of Civil Engineering at Kansas State University) for his assistance with nano-dynamic mechanical analysis and my collaborators: Dr. Weilong Cong and Mr. Hui Wang, Texas Tech University; Dr. Fuda Ning, Binghamton University.

I also extend my thank to both present and past group members, Dr. Xiaoxu Song, Yang Yang, Mingman Sun, Qianqian Nie, and undergrad researcher Adam Owens, for their help and support.

Lastly, but certainly not least, I would like to thank very much my wonderful family. It is hard to express my sincere gratitude in words for my ever loving parents and sister for their unconditional love, support and encouragement in every time in my life. I am forever indebted to you for giving me life, your love and for molding me the person who I am today. I am so grateful to my ever loving wife for her constant love, patience, sacrifices and faithful support throughout last nine years. She has given me the confidence, made me much stronger and motivated and being by my side every good and bad time. I have been extremely fortunate to have her in my life for this journey. Finally, I would like to thank our little bundle of joy, Savin who brought us all the happiness in the world and completing our life.

Dedication

To my son

Savin Ranuga Fernando

To my parents

T.G.H Fernando and P. Hector Fernando

To my sister

P.N.S Fernando

To my wife

Aruni P. Malalasekera

Chapter 1 - Introduction

High-performance materials such as composite materials, metal alloys, and advanced ceramics are attractive to engineering applications in aerospace, automobile and sport industries due to their superior properties such as high strength and stiffness, high toughness and fatigue strength, resistance to creep, wear, and corrosion, and low density. However, there exist considerable impediments to the market expansion of high-performance materials. One of the primary impediments is the high cost of machining due to the difficulty of machining with traditional machining technologies such as twist drilling. In addition to machining of high performance materials, some of the conventional materials such as rocks also can be categorized into difficult-to-machine materials. Therefore, it is crucial to develop more cost-effective machining processes for difficult-to-machine materials. In this chapter, importance of introducing cost-effective machining procedures for difficult-to-machine materials and an introduction of workpiece materials are discussed first. Secondly, rotary ultrasonic machining is described as a promising machining process for many difficult-to-machine materials. Finally, the dissertation outline will be presented.

1.1 Importance of introducing cost-effective machining procedures for difficult-to-machine materials

Present material development is approaching the molecular or atomic level and the ability to achieve advanced analytical and computational techniques has enabled the investigations on material properties to a new level. This allows to develop materials with excellent performances in one or a few areas which cannot be attained from conventional materials. High-performance materials are used in a vast range of applications where conventional materials cannot succeed

such as in the manufacturing of lightweight aerospace structural parts by using composite materials, the making of turbine blades to withstand the high heat and stresses at extreme temperatures by using nickel-based alloys, etc.

Today's manufacturing market demands stronger, lighter, and safer materials for their advanced innovative applications. Fiber reinforced composites are one example that allow many of these challenges to be met. In 2014, the global composite materials market was about $28 billion and its growth rate was between 15 - 20% per year [1]. In 2016, the United States exported composites worth approximately $2.5 billion and $2.7 billion worth of exports in 2018 [2]. The demand for composite materials is increasing due to the emerging trends such as the development of low-cost carbon fibers and high-performance glass fibers [2]. Advanced carbon fiber composites are more expensive than most of the metals because of the high cost of carbon fibers [1]. However, industrial grade carbon fibers are expected to cost $10/kg by 2020. As a result, the current market for carbon fibers in non-aerospace applications is increasing at a rapid rate, especially in sports, marine, and transportation industry [1].

The improvement of the efficiency of energy converting technologies in the power plant and aviation industries are in need of high-performance materials with excellent heat and corrosion resistance to meet the future demands. Nickel-based alloys can meet these challenges to a large extent and have been widely applied in aircraft engine parts, the construction of nuclear reactors, and hot-end components of various types of gas turbines [3-5]. Rolls-Royce Civil Aerospace, one of the largest jet engine manufacturers, predicted that the global market will require 149,000 engines over the 20-year period of 2012-2031 [5]. Typically, nickel-based superalloys account for 40-50% of the total weight of an aircraft engine [5]. Therefore, this will increase the demand for nickel-based superalloys in this industrial application. Furthermore, the expected carbon emission

reduction and improvement in the fuel efficiency of jet engines will also drive the demand for nickel-based superalloys [5]. The International Energy Agency published the projection of global energy consumption to 2030, which indicates the significant growth of the use of natural gas and nuclear power to meet the global energy demand [5]. In turbine generators, it is required to increase the steam temperature to as high as 700 °C to achieve higher efficiency. This high-temperature operation requires high-performance materials such as nickel-based superalloys. Moreover, nickel-based superalloys are progressively finding applications in the oil, gas, and marine sectors because of their resistance to degradation in corrosive or oxidizing environments [4, 5]. These facts indicate that there is a higher demand for nickel-based superalloys in the manufacturing of aircraft engines, power generation, and marine propulsion.

The first, second, and third generations of superalloys have been developed. Second and third-generation superalloys contain expensive alloying materials such as rhenium [5]. The latest generations of super alloys contain either rhenium or ruthenium, or both [5]. For example, Rene' N6 third-generation superalloys contains only rhenium and TMS 162 fifth-generation single crystal alloy contains both rhenium and ruthenium [5]. These alloys were designed to increase the resistance to high heat and to have higher creep resistance, and are used only in specialized applications [5]. The latest generations of superalloys have an increasing demand for special applications such as applications in high speed civil transportation, when the cost is not a constraint [6].

Materials with superior properties are often difficult-to-machine due to their high strength, high hardness, and high toughness, which make the cutting force and temperature at the cutting interface very high and result to a short tool life. This limits their market expansion due to the high cost of machining with current machining procedures. However, the demand for high-performance

materials is increasing in certain industries such as aerospace and automotive. Therefore, cost effective machining procedures are essential for those industries to fulfill the current demand on high-performance materials to make better quality products.

Besides the machining of high-performance materials, there are some conventional materials that can be classified into difficult-to-machine materials. For an example, rock drilling is a still challenging geoengineering practice to investigate ground and extraterrestrial subsurfaces. Some causes which made rock drilling complicated are expose to several rock types in a single drilling, an infinite variability of rock properties, relatively high hardness and high abrasiveness of rocks, friction between rock and tool, severe wear and damage to tools etc. [7, 8]. Recent research developments are basically focused on these problems, especially on finding better materials and designs for tools to avoid tool damage and wear [9 - 13]. Fewer investigations can be found in the literature which were introducing different drilling procedures to exist ones [14]. Therefore, it is also crucial to develop more cost-effective machining processes for conventional materials, which can be categorized as difficult-to-machine materials.

1.2 Workpiece materials and their drilling methods

1.2.1 Carbon fiber reinforced plastic (CFRP) composite

A composite is a material made of two or more materials that have significantly different physical and chemical properties that, when combined, produce a composite material with a properties different from each constituent. Composite materials can be classified into three categories, according to the matrix materials: polymer matrix composites (PMC), metal matrix composites (MMC), and ceramic matrix composites (CMC). There are three common types of reinforcements used in PMC. They are glass, carbon, and aramid fibers. Glass fiber reinforced

plastics (GFRP) are the most commonly used composite material. Carbon fiber reinforced plastics (CFRP) are used where high specific strength, high specific stiffness and light weight are the major considerations. Two types of commonly used composites are carbon fiber and glass fiber composites [2]. Carbon and glass fibers are strong and lightweight but glass fiber is more flexible than carbon fiber [2]. Therefore, carbon fiber reinforced plastics are having a wide range of engineering applications to replace steel and aluminum [2]. CFRP shows the following superior properties: lower density than aluminum, higher strength than high-strength metals, higher stiffness than titanium, high toughness, high fatigue strength, small friction coefficient, resistance to creep, wear and corrosion, high dimensional stability, and a vibration damping ability [3, 6, 16-21].

The fast evolution of composite materials offers numerous opportunities to a wide range of industries to consider new product designs [22]. Aircraft, automobile, and sport industries have a growing interest in increasing the usage of composite materials in their products [17-21, 23, 24]. As an example, Boeing 787 uses 50% by volume of advanced composite materials, which is greater than any other commercial airplanes Boeing built [18].

Since composite materials are heterogeneous and anisotropic, conventional machining procedures are neither efficient nor cost-effective for machining composite materials [22, 24-29]. Therefore, more efficient, cost-effective, and better quality machining processes are required to satisfy the growing demand for composite materials [22, 30-34]. Non-traditional machining technologies such as laser and abrasive waterjet can machine composite materials efficiently [25]. However, these technologies are associated with machining defects [35]. Abrasive penetration, fiber pull-out, and delamination are some of the defects associated with waterjet technology [35].

The major machining defect in laser technology is the occurrence of heat affected zones in the workpiece [35].

1.2.2 K9 glass

K9 glass, also known as BK7 or borosilicate crown glass, has excellent optical performance due to its bubble-free structure and low inclusions [36]. K9 glass has been used as a representative functional material in many applications, such as optics, electronics, thermodynamics, fluidics, etc. [36]. K9 glass is regarded as a difficult-to-machine material due to its mechanical properties, such as high hardness, high strength, and low fracture toughness [38]. Other material properties that give K9 glass a broad application include its low density, high thermal resistance, and high resistance to corrosion and wear.

Some material processing techniques have been investigated with the machining of K9 glass. Gu et al. used a diamond grinding wheel to study four grinding modes in the horizontal surface grinding of K9 glass: brittle mode, semi-brittle mode, semi-ductile mode, and ductile mode [39]. Park et al. investigated the micro-machining of K9 glass by using micro-abrasives, which were accelerated by compressed air to form linear grooves and holes with a width and diameter of 80 μm [40]. Matsumura et al. reported the use of abrasive water jet to make grooves of 20–100 μm wide in glass [41].

1.2.3 Rocks

There are three main categories of rocks: sedimentary, metamorphic, and igneous. Rock types can be divided again into two groups based on grain size and the types of the rock minerals. The first group includes calcite, magnetite, hematite, sandstone and quartz with an isotropic

character, and the other group consist with complex or multi mineral rocks, including granite, granulite and mica schist. In this dissertation, three types of rocks were chosen from each category. They were basalt (high strength) from the igneous category, marble (medium strength) from the metamorphic category, and travertine (low strength) from the sedimentary category.

Rock drilling is widely used to explore and mine energy resources. It has also been used to extract samples to study the earth's geological composition and topography and to explore different planets. Uniaxial compressive strength, rock hardness, texture and grain size, joint spacing, joint dipping, joint aperture and filling, and brittleness are geological properties which influence the drillability of rock masses [42]. The main rock drilling methods are rotary non-percussive drilling and percussive drilling [43]. Percussive drilling is, as of today, the most commonly used rock drilling method. Since the 1950s, many researchers have performed drillability studies on diamond drilling [44]. Impregnated diamond core drilling is a dominant technique used in the advanced stages of mineral exploration [45]. High-frequency torsional impact drilling (HFTID) is the newest impact drilling technique, which is designed to deliver incremental energy to the drill bit and to increase the rate of penetration [46]. Due to the high hardness and abrasiveness of rock, the tool wear in rock drilling is severe, thus limiting its penetration rate and resulting in a high cost to operate. Therefore, it is crucial to develop more cost-effective rock drilling processes.

1.2.4 Titanium alloys

Titanium and its alloys are attractive for many engineering applications due to their high specific strength and excellent corrosion resistance with a lower density compared to steels and nickel-based superalloys [47]. This explains the early success of titanium and its alloys in the

aerospace and chemical industries [47-49]. Today, titanium and its alloys have expanded into many industries such as military, architecture, medicine, power generation, marine, sports and leisure, and transportation [47, 50-59]. More than 10% of the worldwide consumption of titanium is accounted by the sporting goods industry due to the higher rate of production than any other industry that uses titanium and its alloys [47].

Titanium alloys possess attractive superior properties such as its low density (~3.9-4.1 gcm^{-3}), high specific yield strength, high specific stiffness, high oxidation resistance, and better creep properties at high temperatures [47, 56, 58]. These superior properties of titanium and its alloys make them difficult-to-machine materials. For example, the lower thermal conductivity of titanium obstructs the heat dissipation at the cutting zone, which increases the wear of the cutting tools, its lower modulus of elasticity leads to significant spring-back of the titanium workpiece, which causes the workpiece to move away from the cutting tool, and the lower hardness and high chemical reactivity of titanium can affect the galling of the titanium with the cutting tool [47].

Due to the aforementioned reasons, the drilling of titanium and its alloys usually has high cost and low efficiency with conventional drilling methods. The cutting tool for drilling titanium and its alloys preferably should be high-speed cobalt-containing steel with a short cutting length [47]. To avoid excessive friction and to keep the cutting interface cool, lower cutting speeds are preferred with a constant supply of chlorinated cutting fluid [47].

1.3 Introduction of rotary ultrasonic machining

In 1964, rotary ultrasonic machining (RUM) was invented by Percy Legge, who was a technical officer at United Kingdom Atomic Energy Authority [60, 61]. RUM is a hybrid machining process that combines the material removal mechanisms of diamond abrasive grinding

and ultrasonic machining. Rotary ultrasonic machining has been applied to hole-making for a wide range of materials including titanium, carbon fiber reinforced plastics (CFRP), and advanced ceramics [62-67]. RUM provides a lower cutting force compared to that of conventional hole-making processes, as well as many other advantages [68]. The material removal rate (MRR) of RUM is 6-10 times higher than that of ultrasonic machining (USM) [68-70]. RUM can drill small, deep holes with a high hole accuracy, low cutting force, low machining temperature, low surface roughness, and long tool life [70-72].

In RUM, a rotating cutting tool with metal-bonded diamond abrasive particles vibrates at an ultrasonic frequency (e.g., 20 kHz) in the axial direction and is fed towards the workpiece at a constant feedrate to remove material. Figure 1.1 shows a schematic of RUM. Coolant is pumped through the core of the tool to the cutting interface to flush away the removed material, keep the tool cool, and prevent the tool from jamming.

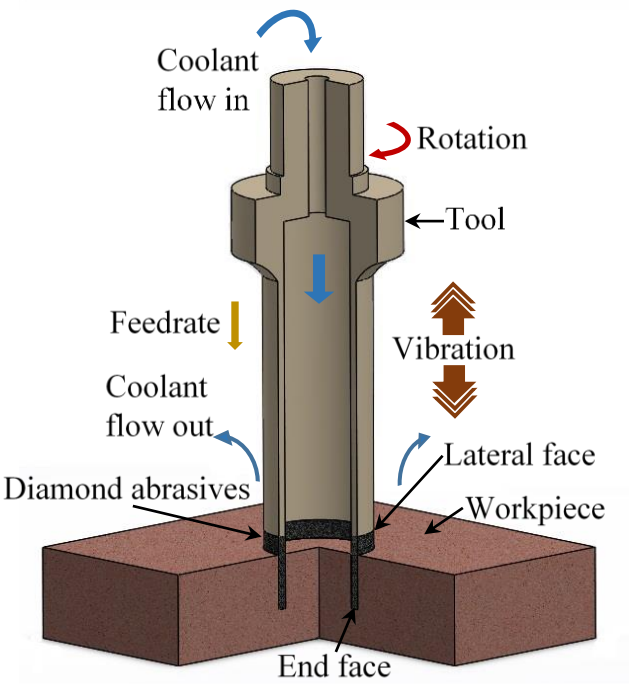

Figure 1.1 A schematic of rotary ultrasonic machining

1.4 Purpose of the research and dissertation outline

The first objective of this research is to generate understanding and to provide new knowledge on drilling difficult-to-machine materials such as carbon fiber reinforced plastics, K9 glass, and rocks (basalt, travertine, and marble) using rotary ultrasonic machining. The second objective of this research is to investigate the effects of the tool natural frequency on the ultrasonic vibration amplitude. The specific research tasks of this dissertation are as follows:

1. RUM of CFRP: To study the effects of input variables on cutting force, torque, and surface roughness, and to study the effects of machining variables, tool end angle, and the use of a backing plate on delamination of RUM of CFRP.
2. RUM of K9 glass: To compare intermittent RUM and continuous RUM when machining K9 glass from the perspectives of cutting force, surface roughness, and chipping size.
3. RUM of rocks: To study the effects of input variables on cutting force, torque, surface roughness, and edge chipping, to investigate the feasible cutting regions of the RUM of basalt, and to develop a mechanistic predictive cutting force for the RUM of rocks.
4. To provide an explanation to the observation, different tools show different vibration amplitudes on the same ultrasonic power level, and verification of measurement methods, and also to guide tool design and selection in RUM.

This dissertation firstly provides an introduction to difficult-to-machine materials and rotary ultrasonic machining. After that Chapter 2 investigates the effects of input variables on cutting force, torque, and surface roughness, and study the effects of machining variables, tool end angle, and the use of a backing plate on the delamination of RUM of CFRP. Chapter 3 studies the

comparison between intermittent RUM and continuous RUM when machining K9 glass from the perspectives of cutting force, surface roughness, and chipping size. Chapter 4 investigates the effects of input variables on cutting force, torque, surface roughness, and edge chipping of the RUM of basalt, travertine, and marble, and development of a mechanistic predictive cutting force model for RUM of rocks based on the ductile mode removal and brittle fracture mode removal of rock under the indentation of a single abrasive particle. Chapter 5 discusses the effects of tool natural frequency on ultrasonic vibration amplitude. Finally, conclusions and contributions on RUM drilling are discussed in Chapter 6.

References

[1]. Shama Rao, N., Simha T.G.A., Rao, K.P., Ravi Kumar, G.V.V., 2018, "Carbon composites are becoming competitive and cost effective," Infosys Limited, pp. 1-12.

[2]. 2017, "2017 top markets report composites," U.S. Department of Commerce, pp. 1-4.

[3]. Uhlmann, E., Kaulfersch, F., Roeder, M., 2014, "Turning of high-performance materials with rotating indexable inserts," Procedia CIRP, Vol. 14, pp. 610-615.

[4]. Zhu, D., Zhang, X., Ding, H., 2013, "Tool wear characteristics in machining of nickel-based superalloys," International Journal of Machine Tools and Manufacture, Vol. 64, pp. 60.

[5]. INSG, 2013, "Nickel-based superalloys," INSG Secretariat Briefing Paper, Vol. 20, pp 1-9.

[6]. Walston, S., Cetel, A., MacKay, R., O'Hara, K., Duhl, D., Dreshfield, R., 2004, "Joint development of a fourth-generation single crystal superalloy," NASA Scientific and Technical Information Program, pp. 1-17.

[7]. K. McGregor, 1967, "The drilling of rock," A Maclaren Company, London.

[8]. J.A. Hawk, R.D. Wilson, in: Modern Tribology Handbook, New York, 2001, pp. 1331–1370.

[9]. Beste, U., Jacobson, S., 2008, “A new view of the deterioration and wear of WC-C0 cemented carbide rock drill buttons,” Wear, Vol. 264, pp. 1129 – 1141.

[10]. Clydesdale, G., Leseultre, A., Lamine, E., 1994, “Core bit design reduces mud invasion, improves ROP,” Oil and Gas Journal, Vol. 92, pp. 51 – 57.

[11]. Beste, U., Jacobson, S., Hogmark, S., 2008, “Rock penetration into cemented carbide drill buttons during rock drilling,” Wear, Vol. 264, pp. 1142 – 1151.

[12]. Yang, X., Li, X., Lu, Y., 2011, “Wear characteristics of the cemented carbide blades in drilling limestone with water jet,” International Journal of Refractory Metals and Hard Materials, Vol. 29, pp. 320 – 325.

[13]. Miller, D., Ball, A., 1991, “The wear of dimonds in impregnated diamond bit drilling,” Wear,Vol. 141, pp. 311-320.

[14]. Jiren, T., Yiyu, L., Zhaolong, G., Binwei, X., Huijuan, S., Peng, D., 2014, “A new method of combined rock drilling,” International Journal Mining Science and Technology, Vol. 24, pp. 1 – 6.

[15]. Arul, S., Vijayaraghavan, L., Malhotra, S.K., Krishnamurthy, R., 2006, "The effect of vibratory drilling on hole quality in polymeric composites," International Journal of Machine Tool & Manufacture, Vol. 46, pp. 252-259.

[16]. Wang, X., Kwon, P.Y., Sturtevant, C., Kim, D., Lantrip, J., 2013, "Tool wear of coated drills in drilling CFRP," Journal of Manufacturing Processes, Vol. 15, pp. 127-135.

[17]. Cong, W.L., Pei, Z.J., Feng, Q., Deines, T.W., Treadwell, C., 2012, "Rotary ultrasonic machining of CFRP: A comparison with twist drilling," Journal of Reinforced Plastics and Composites, Vol. 31, Issue 5, pp. 313-321.

[18]. Boeing Co, 787 Dreamliner Program Fact Sheet, 2011. <http://www.boeing.com/commercial/787family/ programfacts.page?> accessed July 22nd 2014.

[19]. Guu, Y.H., Hocheng, H., Tai, N.H., Liu, S.Y., 2001, "Effect of electrical discharge machining on the characteristics of carbon fiber reinforced carbon composites," Journal of Materials Science, Vol. 36, pp. 2037-2043.

[20]. Hu, S., Hoa, S.V., Ganesan, R., 2009, "A new evaluation method for surface finish of composite automotive panels using waveform analysis," Journal of Composite Materials, Vol. 43, pp. 843-875.

[21]. Liu, Y., Kumar., S., 2012, "Recent progress in fabrication, structure, and properties of carbon fiber," Polymer Reviews, Vol. 52, pp. 234-258.

[22]. Teti, R., 2002, "Machining of Composite materials," CIRP Annals-Manufacturing Technology, Vol. 51, pp. 611-634.

[23]. Stone, R., Krishnamurthy, K., 1996, "A neural network thrust force controller to minimize delamination during of graphite-epoxy laminates," International Journal of Machine Tools & Manufacture, Vol. 36, pp. 985-1003.

[24]. Upadhyay, P.C., Lyons, J.S., 1999, "On the evaluation of critical thrust for delamination-free drilling of composite laminates," Journal of Reinforced Plastics and Composites, Vol. 18, pp. 1287-1303.

[25]. Davim, J.P., Reis, P., 2003, "Drilling carbon fiber reinforced plastics manufactured by autoclave experimental and statistical study," Materials and Design, Vol. 24, pp. 315-324.

[26]. Gaitonde, V.N., Karnik, S.R., Rubio, J.C., Correia, A.E., Abrao, A.M., 2008, "Analysis of parametric influence on delamination in high-speed drilling of carbon fiber reinforced plastic composites," Journal of Materials Processing Technology, Vol. 203, pp. 431-438.

[27]. Faraz, A., Heymann, T., Biermann, D., 2011, "Experimental investigations on drilling GFRP epoxy composite laminates using specialized and conventional uncoated cemented carbide drills," Vol. 26, pp. 609-617.

[28]. Gaitonde, V.N., Karnik, S.R., Rubio, J.C., Correia, A.E., Abrao, A.M., Davim, P.J., 2011, "A study aimed at minimizing delamination during drilling of CFRP composites," Journal of Composite Materials, Vol. 45, pp. 2359-2368.

[29]. Cheng, H., Dharan, C.K.H., 1990, "Delamination during drilling in composite laminates," Journal of Engineering for Industry, Vol. 112, pp. 236-239.

[30]. Jain, S., Yang, D.C.H, 1993, "Effects of feedrate and chisel edge on delamination in composites drilling," Journal of Engineering for Industry, Vol. 115, pp. 398-405.

[31]. Jain, S., Yang, D.C.H, 1994, "Delamination free drilling of composite laminates," Journal of Engineering for Industry, Vol. 116, pp. 475-481.

[32]. Park, K.Y., Choi, J.H., Lee, D.G., 1995, "Delamination-free and high-efficiency drilling of CFRP," Vol. 29, pp. 1988-2002.

[33]. Piquet, R., Ferret, B., Lachaud, F., Swider, P., 2000, "Experimental analysis of drilling damage in thin carbon-epoxy plate using special drills," Composites, Vol. 31, pp. 1107-1115.

[34]. Salama, A., Li, L., Mativenga, P., Sabli, A., 2016, “High-power picosecond laser drilling/machining of carbon fiber-reinforced polymer (CFRP) composites,” Applied Physics A, Vol. 122.

[35]. Zhao, K., Jia, Z., Liu, W., Ma, J., Wang, L., 2015, “Material removal with constant depth in CNC laser milling based on adaptive control of laser fluence,” International Journal of Advanced Manufacturing Technology, Vol. 77, pp. 797-806.

[36]. Gu, W., Yao, Z., 2011, “Evaluation of surface cracking in micron and sub-micron scale scratch tests for optical glass BK7,” Journal of Mechanical Science and Technology, Vol. 25, pp. 1167-1174.

[37]. Choi, J., Jeon, B., Kim, B., 2007, “Chemical-assisted ultrasonic machining of glass,” Journal of Materials Processing Technology, Vol. 19, pp. 153-156.

[38]. Zhang, C., Cong, W., Feng, P., Pei, Z.J., 2014, “Rotary ultrasonic machining of optical K9 glass using compressed air as coolant: A feasibility study,” Processing Institute of Mechanical Engineers, Vol. 228, pp. 504-514.

[39]. Gu, W., Yao, Z., Li, H., 2011, “Investigation of grinding modes in horizontal surface grinding of optical glass BK7,” Journal of Materials Processing, Vol. 211, pp. 1629-1636.

[40]. Park, D., Cho, M., Lee, H., Cho, W., 2004, “Micro-grooving of glass using micro-abrasive jet machining,” Journal of Materials Processing Technology, Vol. 146, pp. 234-240.

[41]. Matsumura, T., Muramatsu, T., Fueki, S., 2011, “Abrasive water jet machining of glass with stagnation effect,” CIRP Annals-Manufacturing Technology, Vol. 60, pp. 355-358.

[42]. Saeidi, O., Torabi, S.R., Ataei, M., 2013, “Development of a New Index to Assess the Rock Mass Drillability,” Geo-Technology and Geology Engineering, Vol. 31, pp. 1477-1495.

[43]. Teale, R., 1965, “The concept of specific energy in rock drilling,” International Journal of Rock Mechanics and Mining Sciences and Geomechanics, Vol. 2, pp. 57-73.

[44]. Huang, S.L., Wang, Z.W., 1997, "The mechanics of diamond core drilling of rocks," International Journal of Rock Mechanics and Mining Sciences, Vol. 34, paper No. 134.

[45]. Karakus, M., Perez, S., 2013, "Acoustic emission analysis for rock–bit interactions in impregnated diamond core drilling," International Journal of Rock Mechanics & Mining Sciences, Vol. 68, pp. 36-43.

[46]. Zhu, X., Tang, L., Tong, H., 2014, "Effects of High-Frequency Torsional Impacts on Rock Drilling," Rock Mechanics and Rock Engineering, Vol. 47, pp. 1345-1354.

[47]. Leyens, C., Peters, M., 2003, "Titanium and titanium alloys," Fundamentals and Applications.

[48]. Boyer, R.R., 1996, "Overview on the use of titanium in the aerospace industry," Materials Science and Engineering A: Structure Materials, Properties, Microstructure, and Processing, Vol. 213, pp. 103-114.

[49]. Peacock, D., 1988, "Aerospace applications for titanium," Sheet Metal Industries, Vol. 65, pp. 406-408.

[50]. Montgomery, J., Wells, M., 2001, "Titanium armor applications in combat vehicles," Journal of the Minerals, Metals, and Materials Society, Vol. 53, pp. 29-32.

[51]. Lerner, I., 2004, "Titanium market recovering on commercial military aircraft," Chemical Market Reporter, Vol. 266, pp. 17.

[52]. Yamashita, Y., Takayama, I., Fujii, H., Yamazaki, T., 2002, "Applications and features of titanium for automotive industry," Nippon Steel Technical Report, Vol. 85, pp. 1-4.

[53]. Wilhelm, M., 1993, "Material used in automobile manufacturing - current state and perspectives," Le Journal de Physique IV, Vol. 3, pp 31-40.

[54]. Farthing, T.W., 1979, "Application of titanium in the chemical industry," Chemical Age of India, Vol. 30, pp. 151-166.

[55]. Orr, N.H., 1982, “Industrial application of titanium in the metallurgical industries and chemical industries,” Light Metals, pp. 1149-1156.

[56]. Froes, F.H., 2002, “Titanium sport and medical application focus,” Materials Technology, Vol. 17, pp. 4-7.

[57]. Abdullin, I., Bagautdinov, A., Ibragimov, G., 1988, “Improving surface finish for titanium alloy medical instruments,” Biomedical Engineering, Vol. 22, pp 48-50.

[58]. Yang, X., Richard Liu, C., 1999, “Machining titanium and its alloys,” Machining Science and Technology, Vol. 3, pp. 107-139.

[59]. Ezugwu, E.O., Wang, Z.M., 1997, “Titanium alloys and their machinability – a review,” Journal of Materials Processing Technology, Vol. 68, pp 262-274.

[60]. Patents Licensing Office, Ukaea, 1966, “Universal ultrasonic machine tool for glass and ceramics,” Vacuum, Vol. 16, pp. 210.

[61]. Legge, P., 1964, “Ultrasonic drilling of ceramics,” Ultrasonics, Vol. 2, pp. 20.

[62]. Churi, N.J., Pei, Z.J., Shorter, D.C., Treadwell, C., 2007, “Rotary ultrasonic machining of silicon carbide: designed experiments,” International Journal of Manufacturing Technology and Management, Vol. 12, pp. 284-298.

[63]. Feng, Q., Cong, W.L., Pei, Z.J., Ren, C.Z., 2012, “Rotary ultrasonic machining of carbon fiber-reinforced polymer: feasibility study,” Machining Science and Technology, Vol. 16, pp. 380-398.

[64]. Jiao, Y., Ping, H., Pei, Z.J., Treadwell, C., 2005, “Rotary ultrasonic machining of ceramics: design of experiments,” International Journal of Manufacturing Technology and Management, Vol. 7, pp. 192-206.

[65]. Cong, W.L., Pei, Z.J., Deines, T., Wang, Q.G., Treadwell, C., 2010, "Rotary ultrasonic machining of stainless steels: empirical study of machining variables," International Journal of Manufacturing Research, Vol. 5, pp. 370-386.

[66]. Wang, Q., Cong, W.L., Pei, Z.J., Gao, H., Kang, R., 2009, "Rotary ultrasonic machining of potassium dihydrogen phosphate (KDL) crystal: an experimental investigation," Journal of Manufacturing Processes, Vol. 11, pp. 66-73.

[67]. Churi, N.J., Pei, Z.J., Shorter, C.J., Treadwell, C., 2009, "Rotary ultrasonic machining of dental ceramics," International Journal of Machining and Machinability of Materials, Vol. 6, pp. 270-284.

[68]. Prabhakar, D., 1992, "Machining advanced ceramic materials using rotary ultrasonic machining process," University of Illinois at Urbana-Champaign, IL, M.S. Thesis.

[69]. Hu, P., Zhang, J.M., Pei, Z.J., Treadwell, C., 2002, "Modeling of material removal rate in rotary ultrasonic machining: designed experiments," Journal of Materials Processing Technology, Vol. 129, pp. 339-344.

[70]. Li, Z.C., Jiao, Y., Deines, T.W., Pei, J.J., Treadwell, C., 2005, "Rotary ultrasonic machining of ceramic matrix composites: feasibility study and design experiments," International Journal of Machine Tools and Manufacture, Vol. 45, pp. 1402-1411.

[71]. Jiao, Y., Ping, H., Pei, Z.J., Treadwell, C., 2005, "Rotary ultrasonic machining of ceramics: design of experiments," International Journal of Manufacturing Technology and Management, Vol. 7, pp. 192-206.

[72]. Cleave, D.V., 1976, "Ultrasonics gets bigger jobs in machining and welding," Iron Age, pp. 69-72.

Chapter 2 - CFRP - Design of experiments on cutting force, torque, and surface roughness and study of delamination

2.1 Design of experiments on cutting force, torque, and surface roughness

Paper title:

Rotary ultrasonic machining of carbon fiber reinforced plastics: a design of experiment

Published in:

Proceedings of the ASME 2015 International Manufacturing Science & Engineering Conference (MSEC-2015), June 8-12, 2015, Charlotte, North Carolina, USA

Authors' names:

Fernando, P.[1], Pei, Z.J.[1], Zhang, M.[1], Cong, W.[2], Song, X.[1]

Authors' affiliations:

1. Department of Industrial and Manufacturing Systems Engineering, Kansas State University, Manhattan, KS 66506, USA
2. Department of Industrial Engineering, Texas Tech University, Lubbock, TX 79409, USA

2.1.1 Introduction

Carbon fiber reinforced plastics (CFRP) have a wide-spread engineering applications in aircraft, automobile and sport industries [1,3,4,6,8-11]. As shown in Table 2.1, superior properties of CFRP include lower density than aluminum, higher strength than high-strength metals, higher stiffness than titanium, high toughness and fatigue strength, resistance to creep, wear, and corrosion, small friction coefficient, high dimensional stability and vibration damping ability [2,3,5,7,8, 10,11].

Drilling is an essential practice in industry, especially for the aircraft and aerospace industries where composites are used to build wings, fins, control surfaces, and fuselage panels of aircraft, solar panels, and antennas of satellites. For example, about 10,000 holes must be drilled for the fuselage of Boeing 787 aircraft [10]. Conventional machining procedures such as twist drilling are not sufficiently cost effective for CFRP [11]. Previous research has demonstrated that rotary ultrasonic machining (RUM) can machine CFRP and other hard to machine materials successfully [9,11-21]. In RUM, a rotating, ultrasonically vibrating cutting tool (core drill) feeds to the workpiece to remove the material. A pump provides coolant through the core drill to the cutting interface to flush away the material removed, keep the tool cool and prevent jamming of the cutting tool. Metal-bonded diamond abrasive core drills are used as cutting tools.

This is the first time that reports a study on using design of experiments for RUM of CFRP with two-level three-factor factorial design. In the literature, design of experiment has been used for RUM of other materials, but never for CFRP. In this study, three input variables (ultrasonic power, tool rotation speed, and feedrate) for RUM of CFRP are studied. The design of experiment was used to obtain main effects, two-factor interactions, and three-factor interactions on cutting force, torque, and surface roughness.

Table 2.1 Properties of CFRP

Property	Unit	Value
Density of CFRP	$Kg.m^{-3}$	1550
Hardness (Rockwell) of CFRP	HRB	70-75
Density of carbon fiber	$Kg.m^{-3}$	1800
Elastic modulus of carbon fiber	GPa	230
Tensile strength of carbon fiber	GPa	5
Poisson's ratio of carbon fiber	-	0.3
Fracture toughness of carbon	$J.m^{-2}$	2
Density of epoxy matrix	$Kg.m^{-3}$	1200
Elastic modulus of epoxy matrix	GPa	4.5
Tensile strength of epoxy matrix	MPa	130
Poisson's ratio of epoxy matrix	-	0.4
Fracture toughness of epoxy	$J.m^{-2}$	500

2.1.2 Experimental conditions and procedures

2.1.2.1 Workpiece material and properties

The workpiece material was CFRP composite with dimensions of 155 mm × 105 mm × 18 mm. The CFRP was composed of carbon fibers and epoxy resin matrix. The CFRP had 21 layers of fabric (42 layers of carbon fiber) which was plain woven fabric of carbon fibers with an orientation of 0/90 degrees. Thickness of the carbon fiber yarn in the woven fabric was 0.2 mm with a width of 2.5 mm. Properties of the CFRP are shown in Table 2.1.

2.1.2.2 Experimental set-up and conditions

The experiments were conducted on a rotary ultrasonic machine (Series 10, Sonic-Mill, Albuquerque, NM, USA). The cutting tool was a core drill with metal-bonded diamond abrasives. Coolant was injected to the interface between the tool and the workpiece to keep them cool. Figure 2.1 shows a schematic diagram of experimental set-up. It consists of an ultrasonic spindle system, a data acquisition system, and a coolant system. The ultrasonic spindle, power supply, electric motor, and control panel comprise the ultrasonic spindle system. The power supply converts low

frequency (60 Hz) electrical supply into high frequency (20 kHz) AC output. This AC output is converted into mechanical vibrations by the piezoelectric transducer in the ultrasonic spindle. The coolant system provides coolant to the spindle and the interface of machining. The coolant system comprises of pump, coolant tank, pressure regulator, flow rate and pressure gauges, and valves.

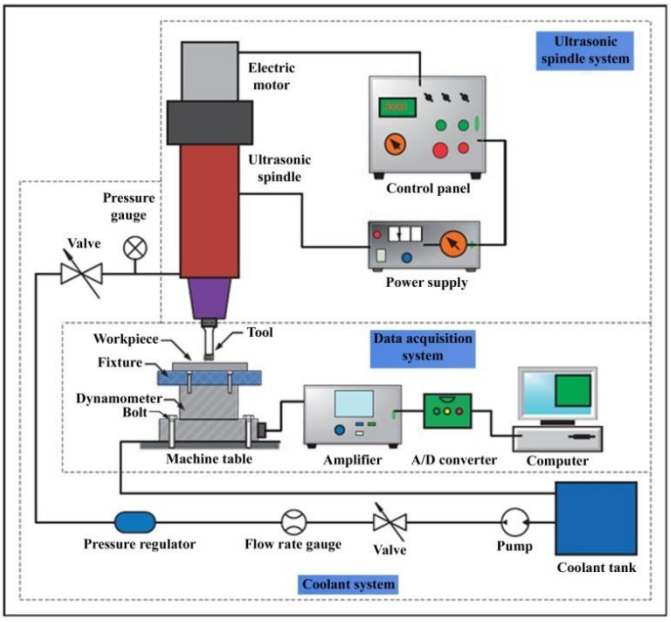

Figure 2.1 Experimental set-up

2.1.2.3 Design of experiments

A 23 (two-level three-factor) full factorial design was employed with 8 unique experimental conditions. Three input variables were studied.

• Ultrasonic power: percentage of power from ultrasonic power supply that controls ultrasonic vibration amplitude

• Tool rotation speed: rotational speed of the core drill

• Feedrate: feedrate of the core drill

Table 2.2 provides the low and high levels of the input variables.

Table 2.2 Low and high levels of input variables

Input variable	Unit	Low	High
Ultrasonic	%	20	60
Tool rotation	$rev.s^{-1}$	2000	4000
Feedrate	$mm.s^{-1}$	0.2	0.5

Two replicates were carried out for each combination of input variables, for a total number of 16 runs. Three output variables (cutting force, torque, and surface roughness) were studied.

Table 2.3 is the experimental matrix associated with each test.

Table 2.3 Experimental matrix

Test #	Test order		Ultrasonic power	Tool rotation speed	Feed rate
	Test1	Test2			
1	9	15	-	-	-
2	10	13	+	-	-
3	12	14	-	+	-
4	11	16	+	+	-
5	1	5	-	-	+
6	3	6	+	-	+
7	4	8	-	+	+
8	2	7	+	+	+

The important issue here was to maintain identical values for the low and high level of feedrate throughout the experimental runs. This was needed to restrict the randomization of the experimental runs. Split-plot design was used to obtain nested low level of feedrate and nested high level of feedrate. Minitab software (Version 14, Minitab Inc. State College, Pennsylvania, USA) was used to obtain non randomized feedrate as shown in Table 2.3.

2.1.2.4 Measurement procedure

A dynamometer (Kistler 9272, Kistler Instrument Corp, Switzerland) was used to measure torque and cutting force along the tool axis (feedrate direction). A workpiece was mounted on top

of the fixture located on top of the dynamometer. Bolts were used to attached the dynamometer to the machine, as shown in Figure 2.1.

Charge amplifier (Kistler 5010, Kistler Instrument Corp, Switzerland) was used to amplify the signal from the dynamometer and an analog to digital converter was used to convert that signal to a numerical signal.

LABVIEWTM (Version 5.1, National Instruments, Austin, TX. USA) was used to collect the cutting force and torque data.

Surface roughness of the machined holes was measured with a surface profilometer (Mitutoyo SJ-400, Mitutoyo Corporation, Kanagawa, Japan). Test range was set as 4 mm and the surface roughness in this study was characterized by average surface roughness, Ra. RUM is a core drilling process, since it produced a hole and a rod after each test. Surface roughness was measured on the cylindrical surface of the drilled hole. Surface roughness was measured at entrance and exit locations along the axial direction of the hole. Four measurements were taken at each quadrant, as shown in Figure 2.2. Eight Ra values were obtained for each test. Table 2.4 shows the average values of those eight measurements.

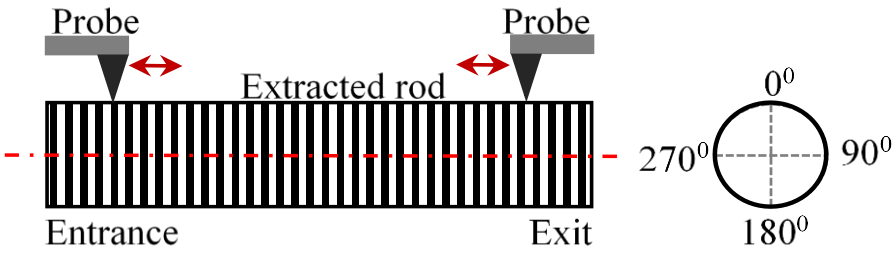

Figure 2.2 Measurement procedure of surface roughness

2.1.3 Experimental results

Cutting force and torque are the most important output variables in rotary ultrasonic machining of CFRP. Surface roughness which assures the quality of a surface of a drilled hole and

torque, tool wear, all delamination in RUM of CFRP and cutting temperature are related to cutting force [22,23]. Therefore, in this study output variables studied are cutting force, torque and surface roughness.

Figure 2.3 and Figure 2.4 show a typical curve of measured cutting force and torque versus time respectively. The maximum cutting force and the maximum torque were used to represent the cutting force and torque. Table 2.4 presents the experimental results.

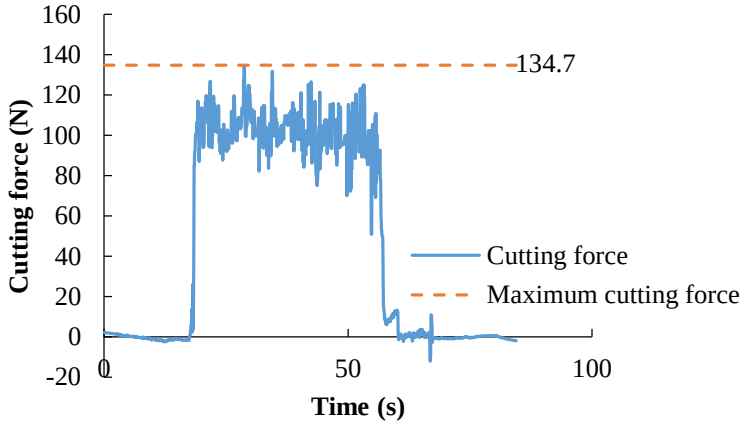

Figure 2.3 Variation of cutting force with time

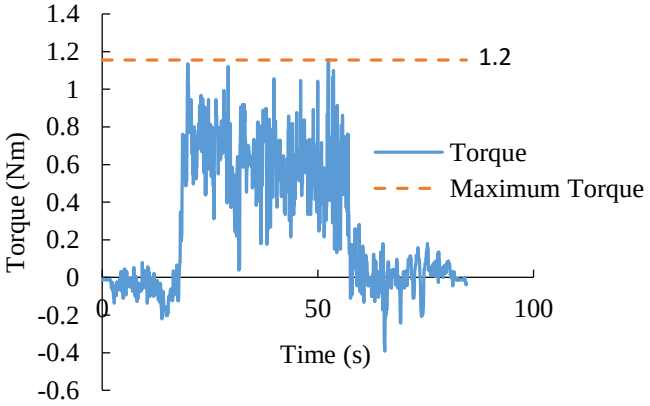

Figure 2.4 Variation of torque with time

Minitab software (Version 14, Minitab Inc. State College, Pennsylvania, USA) was used to analyze data using ANOVA (analysis of variance) to identify significant effects at the significance level of $\alpha = 0.05$. P-values for each interaction effects are reported in Table 2.5.

Table 2.4 Experimental results

Run Order	Cutting Force (N)	Torque (Nm)	Surface roughness (μm)
1	134.7	1.16	2.15
2	112.9	1.17	2.16
3	124.7	1.67	2.14
4	108.9	0.95	1.80
5	135.5	1.27	1.85
6	172.2	3.14	1.89
7	132.2	1.13	2.09
8	140.4	0.85	1.61
9	97.5	1.00	2.23
10	187.8	1.70	1.96
11	113.8	1.57	2.18
12	128.6	1.47	2.42
13	148.6	1.38	2.03
14	107.0	1.19	2.92
15	107.1	2.18	2.26
16	85.1	0.84	2.44

2.1.3.1 Main effects

Main effects of ultrasonic power, tool rotation speed, and feedrate on cutting force, torque, and surface roughness were considered.

Table 2.5 P-values of effects

Effect	Output variable	Input variable	P-value
Main effect	Cutting force	Feedrate	0.44
		Tool rotation speed	0.09
		Ultrasonic power	0.29
	Torque	Feedrate	0.99
		Tool rotation speed	0.06
		Ultrasonic power	0.29
	Surface roughness	Feedrate	0.02
		Tool rotation speed	0.38
		Ultrasonic power	0.77
Two-factor interaction	Cutting force	Tool rotation speed, feedrate	0.33
		Ultrasonic power, feedrate	0.55
		Ultrasonic power, tool rotation speed	0.03
	Torque	Tool rotation speed, feedrate	0.25
		Ultrasonic power, feedrate	0.40
		Ultrasonic power, tool rotation speed	0.13
	Surface roughness	Tool rotation speed, feedrate	0.02
		Ultrasonic power, feedrate	0.02
		Ultrasonic power, tool rotation speed	0.80
Three-factor interaction	Cutting force	Tool rotation speed, feedrate, ultrasonic power	0.10
	Torque	Tool rotation speed, feedrate, ultrasonic power	0.28
	Surface roughness	Tool rotation speed, feedrate, ultrasonic power	0.02

2.1.3.1.1 Main effects on cutting force

Figure 2.5 shows main effects on cutting force of three process variables: ultrasonic power, tool rotation speed, and feedrate. Cutting force increased with the increase of ultrasonic power and feedrate. With the increase of tool rotation speed, cutting force decreased.

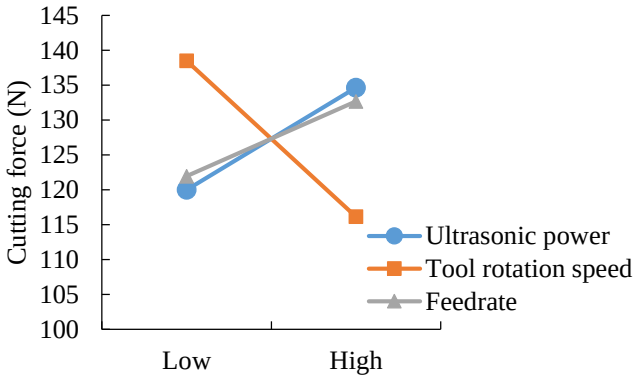

Figure 2.5 Main effects on cutting force

2.1.3.1.2 Main effects on torque

Figure 2.6 shows main effects of ultrasonic power, speed of tool rotation and feedrate on torque. Similar to cutting force, torque increased with increased ultrasonic power and feedrate, but torque decreased with increased tool rotation speed.

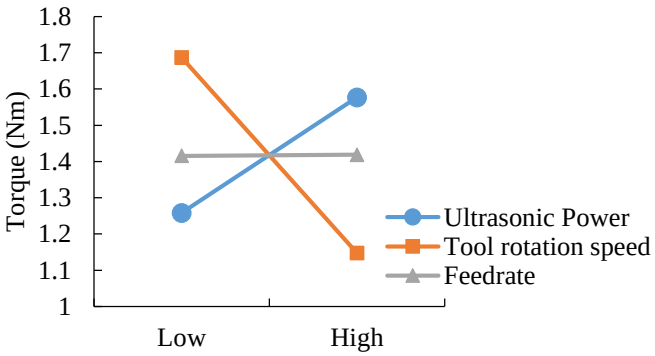

Figure 2.6 Main effects on torque

2.1.3.1.3 Main effects on surface roughness

Figure 2.7 shows main effects of ultrasonic power, tool rotation speed, and feedrate on surface roughness. As shown in Figure 2.7, surface roughness decreased with increased ultrasonic power and feedrate. Feedrate had the most significant effect on surface roughness, with P-value of 0.019. Effects of tool rotation speed (P-value = 0.38) and ultrasonic power (P-value = 0.77) on surface roughness are not significant at the significant level of $\alpha = 0.05$.

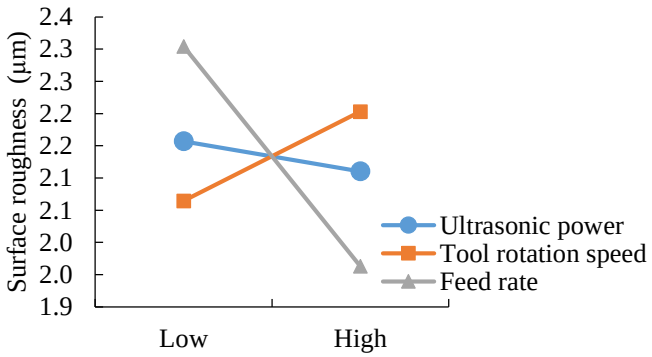

Figure 2.7 Main effects on surface roughness

2.1.3.2 Two-factor interactions

Two-factor interactions were obtained for cutting force, torque and surface roughness.

2.1.3.2.1 Two-factor interactions on cutting force

Three two-factor interactions on cutting force are shown in Figure 2.8. Interaction effect between ultrasonic power and tool rotation speed on cutting force is significant with P-value of 0.03. Interaction effects of tool rotation speed and feedrate (P-value = 0.34), and ultrasonic power and feedrate (P-value = 0.55) on cutting force are not significant at the significance level of $\alpha = 0.05$.

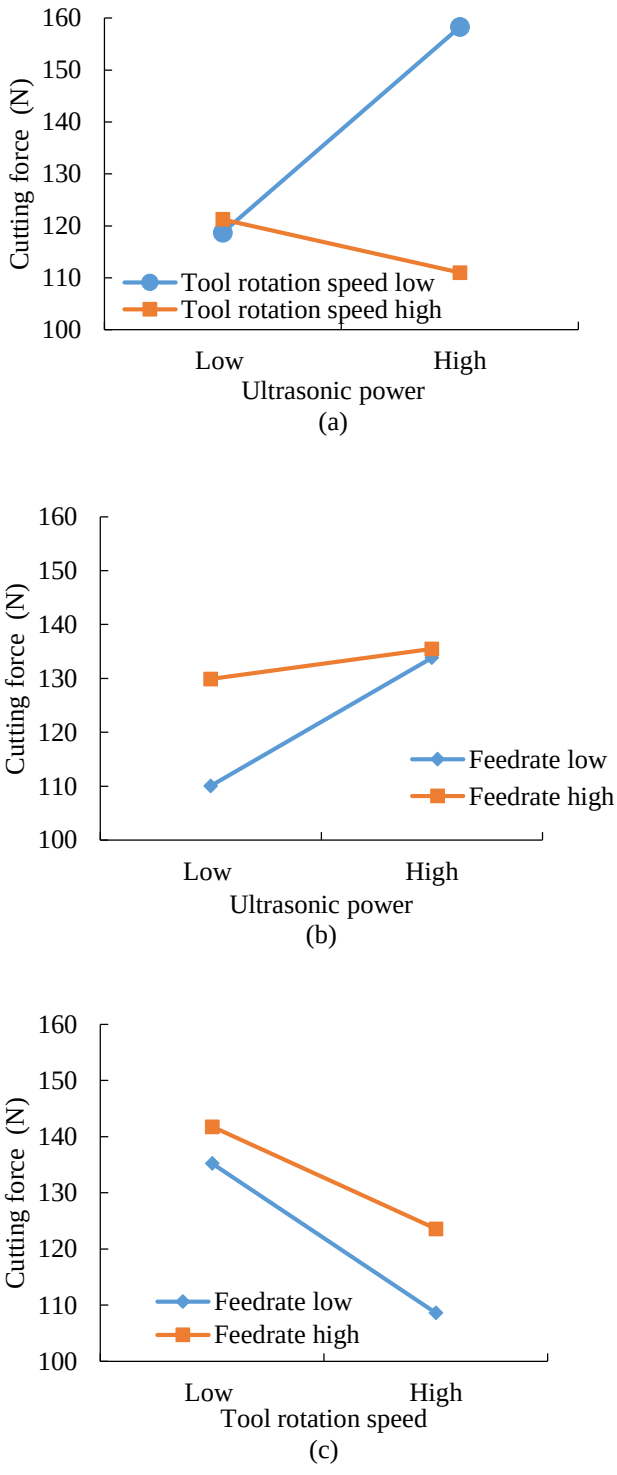

Figure 2.8 Two-factor interactions on cutting force

2.1.3.2.2 Two-factor interactions on torque

Three two-factor interactions on torque are shown in Figure 2.9. Interaction effects of tool rotation speed and feedrate (P-value = 0.25), ultrasonic power and feedrate (P-value = 0.4), and ultrasonic power and tool rotation speed (P-value = 0.13) on torque are not significant at the significance level of $\alpha = 0.05$.

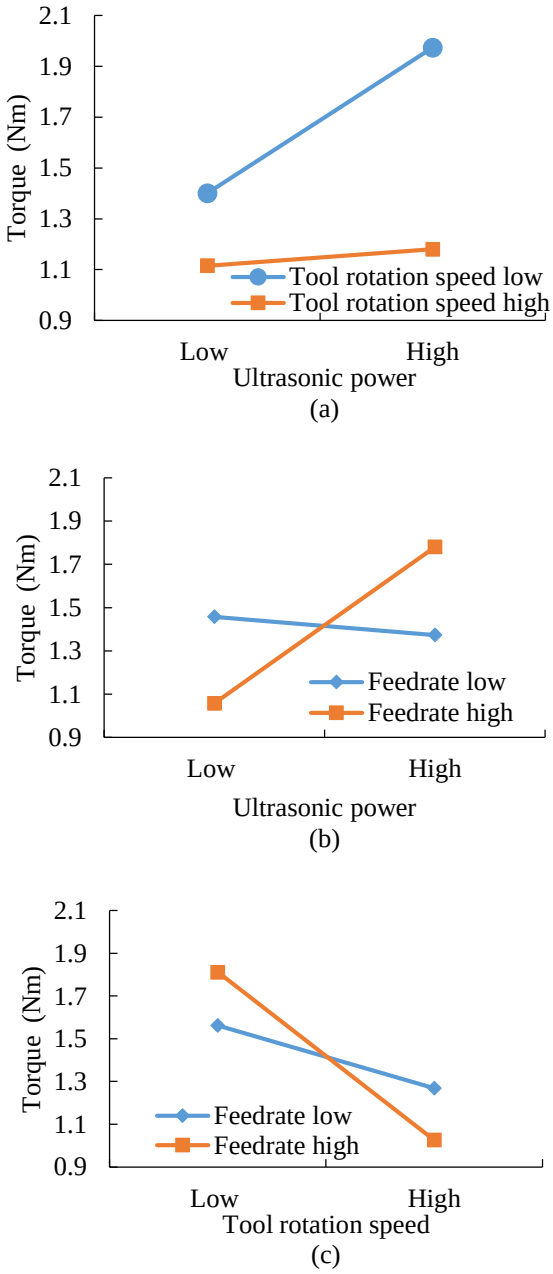

Figure 2.9 Two-factor interactions on torque

2.1.3.2.3 Two-factor interactions on surface roughness

Three two-factor interactions on surface roughness are shown in Figure 2.10. Interaction effects between tool rotation speed and feedrate, and ultrasonic power and tool rotation speed on surface roughness are significant with P-value of 0.02. Interaction effect of ultrasonic power and tool rotation speed on cutting force (P-value = 0.03) is significant at the significance level of $\alpha = 0.05$.

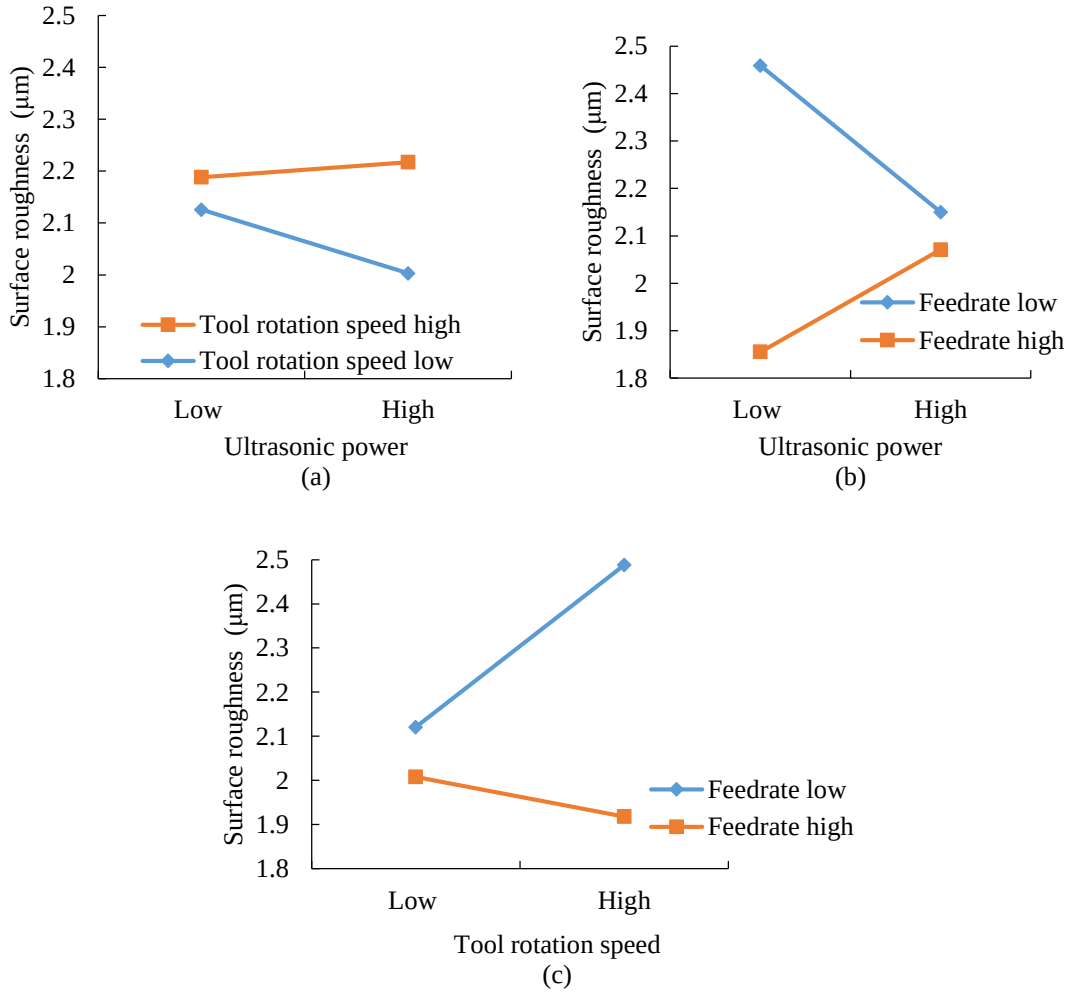

Figure 2.10 Two-factor interactions on surface roughness

2.1.3.3 Three-factor interactions

Three-factor interactions were obtained for cutting force, torque and surface roughness.

2.1.3.3.1 Three-factor interactions on cutting force

The three-factor interaction effect of ultrasonic power, tool rotation speed and feedrate on cutting force, as shown in Figure 2.11, is not significant (P-value = 0.10).

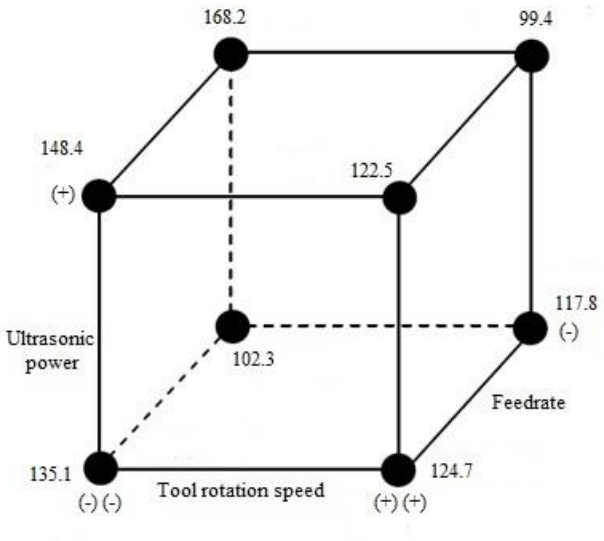

Figure 2.11 Three-factor interactions on cutting force

2.1.3.3.2 Three-factor interactions on torque

The three-factor interaction effect of ultrasonic power, tool rotation speed, and feedrate on torque, as shown in Figure 2.12, is not significant (P-value = 0.28).

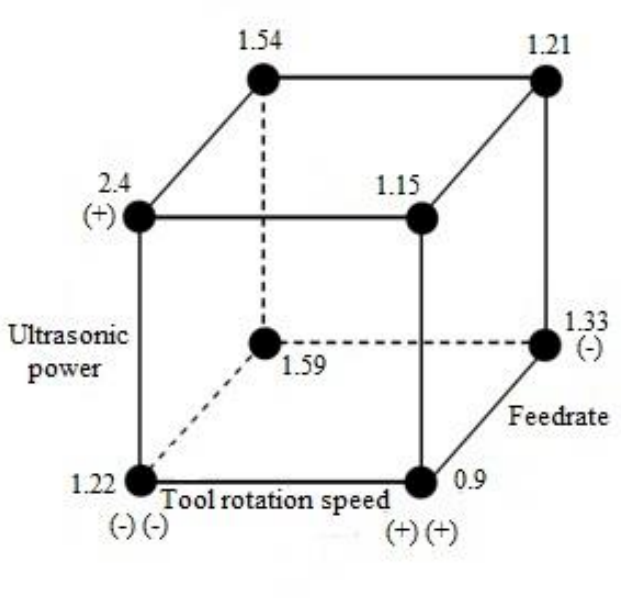

Figure 2.12 Three-factor interactions on torque

2.1.3.3.3 Three-factor interactions on surface roughness

The three-factor interaction effect of ultrasonic power, tool rotation speed, and feedrate on surface roughness, as shown in Figure 2.13, is significant (P-value = 0.02).

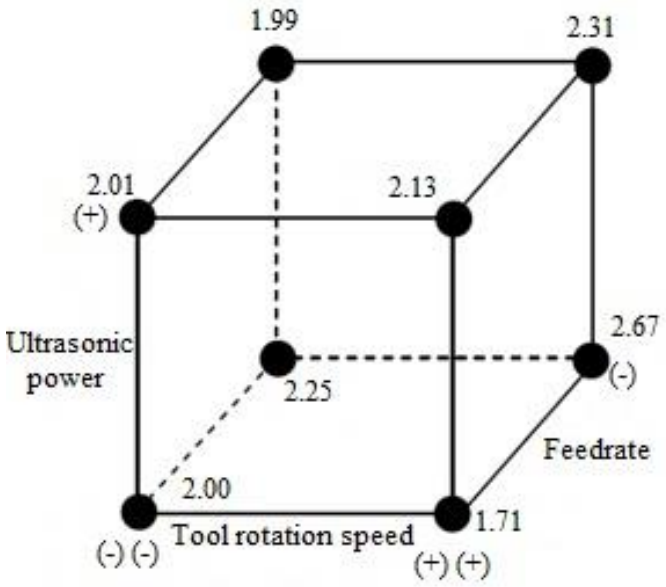

Figure 2.13 Three-factor interactions on surface roughness

2.1.4 Conclusions

The following conclusions are drawn from the study of two-level three-factor full factorial design of input variables of ultrasonic power, tool rotation speed, and feedrate to the outputs of cutting force, torque, and surface roughness.

1. Surface roughness has significant effects in rotary ultrasonic machining of CFRP within the variable settings tested in this paper on feedrate, two-factor interactions of tool rotation speed and feedrate, and ultrasonic power and feedrate and three-factor interactions of tool rotation speed, feedrate, and ultrasonic power. It presents surface roughness decreases with increased feedrate.

2. Two-factor interaction on cutting force of the input variables (ultrasonic power and tool rotation speed) is significant. It presents cutting force increases with ultrasonic power and decreases with tool rotation speed.

2.2 Effects of process parameters on delamination of drilling of CFRP

Paper title:

Rotary ultrasonic machining of CFRP: effects of process parameters on delamination

Published in:

Proceedings of the ASME 2016 International Manufacturing Science & Engineering Conference (MSEC-2016), June 27-July 1, 2016, Blacksburg, Virginia, USA

Authors' names:

Fernando, P., Pei, Z.J., Zhang, M., Song, X.

Authors' affiliations:

Department of Industrial and Manufacturing Systems Engineering, Kansas State University, Manhattan, KS 66506, USA

2.2.1 Introduction

Drilling is a primary machining process while drilling composites is a peculiar process due to its properties and difficulty of producing quality holes [25]. Twist drilling and similar traditional methods are widely used in machining of composites which is challenging, due to their non-homogeneity and anisotropic properties [24, 30, 32, 34, 37-39]. Faster and quality fabricating and machining methods are needed with the increased usage of composites, to provide manufacturer and consumer satisfied products [24, 25, 27-30, 33]. Generally, CFRP can be machined efficiently by laser and waterjet cutting technologies even though they are associated with various forms of defects [41]. Common defect of laser cutting is occurrence of heat-affected zones [41, 42]. Water jet cutting encountered with many defects such as abrasive penetration, fiber pull-out and delamination [41, 43]. Several researchers have studied general aspects of machining of composites. More studies can be found in drilling of composites recently, as it encountered problems for drill bits and its material, specially wear of traditional drill bits [24-28, 30, 31, 33, 36-39].

Another major problem associated with drilling of composites is delamination [25, 27,-30, 32, 34, 36, 39]. Delamination is known as failures occur in laminates of composites [25, 28]. There are two types of common delamination; push-out delamination and peel-off (peel-up) delamination [25]. Push out delamination occurs at exit surface due to thrust force of drill bit and peel-off delamination can be occurred at both exit and entry surfaces, depending on the geometry of drill bit [25]. If delamination took place when drilling which is the final machining process for most of production lines, a whole part can be rejected due to poor quality of a hole [39]. This is a huge loss in both economical vise and material vise. This encourages researchers to gain delamination free techniques for composite drilling. This study, for the first time, investigates the effects of process

parameters on the delamination of CFRP processed by rotary ultrasonic machining. These process parameters are variable feed rate, variable spindle speed and the use of backing plate.

2.2.2 Experimental conditions and procedures

2.2.2.1 Workpiece material and properties

The workpiece material was a CFRP composite with dimensions of 155 mm × 105 mm × 18 mm. The CFRP was composed of carbon fibers and epoxy resin matrix. The CFRP had 21 layers of fabric (42 layers of carbon fiber) which was plain woven fabric of carbon fibers with an orientation of 0/90 degrees. Thickness of the carbon fiber yarn in the woven fabric was 0.2 mm with a width of 2.5 mm. Properties of CFRP are shown in Table 2.1. An aluminum plate with the dimensions of 155 mm × 105 mm × 3 mm was used as a backing plate (Figure 2.14) which was placed under CFRP workpiece with no bonding.

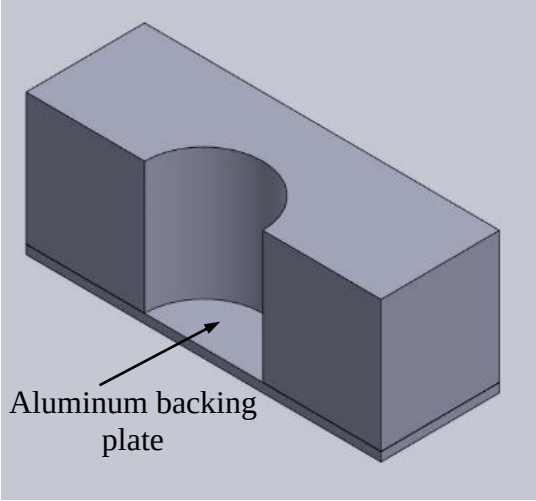

Figure 2.14 Use of backing plate

2.2.2.2 Experimental set-up and conditions

The experiments were conducted on a rotary ultrasonic machine (Series 10, Sonic-Mill, Albuquerque, NM, USA). The tool was a core drill with metal-bonded diamond abrasives. Coolant

was injected to the interface between the tool and the workpiece to keep them cool. Figure 2.1 is a schematic diagram of the experimental set-up. It consists of an ultrasonic spindle system, a data acquisition system, and a coolant system. The ultrasonic spindle, power supply, electric motor, and control panel comprise the ultrasonic spindle system. The power supply converts low frequency (60 Hz) electrical supply into high frequency (20 kHz) AC output. This AC output is converted into mechanical vibrations by the piezoelectric transducer in the ultrasonic spindle. The coolant system provides coolant to the spindle and the interface of machining. The coolant system comprises of pump, coolant tank, pressure regulator, flow rate and pressure gauges, and valves.

2.2.2.3 Design of experiments

The design shown in the Table 2.6 was used to conduct the experiment. Ultrasonic power (percentage of ultrasonic power that controls ultrasonic vibration amplitude) which was fixed at 30% (150 W), spindle speed and feedrate were three process variables. Two types of federate and spindle speed were used. Fixed feedrate and spindle speed were used under "normal" condition which the entire hole was drilled using a feedrate of 0.2 mms-1 and spindle speed of 3000 rpm. In variable feedrate, feedrate was changed from 0.2 mms-1 to 0.1 mms-1 after 65 seconds of drilling time of a particular hole. Same procedure was used for the variable spindle speed which changed spindle speed from 3000 rpm to 1000 rpm.

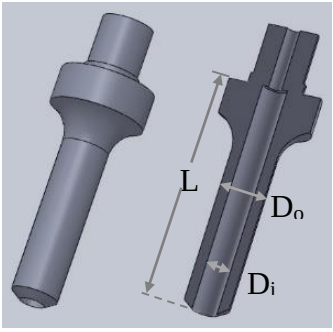

Figure 2.15 Outer core tool

Metal-bonded diamond abrasive outer core drill (Figure 2.15) was used to perform the experiment. The outer and inner diameters (Do, Di) of the tool were 9.48 mm and 5.02 mm respectively and tuning length was 44.5 mm. After preliminary studies, three replicates were conducted for each experimental condition. Three output variables (cutting force, torque, and delamination) were studied.

Table 2.6 Experimental matrix

Condition	Spindle speed (rpm)	Feed rate (mms^{-1})
Normal	3000	0.2
Variable feed rate	3000	0.2/0.1
Variable spindle speed	3000/1000	0.2
Use of backing plate	3000	0.2

2.2.2.4 Measurement Procedure

A dynamometer (Kistler 9272, Kistler Instrument Corp, Switzerland) was used to measure torque and cutting force along the tool axis (feed rate direction). A work piece was mounted on top of the fixture located on top of the dynamometer. Bolts were used to attach the dynamometer to the machine, as shown in Figure 2.1.

A charge amplifier (Kistler 5010, Kistler Instrument Corp, Switzerland) was used to amplify the dynamometer signal, and an Analog to Digital converter was used to convert that electrical signal to a numerical signal.

LABVIEWTM (Version 5.1, National Instruments, Austin, TX. USA) was used to collect the cutting force and torque data.

A microscope (Olympus BX51, Olympus Corporation, Tokyo, Japan) was used to measure delamination of machined holes.

Microscopes show high resolving power referred as depth of focus (DOF) along its longitudinal axis. Based on DOF with the assistant of fine-adjustment delamination thickness was measured. The CFRP workpiece was placed flat on the adjustable table of the microscope with illumination of florescent lamp. Then the coarse adjustment was gradually turned until exit surface of the CFRP workpiece comes in to screen. Fine adjustment was used to focus exit surface correctly and note down the corresponding reading of the fine adjustment. Same procedure was repeated to focus on deepest layer of the delamination and record the new reading of the fine adjustment. Difference of the two readings gives delamination thickness with one-micron resolution (Figure 2.16).

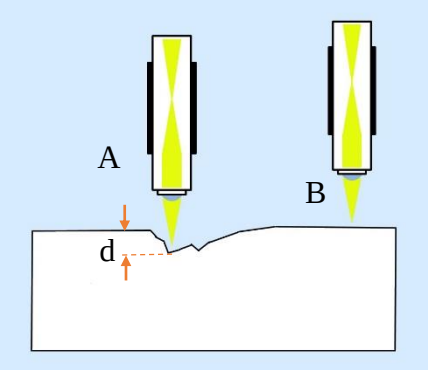

Figure 2.16 Measurement of delamination (thickness)

(A) Focus on the deepest layer of the delamination (B) Focus on the exit surface of the CFRP workpiece, two arrows show the difference of the two readings corresponded to the delamination thickness (d)

2.2.3 Experimental results and discussion

Cutting force and torque are the most important output variables in rotary ultrasonic machining of CFRP. The maximum cutting force and maximum torque represented the cutting force and torque. Table 2.7 presents experimental results.

Figures 2.17, 2.18, and 2.19 show cutting force, torque, and delamination vs experimental condition, respectively. As shown in Figure 2.17, the lowest cutting force was resulted from variable feed rate while the highest cutting force was resulted from variable spindle speed. This outcome of variable feedrate is consistent with the reported work by Cong et al. (2014) for RUM of CFRP/Ti stacks using variable feedrate. Cutting force for both normal and use of backing plate experiment conditions was approximately 250 N, as identical values were used for input variables in both conditions. Experimental conditions: Normal, Variable feed rate and use of backing plate reported a torque (Figure 2.18) in between 2 Nm and 3 Nm. The cutting force, torque, and delamination show similar trend for the experimental conditions: normal, variable feedrate, and variable spindle speed as shown from Figures 2.17 - 2.19. Zero delamination was observed in experimental condition of use of backing plate as shown in Figure 2.19. A hole in the fixture which was designed to prevent tool hitting, could lead push out of bottom layer of CFRP due to thrust force while drilling. Therefore, backing plate was used as a support for the bottom layer of CFRP. Figure 2.20 shows the occurrence of delamination in the absence of baking plate. But some edge damages were shown in the exit surface by removed metal parts of backing plate. Next lowest delamination was reported in experimental condition of variable feed rate. Except use of baking plate, all other experimental conditions have shown high uncertainty on delamination.

Table 2.7 Experimental results

Condition	Run Order	Cutting Force (N)	Torque (Nm)	Delamination (μm)
Normal	1	258.2	2.7	72
Normal	2	240.8	3.2	150
Normal	3	265.9	2.5	45
Variable feedrate	4	220.9	2.5	32
Variable feedrate	5	205.5	3.3	40
Variable feedrate	6	209.8	2.0	110
Variable spindle speed	7	303.7	4.7	87
Variable spindle speed	8	314.2	4.5	48
Variable spindle speed	9	331.7	5.7	168
Use of backing plate	10	247.1	3.8	0
Use of backing plate	11	225.9	2.2	0
Use of backing plate	12	247.5	1.9	0

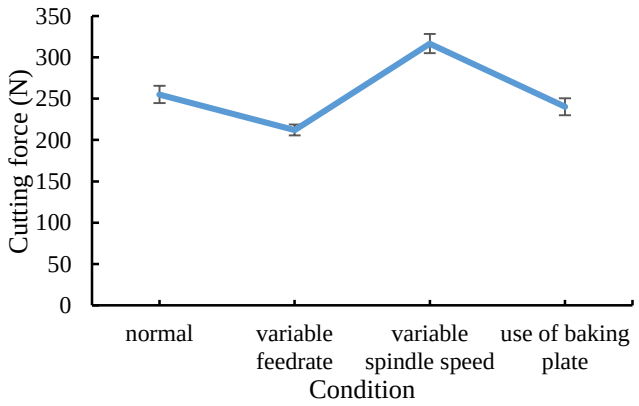

Figure 2.17 Cutting force vs. experimental condition

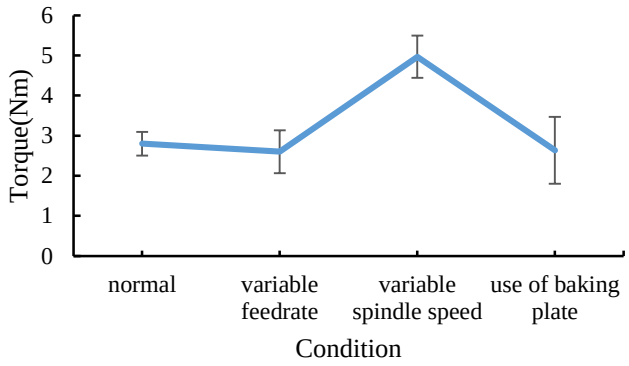

Figure 2.18 Torque vs. experimental condition

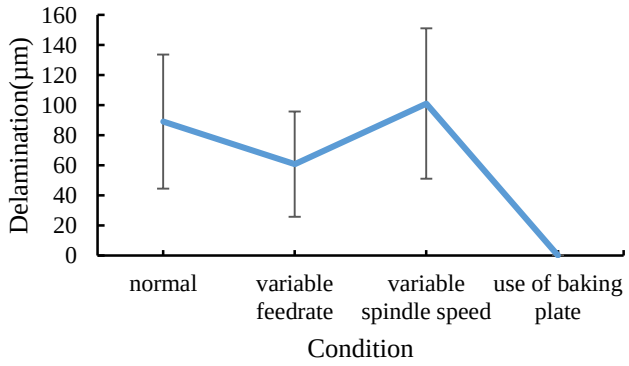

Figure 2.19 Delamination vs. experimental condition

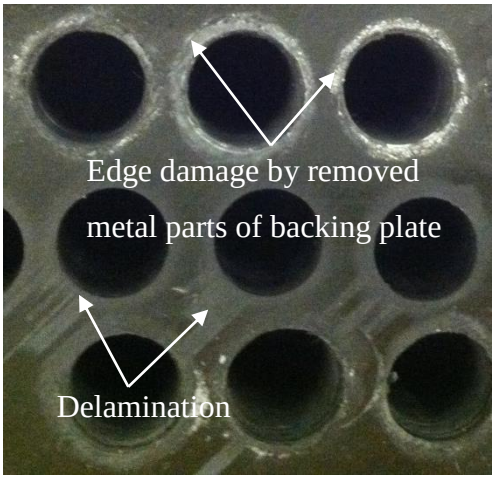

Figure 2.20 Edge damage by removed metal parts of backing plate

2.2.4 Conclusions

This paper mainly studies the delamination in rotary ultrasonic drilling of CFRP. This study has been developed to obtain delamination free drilling techniques for rotary ultrasonic drilling of CFRP. Following are the main conclusions obtained.

1. Backing plate under the exit surface prevents delamination completely. But it shows some edge damage in the exit surface by the removed metal parts of the backing plate. Further studies need to be performed to select the most suitable material for the backing plate.
2. Use of variable spindle speed (low spindle speed at the exit surface) has no any assistance in preventing delamination.
3. Variable federate (reduced feedrate at the exit surface) helps to decrease delamination.
4. Delamination is associated with high variance; therefore, it shows high unpredictability.
5. Certain correlations could be existing between the cutting force, torque, and the delamination. Further studies need to be performed to prove it.

2.3 Effect of tool end angle on delamination of drilling of CFRP

Paper title:

Rotary ultrasonic machining: effects of tool end angle on delamination of CFRP drilling

Published in:

Proceedings of the ASME 2017 International Manufacturing Science & Engineering Conference (MSEC-2017), June 4-8, 2017, Los Angeles, California, USA

Authors' names:

Fernando, P.[1], Pei, Z.J.[2], Zhang, M.[1], Cong, W.[3]

Authors' affiliations:

1. Department of Industrial and Manufacturing Systems Engineering, Kansas State University, Manhattan, KS 66506, USA
2. Department of Industrial and Systems Engineering, Texas A & M University, College Station, TX 77843 USA
3. Department of Industrial Engineering, Texas Tech University, Lubbock, TX 79409, USA

2.3.1 Introduction

Delamination is a major problem when drilling CFRP, the separation of layers which makes damage to the surface of the material or the component [22, 29, 54]. Two common delamination types are: peel-up/off delamination as shown in Figure 2.21 and push-down delamination [52]. In the aerospace industry, rejections caused by delamination accounted for 60% of all rejections in the final assembly [48, 55]. The CFRP drilling process, which occurs close to the end of the manufacturing process, causes a comparatively huge loss to entrepreneurs due to component rejection caused by delamination [56]. This challenge motivates researchers to identify delamination-free techniques to drill CFRP. Several investigators have cited thrust force as a major cause for delamination [55, 57]. Similarly, it can be seen in the literature, several reported studies also identified that cutting force (thrust force) as a major concern on edge chipping [30, 58]. Even though, Qin et al. found that, tool end angle has an influence on edge chipping thickness of rotary ultrasonic machining (RUM) of ceramic [30]. Edge chipping in drilling on brittle materials can be relate to delamination in composite drilling. Therefore, this study, for the first time, investigate on effects of tool end angel on delamination in RUM of CFRP.

2.3.2 Experimental conditions and procedures

2.3.2.1 Workpiece material and properties

The workpiece material was CFRP with dimensions of 155 mm × 105 mm × 18 mm. The CFRP was composed of carbon fibers and epoxy resin matrix with 21 layers of plain woven fabric of carbon fibers with an orientation of 0/90 degrees (42 layers of carbon fiber). Carbon fiber yarn thickness in the woven fabric was 0.2 mm with a width of 2.5 mm. CFRP properties are shown in Table 2.1.

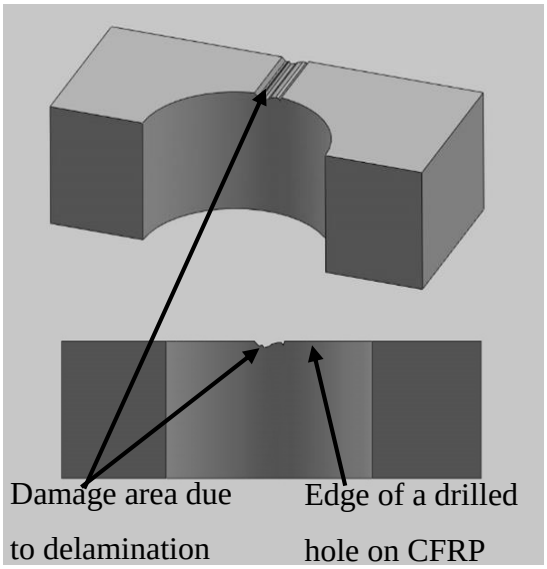

Figure 2.21 Delamination at exit surface of CFRP

2.3.2.2 Experimental set-up and conditions

Experiments were conducted on a rotary ultrasonic machine (Series 10, Sonic-Mill, Albuquerque, NM, USA). The cutting tools were core drills with metal-bonded diamond abrasives with different tool end angels as illustrated in Figure 2.22.

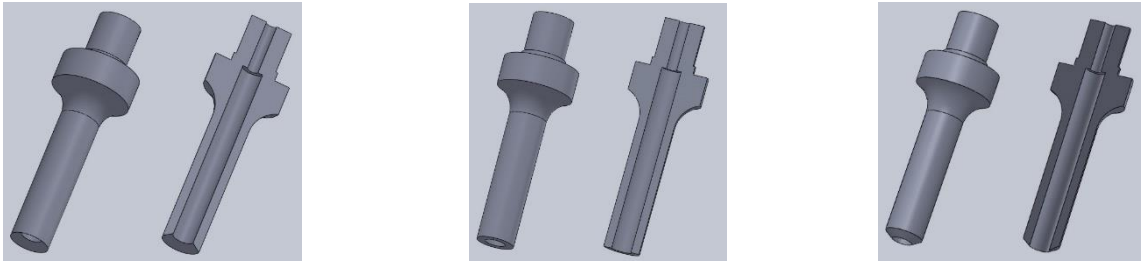

(a) Negative tool end angle (b) Zero tool end angle (c) Positive tool end angle

Figure 2.22 Tool end angels

Schematic diagram of the experimental set-up is shown in Figure 2.1. It consists of an ultrasonic spindle system, a data acquisition system, and a coolant system. The ultrasonic spindle system is comprised of an ultrasonic spindle, a power supply, an electric motor, and a control

panel. The power supply converts a low frequency (60 Hz) electrical supply (110v) into a high frequency (20,000 Hz) electrical signal. The piezoelectric transducer in the ultrasonic spindle converted that electrical signal into high frequency (20,000 Hz) mechanical vibrations. The coolant system consists of a pump, a coolant tank, a pressure regulator, flow rate and pressure gauges, and valves.

2.3.2.3 Design of experiments

The experiments were conducted according to the design shown in Table 2.8. Three process variables: ultrasonic power (the percentage of ultrasonic power which controls ultrasonic vibration amplitude), tool rotation speed and feedrate were kept constant throughout the experiments. Ultrasonic power of 30% is corresponded with power output of 150W.

Three replicates were carried out for each tool end angle. Three output variables (cutting force, torque and delamination) were studied.

Table 2.8 Experimental matrix

Condition	Tool end angel	Ultrasonic power %	Tool rotation speed rpm	Feed rate mm/s
1	Negative	30	3000	0.2
2	Zero	30	3000	0.2
3	Positive	30	3000	0.2

2.3.2.3 Measurement Procedure

A dynamometer (Kistler 9272, Kistler Instrument Corp, Switzerland) was used to measure torque and cutting force. A charge amplifier (Kistler 5010, Kistler Instrument Corp, Switzerland) was used to amplify the signal from dynamometer, and an analog to digital converter was used to convert that electrical signal in to a numerical signal.

LABVIEWTM (Version 5.1, National Instruments, Austin, TX. USA) was used to collect the cutting force and torque data.

A microscope (Olympus BX51, Olympus Corporation, Tokyo, Japan) was used to measure delamination of the machined holes. Microscopes show high resolving power referred as depth of focus (DOF) along its longitudinal axis. Based on DOF with the assistant of fine-adjustment, delamination thickness was measured. The CFRP workpiece was placed flat on the adjustable table of the microscope with illumination of florescent lamp. Then the coarse adjustment was gradually turned until exit surface of the CFRP workpiece comes in to screen. Fine adjustment was used to focus exit surface precisely and note down the corresponding reading of the fine adjustment. Same procedure was repeated to focus on deepest layer of the delamination and record the new reading of the fine adjustment. Difference of the two readings gives delamination thickness with one micro-meter resolution (Figure 2.16).

2.3.3 Experimental results and discussion

Table 2.9 presents experimental results. The reported maximum cutting force and maximum torque were used in this study. A comparison of cutting force, torque, and delamination between three tool end angels under the same ultrasonic power, tool rotation speed, and feedrate were shown in Figures 2.23, 2.24, and 2.25 respectively. The lowest cutting force was obtained from zero tool end angle, followed by positive and negative tool end angles. Effect of tool end angle on torque also showed similar trend as in cutting force. The highest torque was obtained by negative tool end angle and it is much higher than that obtained from zero and positive tool end angles. The lowest delamination was obtained from positive tool end angle, followed by negative

tool end angle and zero tool end angle. Figure 2.26 shows the occurrence of delamination at the exit surface of CFRP workpiece.

Table 2.9 Experimental results

Run order	Cutting force (N)	Torque (Nm)	Delamination (μm)
1	224.86	4.63	48
2	218.84	2.53	48
3	228.29	1.61	42
4	191.22	2.22	142
5	198.88	2.12	67
6	155.19	1.32	109
7	268.75	7.78	37
8	310.05	8.41	80
9	271.10	8.55	44

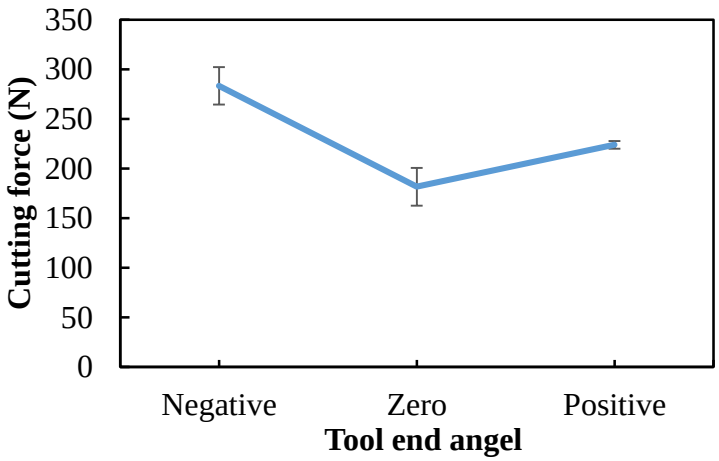

Figure 2.23 Effect of tool end angel on cutting force

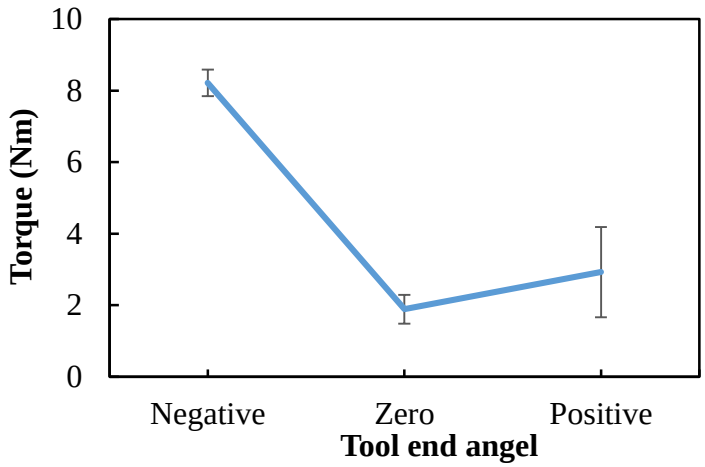

Figure 2.24 Effect of tool end angel on torque

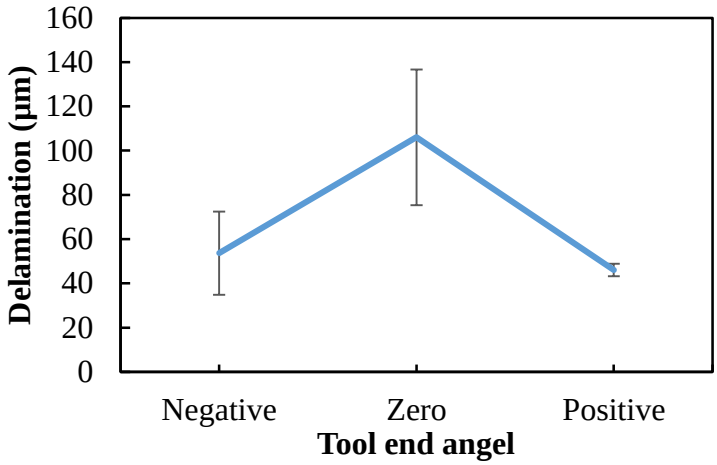

Figure 2.25 Effect of tool end angel on delamination

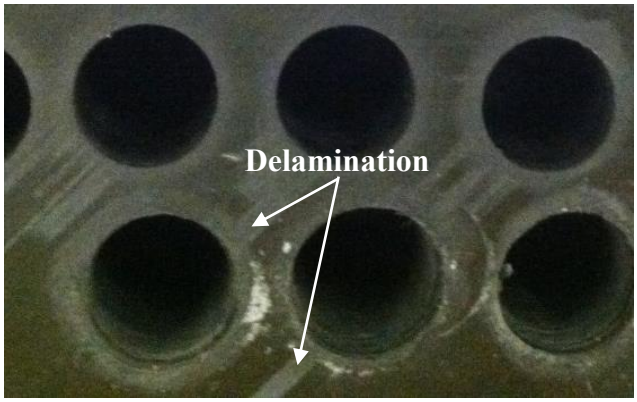

Figure 2.26 Delamination in exit surface of CFRP

As shown in Figures 2.23, 2.24 and 2.25, the zero tool end angle has obtained the lowest cutting force and the lowest torque but its delamination was the highest. This is not consistent with the reported studies in the literature, which are stated that thrust force is the major factor for the delamination of drilling of composites [55, 57]. The lowest delamination was obtained by positive tool end angle, which had higher cutting force and torque compared to the zero tool end angle. The highest cutting force and torque were reported by negative tool end angle, but its delamination was close to the delamination obtained by positive tool end angle. Positive and negative tool end angles show significant effect on delamination. Qin et al. reported that negative tool end angle obtained the lowest edge-chipping thickness and size, followed by positive tool end angle and zero tool end angle of drilling ceramic by using RUM, which is consistent with the outcome of this study [30].

2.3.4 Conclusions

This paper, for the first time investigated on effect of tool end angle on delamination in RUM of CFRP. Three tool end angles were tested under same input condition to find best tool end angle, which can reduce delamination in RUM of CFRP. The following are the conclusions obtained from this study:

1. Tool end angle has considerable influence on delamination in RUM of CFRP compared to cutting force and torque.
2. Positive and negative tool end angles show significant effect on delamination.
3. Since positive tool end angle show less variance on cutting force and delamination and also 26% lower cutting force compared to the negative tool end angle, positive tool end angle is the best tool end angle to reduce delamination with respect to zero and negative tool end angles.

2.4 Effects of abrasive properties on drilling of CFRP

Paper title:

Rotary ultrasonic machining of CFRP: effects of abrasive properties

Published in:

Proceedings of the ASME 2018 International Manufacturing Science & Engineering Conference (MSEC-2018), June 18-22, 2018, College Station, Texas, USA

Authors' names:

Fernando, P.[1], Pei, Z.J.[2], Zhang, M.[1]

Authors' affiliations:

1. Department of Industrial and Manufacturing Systems Engineering, Kansas State University, Manhattan, KS 66506, USA
2. Department of Industrial and Systems Engineering, Texas A & M University, College Station, TX 77843 USA

2.4.1 Introduction

In manufacturing, drilling is a primary and essential machining process. It accounts for more than 25% from all machining processes [61]. Drilling is probably the most common machining practice conducted on CFRP, which is challenging to conventional machining processes, such as twist drilling, to produce quality holes because of severe tool wear and complications associated with drill bits [24-29, 31, 32, 35-37, 39, 41]. Comparatively, researchers have shown that rotary ultrasonic machining (RUM) has the capability to machine CFRP successfully [9, 11, 13-16, 22, 62].

The reported studies on RUM of CFRP are mainly focused on effects of machining variables (feedrate, tool rotation speed, and ultrasonic power) on output variables such as cutting force, torque and surface roughness, comparisons of twist drilling and RUM, and comparisons of different cooling systems [11, 22, 23, 62]. In RUM, material removal mechanism is predominately based on the indentation of abrasive particles. Therefore, it is important to have a study on effects of abrasive properties on output variables. This paper, for the first time, investigates the effects of abrasive properties on RUM of CFRP. In this study, effects of abrasive properties: abrasive particle size and their concentration on output variables: cutting force, torque, and surface roughness were studied. Cutting force is the primary output variable in RUM since it has effects on all the other output variables, such as surface roughness of the drilled hole, torque, tool wear, delamination in CFRP, and cutting temperature [22, 23]. When tool rotation speed is fixed, torque reflects the variation of power requirement. Surface roughness of a drilled hole determines how it interacts with a component to be assembled. Surface roughness is crucial to interactions between surfaces because surface roughness affects the real area of contact, wear rate, coefficient of friction, lubrication, and adhesive force [63].

2.4.2 Experimental conditions and procedures

2.4.2.1 Workpiece material and properties

The workpiece used in this study was CFRP composite with the dimensions of 155 mm × 380 mm × 22 mm. The compositions of the CFRP were epoxy resin matrix and carbon fiber reinforcements. The CFRP had 29 uni-directional continuous layers (Figure 2.27) of carbon fibers with an orientation of 45 degrees. Table 2.1 shows the properties of CFRP.

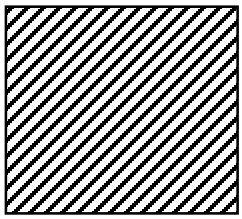

Figure 2.27 Uni-directional continuous fiber structure of CFRP

2.4.2.2 Experimental set-up and conditions

The experiments were conducted on a rotary ultrasonic machine (Series 10, Sonic-Mill, Albuquerque, NM, USA). Figure 2.1 shows a schematic of the experimental setup. It consists of an ultrasonic spindle system, a data acquisition system, and a coolant system. An ultrasonic spindle, a power supply, an electric motor, and a control panel comprised the ultrasonic spindle system. The power supply converted the low frequency (60 Hz) electrical supply into a high frequency (20,000 Hz) AC output. This AC output was converted into mechanical vibration by the piezoelectric transducer in the ultrasonic spindle. The coolant system provided coolant to the spindle and to the machining interface. The coolant system was comprised of a pump, a coolant tank, a pressure regulator, flow rate and pressure gauges, and valves. Coolant was injected to the interface between the tool and the workpiece to keep them cool. The cutting fluid used was water-soluble Quakercool 6010 (Murdock Industrial Supply Co., Wichita, KS, USA). The cutting tool was a core drill with metal-bonded diamond abrasives. The data acquisition system was comprised

of a dynamometer, a charge amplifier, an analog to digital converter, and software to collect cutting force and torque data.

Table 2.10 Input variables and their values

Input variables	Values
Abrasive size (S, mm)	0.02, 0.08, 0.12, 0.16
Abrasive concentration (C)	50, 100, 150

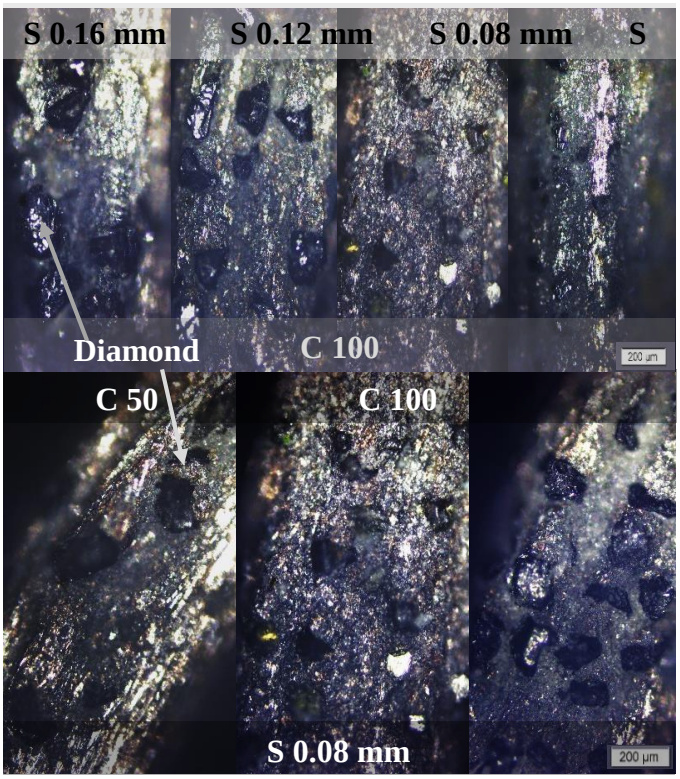

Figure 2.28 Microscopic images of the diamond abrasives at the tool end faces

The experiments involved in two input variables: abrasive size and abrasive concentration. Abrasive size represents the average diameter of the abrasive particles. Abrasive concentration is a measurement of the weight of the diamond particles per cubic centimeter. 100 concentration indicates 4.4 carat/cm3. Outer and the inner diameters of the tool were 12 mm and 10 mm, respectively and its bond type was type B. The abrasive size and concentration are listed in Table 2.10. In order to experimentally investigate the effects of abrasive size on output variables in this

study, abrasive concentration was fixed at 100. Similarly, to study the effect of abrasive concentration, abrasive size was fixed at 0.08 mm. Figure 2.28 shows the microscopic images of the diamond abrasives at the tool end faces. Other process variables: ultrasonic power (percentage of ultrasonic power that controls ultrasonic vibration amplitude), tool rotation speed and feedrate were fixed at 40% (200 W), 3000 rpm, and 0.3 mm/s, respectively.

2.4.2.3 Measurement procedure for cutting force and torque

A dynamometer (Kistler 9272, Kistler Instrument Corp, Switzerland) was used to measure the cutting force along the tool axis (feedrate direction) and the torque. The workpiece was mounted on top of the fixture on the dynamometer. Bolts were used to attach the dynamometer to the machine table as shown in Figure 2.1. A charge amplifier (Kistler 5070, Kistler Instrument Corp, Switzerland) was used to amplify the signal from the dynamometer, and an analog to digital converter (PCIM-DAS 1602/16, Measurement Computing Corporation, Norton, MA, USA) was used to convert that signal into a numerical signal. Dynoware software (Version 2.4.1.6 type 2825A-02, Kistler Instrument Corp, Switzerland) was used to collect cutting force and torque data. The maximum cutting force and the maximum torque obtained during the experiment were reported in this study.

2.4.2.4 Measurement Procedure for surface roughness

A surface profilometer (Mitutoyo SJ-400, Mitutoyo Corporation, Kanagawa, Japan) was used to measure the surface roughness. The sampling range and cut-off length were set at 4 mm and 0.8 mm, respectively, and the surface roughness was characterized by the average surface roughness (Ra). RUM produced a hole and a rod after each drilling process, and the surface

roughness was measured on the cylindrical surface of the drilled rod at the entrance and the exit locations along the axial direction of the extracted rod. Four measurements were taken at each quadrant, as shown in Figure 2.2. Eight Ra values were obtained for each test. Table 2.13 shows the average values of the measurements.

2.4.3 Experimental results

2.4.3.1 Effects on cutting force

The effects of abrasive size and abrasive concentration on cutting force were studied and Table 2.11 shows the experimental results of cutting force. The average cutting forces are presented with the corresponding standard deviations as the error bars.

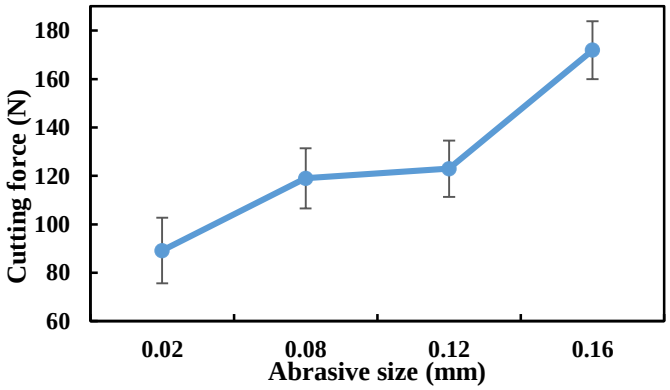

Figure 2.29 Effects of abrasive size on cutting force

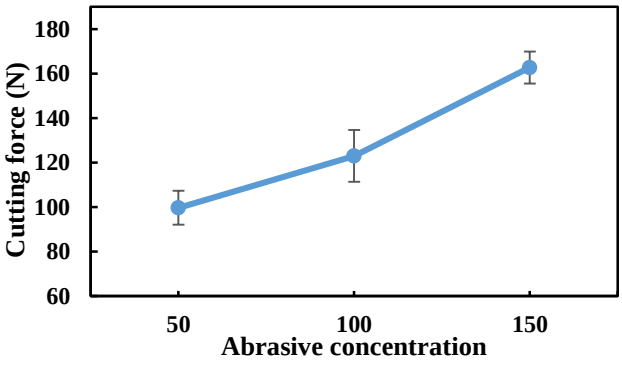

Figure 2.30 Effects of abrasive concentration on cutting force

Table 2.11 Experimental results on cutting force

Input variables		Cutting force (N)	Average cutting force (N)
Abrasive size (mm)	0.02	87.46	89.17
		106.63	
		73.43	
	0.08	118.38	118.99
		134.49	
		104.1	
	0.12	106.57	123.00
		131.84	
		130.59	
	0.16	170.96	171.92
		157.75	
		187.04	
Abrasive concentration	50	103.7	99.68
		106.35	
		88.99	
	100	106.57	123.00
		131.84	
		130.59	
	150	153.14	162.73
		170.38	
		164.67	

As shown in Figure 8, cutting force increased as abrasive size increased. This result is consistent with the reported study of a mechanistic predictive model for cutting force on RUM of CFRP [22]. In the model study, Cong et al. reported that impact force of abrasive particles increased as abrasive size increased, hence increasing the cutting force but their predicted cutting force decreased as abrasive size increased [22]. The reason for the reduction in cutting force was the consideration of decrement in number of abrasive particles involved in cutting, as increased of the abrasive size [22]. The same trend in Cong et al's modelling study has been reported by other studies when RUM if applied to machine silicon carbide [16, 22].

The increment of cutting force from abrasive size 0.08 mm to 0.12 mm was the lowest increment compared with other consecutive levels of abrasive sizes. Effects of abrasive sizes 0.08 mm and 0.12 mm on cutting force were statistically insignificant due to the same variability. The highest increment of cutting force was observed when abrasive size increased from 0.12 mm to 0.16 mm since this consecutive sizes of abrasives had the largest difference in surface area of abrasive particles (abrasive particles were considered as spheres when calculating the surface area).

As shown in Figure 2.30, cutting force increased as abrasive concentration increased. The increment of cutting force when abrasive concentration increased from 50 to 100 was smaller than to that when abrasive concentration increased from 100 to 150. According to the reported study, cutting force increased as abrasive concentration increased and that study mentioned the nonlinear relationship between cutting force and abrasive concentration [22].

2.4.3.2 Effects on torque

The effects of abrasive size and abrasive concentration on torque were studied. Table 2.12 presents the experimental results on torque. The average torques are presented with the corresponding standard deviations as the error bars. According to Figure 2.31, torque decreased as abrasive size increased from 0.02 – 0.12 mm; however, torque dramatically increased at abrasive size of 0.16 mm. Effects of abrasive sizes from 0.02 – 0.12 mm on torque were statistically insignificant due to the common range of variability. As shown in Figure 2.32, abrasive concentration had insignificant effects on torque. The lowest torque reported when abrasive concentration was 100.

Table 2.12 Experimental results on torque

Input variables		Torque (Nm)	Average torque (Nm)
Abrasive size (mm)	0.02	2.0	1.67
		1.5	
		1.5	
	0.08	1.7	1.63
		1.5	
		1.7	
	0.12	1.5	1.60
		1.7	
		1.6	
	0.16	1.9	1.93
		1.9	
		2.0	
Abrasive concentration	50	1.7	1.63
		1.6	
		1.6	
	100	1.5	1.60
		1.7	
		1.6	
	150	1.7	1.63
		1.6	
		1.6	

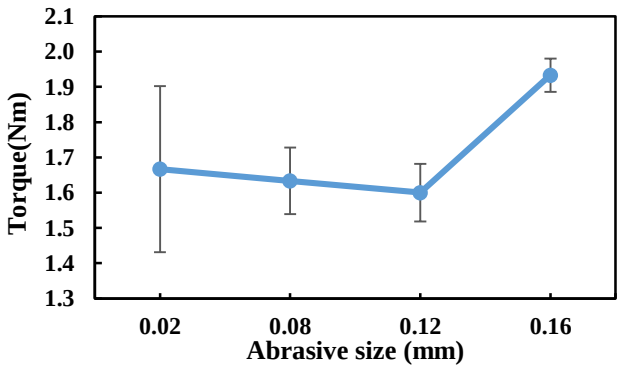

Figure 2.31 Effects of abrasive size on torque

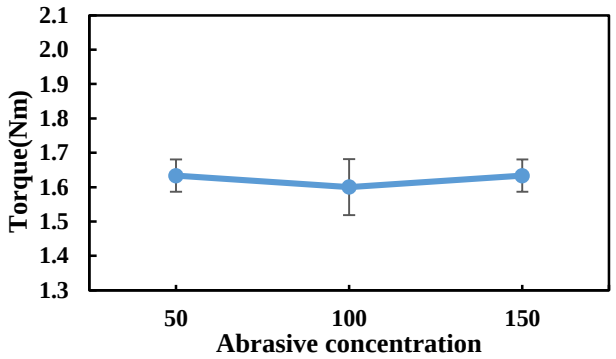

Figure 2.32 Effects of abrasive concentration on torque

2.4.3.3 Effects on surface roughness

The effects of abrasive size and abrasive concentration on surface roughness were studied. Table 2.13 shows the experimental results on surface roughness of the drilled holes. The average surface roughness values were presented with the corresponding standard deviations as the error bars. Reported surface roughness values were associated with large variability due to many reasons such as layered structure of the CFRP, variability of abrasive size and concentration, etc. According to Figure 2.33, the lowest and the highest average surface roughness reported at abrasive size of 0.12 mm and 0.08 mm, respectively. As shown in Figure 2.34 the lowest average surface roughness obtained for abrasive concentration of 100.

Table 2.13 Experimental results of average surface roughness (µm)

Input variables		Average at entrance	Average at exit	Average of the hole
Abrasive size (mm)	0.02	0.71	1.08	0.89
	0.08	1.18	1.37	1.27
	0.12	0.66	0.79	0.73
	0.16	0.85	1.26	1.05
Abrasive concentration	50	1.06	1.35	1.20
	100	0.66	0.79	0.73
	150	0.67	1.22	0.94

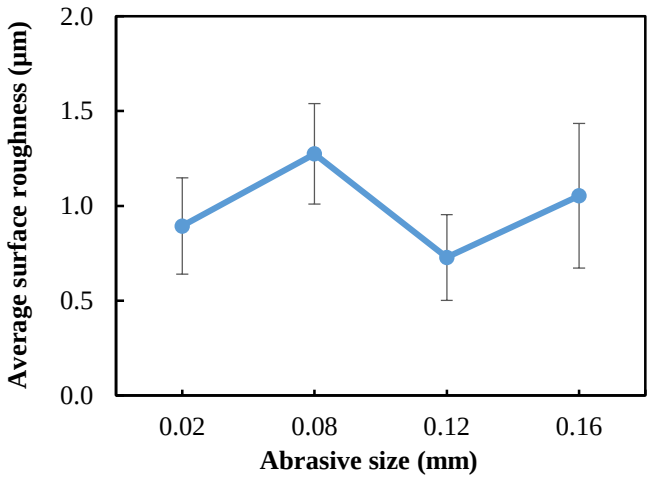

Figure 2.33 Effects of abrasive size on surface roughness

Figures 2.35 and 2.36 show surface roughness at the entrance and the exit of drilled holes. The surface roughness at the exit for all the abrasive sizes and concentrations used in this study was higher than the surface roughness at the entrance. This was consistent with the results obtained by Cong et al. [64]. The reason for this outcome is that at the hole entrance, abrasives on the tool grind the hole surface much longer comparing to the hole exit [64].

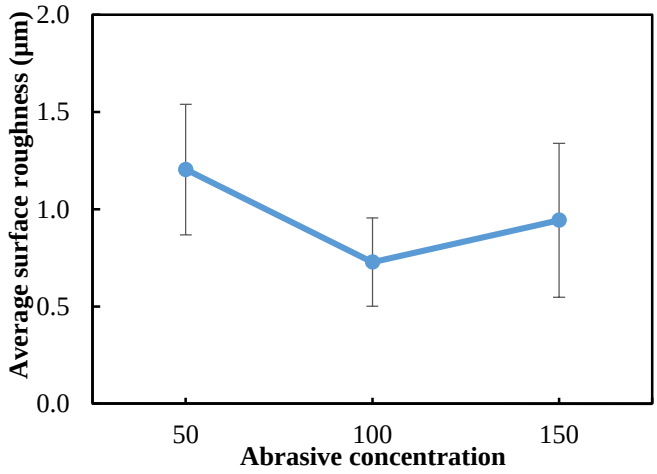

Figure 2.34 Effects of abrasive concentration on surface roughness

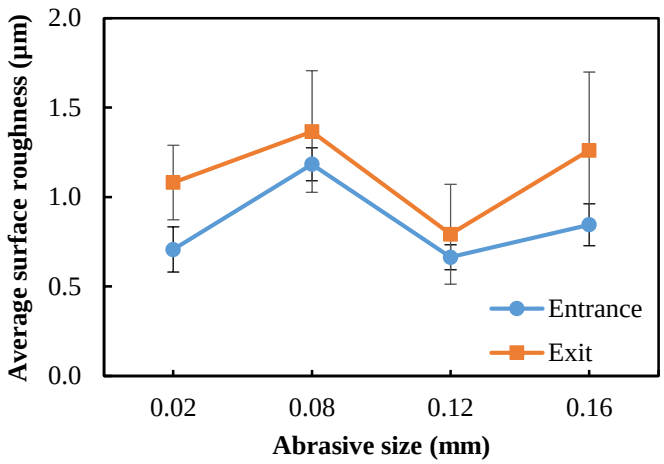

Figure 2.35 Effects of abrasive size on surface roughness at entrance and exit

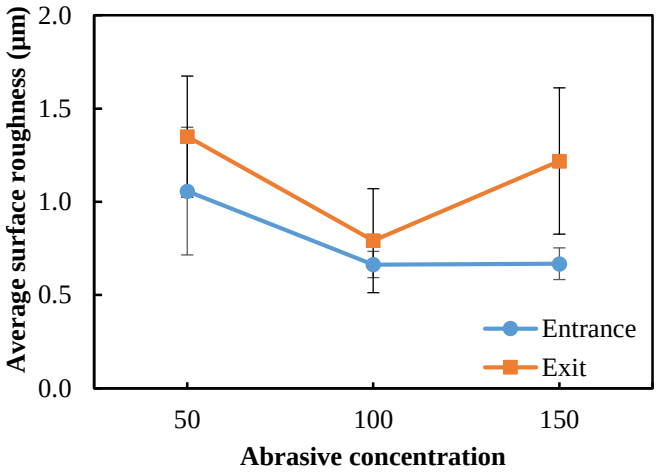

Figure 2.36 Effects of abrasive concentration on surface roughness at entrance and exit

2.4.4 Conclusions

This study, for the first time, reports the effects of abrasive properties (abrasive size and abrasive concentration) on cutting force, torque, and surface roughness on rotary ultrasonic machining (RUM) of carbon fiber reinforced plastic (CFRP). The following conclusions are drawn:

1. Cutting force increased as abrasive size and abrasive concentration increased.

2. Torque increased when abrasive size increased beyond the abrasive size of 0.12 mm, but abrasive concentration had insignificant effects on torque.
3. The average surface roughness at the exit of a drilled hole on CFRP was always greater than that at the entrance.
4. Abrasive size and abrasive concentration had insignificant effects on the average surface roughness of a drilled hole on CFRP.

References

[1]. Mangalgiri, P.D., 1999, "Composite materials for aerospace applications," Bulletin of Materials Science, Vol. 22, pp. 657-664.

[2]. Guu, Y.H., Hocheng, H., Tai, N.H., Liu, S.Y., 2001, "Effect of electrical discharge machining on the characteristics of carbon fiber reinforced carbon composites," Journal of Materials Science, Vol. 36, pp. 2037-2043.

[3]. Arul, S., Vijayaraghavan, L., Malhotra, S.K., Krishnamurthy, R., 2006, "The effect of vibratory drilling on hole quality in polymeric composites," International Journal of Machine Tool & Manufacture, Vol. 46, pp. 252-259.

[4]. Cataldo, F., 2008, "Study on the reinforcing effect of milled carbon fibers in a natural rubber based composite," Journal of Macromolecular Science, Vol. 47, pp. 818-828.

[5]. Hu, S., Hoa, S.V., Ganesan, R., 2009, "A new evaluation method for surface finish of composite automotive panels using waveform analysis," Journal of Composite Materials, Vol. 43, pp. 843-875.

[6]. Palanikumar, K., 2010, "Modeling and analysis of delamination factor and surface roughness in drilling GFRP composites," Materials and Manufacturing Processes, Vol. 25, pp. 1059-1067.

[7]. Liu, Y., Kumar., S., 2012, "Recent progress in fabrication, structure, and properties of carbon fiber," Polymer Reviews, Vol. 52, pp. 234-258.

[8]. Wang, X., Kwon, P.Y., Sturtevant, C., Kim, D., Lantrip, J., 2013, "Tool wear of coated drills in drilling CFRP," Journal of Manufacturing Processes, Vol. 15, pp. 127-135.

[9]. Cong, W.L., Pei, Z.J., Deines, T.W., Srivastava, A., Riley, L., Treadwell, C., 2012, " Rotary ultrasonic machining of CFRP composites: A study on power consumption," Ultrasonics, Vol. 52, pp. 1030-1037.

[10]. Boeing Co, 787 Dreamliner Program Fact Sheet, 2011.<http://www.boeing.com/commercial/787family/ programfacts.page?> accessed July 22nd 2014.

[11]. Cong, W.L., Pei, Z.J., Feng, Q., Deines, T.W., Treadwell, C., 2012, "Rotary ultrasonic machining of CFRP: A comparison with twist drilling," Journal of Reinforced Plastics and Composites, Vol. 31, Issue 5, pp. 313-321.

[12]. Feng, Q., Cong, W.L., Pei, Z.J., Ren, C.Z., 2012, "Rotary Ultrasonic Machining of Carbon Fiber-Reinforced Polymer: Feasibility Study," Machining Science and Technology, Vol. 16, pp. 380-398.

[13]. Hocheng, H., Hsu, C.C., 1995, "Preliminary study of ultrasonic drilling of fiber reinforced plastics," Journal of Material Processing Technology, Vol. 48, pp. 255-266.

[14]. Kumar, J., Khamba, J.S., 2008, "An experimental study on ultrasonic machining of pure titanium using designed experiments," Journal of the Brazilian Society of Mechanical Science and Engineering, Vol. 30, pp. 231-238.

[15]. Kim, K.T., Hong, Y.H., Park, K.H., Choi, Y.J., Lee, S.W., Choi, H.Z., 2012, "An Experimental Investigation of ultrasonic assisted grinding in DOE approach," Advances in Abrasive Technology, Vol. 565, pp. 129.

[16]. Churi, N.J., Nikhi, J., 2007, "Rotary ultrasonic machining of silicon carbide: designed experiments," International Journal of Manufacturing Technology and Management, Vol. 12, Issue 1/2/3, pp. 284.

[17]. Jiao, Y., Ping, P.H., 2005, "Rotary ultrasonic machining of ceramics: design of experiments," International Journal of Manufacturing Technology and Management, Vol. 7, Issue 2/3/4, pp. 192.

[18]. Zhang, C., Feng, P., Pei, Z., Cong, W., 2014, "Rotary ultrasonic machining of sapphire: feasibility study and designed experiments," Key Engineering Materials, Vol. 589-590, pp. 523-528.

[19]. Cong, W.L., Pei, Z.J., Deines, T., 2010, "Rotary ultrasonic machining of stainless steels: empirical study of machining variables," International Journal of Manufacturing Research, Vol. 5, pp. 370-386.

[20]. Wang, Q., Pei, Z.J., Gao, H., Churi, N.J., Kang, R., 2009, "Rotary ultrasonic machining of potassium Dihydrogen phosphate (KDL) crystal : an experimental investigation," International Journal of Mechatronics and Manufacturing Systems, Vol. 2, pp. 414-426.

[21]. Churi, N.J., Pei, Z.J., Shorter, D.C., 2009, "Rotary ultrasonic machining of dental ceramics," International Journal of Machining and Machinability of Materials, Vol. 6, pp. 270-284.

[22]. Cong, W.L., Pei, Z.J., Sun, X., Zhang, C.L., 2014, "Rotary ultrasonic machining of CFRP: A mechanistic predictive model for cutting force," Ultrasonics, Vol. 54, pp. 663-675.

[23]. Cong, W.L., Feng, Q., Pei, Z.J., Deines, T.W., Treadwell, C., 2012, "Rotary ultrasonic machining of carbon fiber reinforced plastic composites: Using cutting fluid versus cold air as coolant," Journal of Composite Materials, Vol. 46, pp. 1745-1753.

[24]. Teti, R., 2002, "Machining of Composite materials," CIRP Annals-Manufacturing Technology, Vol. 51, pp. 611-634.

[25]. Cheng, H., Dharan, C. K. H., 1990, "Deamination during drilling in composite laminates," Journal of engineering for industry, Vol. 112, pp. 236-239

[26]. Andrews, S.D., Ochoa, O.O., Owns, S.D., 1993, "The effects of fastner hole effects," Journal of composite materials, Vol. 27, pp. 2-20.

[27]. Jain, S., Yang, D.C.H, 1993, "Effects of feedrate and chisel edge on delamination in composites drilling," Journal of engineering for industry, Vol. 115, pp. 398-405

[28]. Jain, S., Yang, D.C.H, 1994, "Delamination free drilling of composite laminates," Journal of engineering for industry, Vol. 116, pp. 475-481.

[29]. Park, K.Y., Choi, J.H., Lee, D.G., 1995, "Delamination-free and high-efficiency drilling of CFRP," Vol. 29, pp. 1988-2002.

[30]. Stone, R., Krishnamurthy, K., 1996, "A neural network thrust force controller to minimize delamination during of graphite-epoxy laminates," International journal of machine tools & manufacture, Vol. 36, pp. 985-1003.

[31]. Chen, W.C., 1997, "Some experimental investigations in the drilling of carbon fiber-reinforced plastic," International journal of machine tools & manufacture, Vol. 37, pp. 1097-1108.

[32]. Upadhyay, P.C., Lyons, J.S., 1999, "On the evaluation of critical thrust for delamination-free drilling of composite laminates," Journal of reinforced plastics and composites, Vol. 18, pp.1287-1303.

[33]. Piquet, R., Ferret, B., Lachaud, F., Swider, P., 2000, "Experimental analysis of drilling damage in thin carbon-epoxy plate using special drills," Composites, Vol. 31, pp. 1107-1115.

[34]. Davim, J. P., Reis, P., 2003, "Drilling carbon fiber reinforced plastics manufactured by autoclave experimental and statistical study," Materials and design, Vol.24, pp. 315-324.

[35]. Davim, J. P., Reis, P., 2003, "Study of delamination in drilling carbon fiber reinforced plastics (CFRP) using design experiments," Composite structures, Vol. 59, pp. 481-487.

[36]. Hocheng, H., Tsao,C. C., 2005, "The path towards delamination-free drilling of composite materials," Journal of materials processing technology, Vol. 167, pp. 251-264.

[37]. Gaitonde, V.N., Karnik, S.R., Rubio, J.C., Correia, A.E., Abrao, A.M., 2008, "Analysis of parametric influence on delamination in high-speed drilling of carbon fiber reinforced plastic composites," Journal of materials processing technology, Vol. 203, pp.431-438.

[38]. Faraz, A., Heymann, T., Biermann, D., 2011, "Experimental Investigations on Drilling GFRP Epoxy Composite Laminates Using Specialized and Conventional Uncoated Cemented Carbide Drills," Vol. 26, pp. 609-617.

[39]. Gaitonde, V.N., Karnik, S.R., Rubio, J.C., Correia, A.E., Abrao, A.M., Davim, P.J., 2011, "A study aimed at minimizing delamination during drilling of CFRP composites," Journal of composite materials, Vol. 45, pp. 2359-2368.

[40]. Cong, W.L., Pei, Z.J., Deines, T.W., Liu, D.F., Treadwell, C., 2014, " Rotary ultrasonic machining of CRP/Ti stacks: using variable feedrate," Composite Part B, Vol. 52, pp. 303-310.

[41]. Salama, A., Li, L., Mativenga, P., Sabli, A., 2016, “High-power picosecond laser drilling/machining of carbon fiber-reinforced polymer (CFRP) composites,” Applied Physics A, Vol. 122.

[42]. Zhao, K., Jia, Z., Liu, W., Ma, J., Wang, L., 2015, “ Material removal with constant depth in CNC laser milling based on adaptive control of laser fluence,” International Journal of Advanced Manufacturing Technology, Vol. 77, pp. 797-806.

[43]. Alberdi, A., Suarez, A., Artaza, T., Palafox, G. A. E., Ridgway, K., 2013, “ Composite cutting with abrasive water jet,” Procedia Engineering, Vol. 63, pp. 421-429.

[44]. Danford, M., 2008, "Drill deletes delamination in CFRP," Modern Machine Shop, Vol. 81, pp. 22-24.

[45]. Shyha, I.S., Aspinwall, D.K., Soo, S.L., Bradley, S., 2009, "Drill geometry and operating effects when cutting small diameter holes in CFRP," International Journal of Machine Tools and Manufacture, Vol. 49, pp. 1008-1014.

[46]. Schulze, V., Becke, C., 2011, "Machining strategies for hole making in composites with minimal workpiece damage by directing the process forces inwards," Journal of Materials Processing Technology, Vol. 211, pp. 329-338.

[47]. Lsbilir, O., Ghassemieh, E., 2012, "Delamination and wear in drilling of carbon-fiber reinforced plastic composites using multilayer TiALN/TiN PVD-coated tungsten tools," Journal of Reinforced Plastics and Composites, Vol. 31, pp. 717-727.

[48]. Zitoune, R., Krishnaraj, V., Almabouacif, B.S., Collombet, F., Sima, M., Jolin, A., 2012, "Influence of machining parameters and new nano-coated tool on drilling performance of CFRP/Aluminum sandwich," Composites, Vol. 43, pp. 1480-1488.

[49]. Kumar, M.S., Prabukarthi, A., Krishnaraj, V., 2013, "Study on tool wear and chip formation during drilling carbon fiber reinforced polymer (CFRP)/Titanium alloy (Ti6A14V) stacks," International Conference on Design and manufacturing, Vol. 64, pp. 582-592.

[50]. Zhang, J.G., Wang, X.C., Shen, B., Sun, F.H., 2013, "Effect of boron and silicon doping on improving the cutting performance of CVD diamond coated cutting tools in machining CFRP," International Journal of Refractory Metals and Hard Materials, Vol. 41, pp. 285-292.

[51]. Xu, J., An, Q., Chen, M., 2014, "A comparative evaluation of polycrystalline diamond drills in drilling high-strength T800S/250F CFRP," Composite Structures, Vol. 117, pp. 71-82.

[52]. Tsao, C.C., Chiu, Y.C., 2011, "Evaluation of drilling parameters on thrust force in drilling carbon fiber reinforced plastic (CFRP) composite laminates using compound core-special drills," International Journal of Machine Tools and Manufacture, Vol. 51, pp. 740-744.

[53]. Wang, J., Feng, P., Zheng, J., Zhang, J., 2016, “Improving hole exit quality in rotary ultrasonic machining of ceramic matrix composites using a compound step-taper drill,” Ceramics International, Vol. 42, pp. 13387-13394.

[54]. Mayuet, P., Gallo, A., Portal, A., Arroyo, P., Alvarez, M., Marcos, M., 2013, "Damaged area based study of the Break-in and break-out defects in the dry drilling of carbon fiber reinforced plastics (CFRP)," The Manufacturing Engineering Society International Conference, Vol. 63, pp. 743-751.

[55]. Park, K.H., Beal, A., Kim, D., Kwon, P., Lantrip, J., 2011, "Tool wear in drilling of composite/titanium stacks using carbide and polycrystalline diamond tools," Wear, Vol. 271, pp. 2826-2835.

[56]. Schulze, V., Becke, C., 2011, "Analysis of machining strategies for fiber reinforced plastics with regard to process force direction," Conference on Surface Integrity, Vol. 19, pp. 312-317.

[57]. Khashaba, U.A., El-Sonbaty, I.A., Selmy, A.I., Megahed, A.A., 2012, "Drilling analysis of woven glass fiber-reinforced/epoxy composites," journal of Composite Materilas, Vol. 47, pp. 191-205.

[58]. Khashaba, U.A., 2004, "Delamination in drilling GFR-thermoset composites," Composite Structures, Vol. 63, pp. 313-327.

[59]. Qin, N., Pei, Z.J., Cong, W.L., Guo, D.M., 2010, "Effects of tool design on edge chipping in ultrasonic-vibration-assisted grinding," International Manufacturing Science and Engineering Conference, pp. 147-154.

[60]. Jiao, Y., Liu, W.J., Pei, Z.J., Xin, X.J., 2005, "Study on edge chipping in rotary ultrasonic machining of ceramics: an integration of designed experiments and finite element method analysis," Journal of Manufacturing Science and Engineering, Vol. 127, pp. 752-758.

[61]. Black, J. T., Kohser, R. A., 2012, Chapter 23 Drilling and related hole-making processes, Materials and processes in manufacturing, John Wiley & Sons, Inc, USA.

[62]. Fernando, P.K.S.C, Pei, Z.J., Zhang, M., Song, X., 2015, "Rotary ultrasonic machining of carbon fiber-reinforced plastics: a design of experiment," International Manufacturing Science and Engineering Conference, Vol. 1.

[63]. Bhushan, B., 2013, "Introduction to tribology," Second edition, John Wiley and Sons, Ltd.

[64]. Cong, W. L., Pei, Z. J., Deines, T. W., Zhang, P.F., 2013, “Surface roughness in rotary ultrasonic machining: hypotheses and their testing via experiments and simulations,” International Journal of Manufacturing Research, Vol. 8, pp. 378-393.

Chapter 3 - K9 Glass – An experimental investigation on intermittent and continuous rotary ultrasonic machining

Paper title:

Intermittent and Continuous Rotary Ultrasonic Machining of K9 Glass: An Experimental Investigation

Published in:

Journal of Manufacturing and Materials Processing, Vol. 1, pp. 20

Authors' names:

Fernando, P.[1], Zhang, M.[1], Pei, Z.J.[2], Cong, W.[3]

Authors' affiliations:

1. Department of Industrial and Manufacturing Systems Engineering, Kansas State University, Manhattan, KS 66506, USA
2. Department of Industrial and Systems Engineering, Texas A & M University, College Station, TX 77843 USA
3. Department of Industrial Engineering, Texas Tech University, Lubbock, TX 79409, USA

3.1 Introduction

K9 glass, also known as BK7 or borosilicate crown glass, has excellent optical performance due to its bubble-free structure and low inclusions [1]. K9 glass has been used as a representative functional material in many applications, such as optics, electronics, thermodynamics, fluidics, and so on. [2]. K9 glass is regarded as a difficult-to-machine material due to its mechanical properties, such as high hardness, high strength, and low fracture toughness [3]. Other material properties that give K9 glass a broad application include its low density, high thermal resistance, and good resistance to corrosion and wear.

Some material processing techniques have been reported on machining of K9 glass. Gu et al. used a diamond grinding wheel to study four grinding modes: brittle mode, semi-brittle mode, semi-ductile mode and ductile mode in horizontal surface grinding of K9 glass [4]. Park et al. investigated micro machining of K9 glass by using micro-abrasives, which were accelerated by compressed air to form linear grooves and holes with width and diameter of 80 μm [5]. Matsumura et al. reported the use of abrasive water jet to make grooves of 20–100 μm wide on glass [6]. Rotary ultrasonic machining (RUM) has also been applied to K9 glass machining [3,7–9]. Paragraphs that follow will give more details about the state-of-the-art of RUM application to K9 glass machining. Figure 3.1 shows an illustration of this process and microscopic pictures of machined surface, cutting interface, and cutting chips of K9 glass.

Zhang et al. did a feasibility study on RUM of K9 glass [3]. They revealed that RUM can drill holes on K9 glass with compressed air as coolant [3]. Zhang et al. also investigated rotary ultrasonic face milling of K9 glass and studied its material removal mechanism [13]. It is reported that, comparing to diamond milling, rotary ultrasonic face milling reduced surface damage depth, chipping size, and lateral cracks [3].

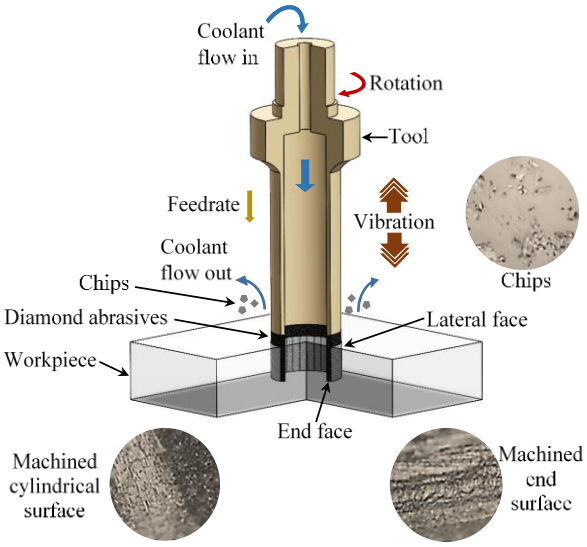

Figure 3.1 Illustrations of Rotary ultrasonic machining (RUM) and microscopic pictures of machined surface, cutting interface, and cutting chips of K9 glass

Lv et al. investigated RUM of K9 glass and reported a study of scratch test to obtain damage patterns in the stage of high strain rate [7]. In their study, they discussed kinematic principles of the abrasives. Material strain rate effects based on the indentation mechanics theory were also studied in Lv et al.'s study [7]. Lv et al. also studied the surface formation mechanisms and conducted experimental investigations on subsurface damage, including the relationship between subsurface damage and surface roughness, subsurface damage depth and its distribution in RUM and conventional grinding of K9 glass [8,9,14,15]. They did another study to attain influences of high-frequency vibration on tool wear in RUM of K9 glass [16].

RUM is merited for providing good surface finish. In order to reduce the hole surface roughness, it is important to have an efficient way to flush the swarf away. RUM employs liquid coolant or compressed air to flush the swarf in between the tool and workpiece away [17]. Intermittent rotary ultrasonic machining (intermittent RUM) is a newly introduced machining process. The main difference between these two RUM processes is that intermittent RUM uses a slotted cutting tool (metal bonded diamond core drill) instead of a common metal bonded diamond

core cutting tool (without slots) in continuous RUM. Regarding swarf flushing, intermittent RUM provides a higher coolant flow rate [18]. Zeng et al. did an experimental investigation on intermittent rotary ultrasonic machining of alumina (92% hot-pressed) [18]. They compared output coolant flowrate and surface quality between continuous RUM and intermittent RUM. They found that coolant flowrate was increased and surface quality was improved significantly by using intermittent RUM [18]. But there was no significant difference in cutting force by using intermittent RUM compared to continuous RUM [18].

In RUM studies, results were also obtained and analyzed through mathematical modeling. Chowdhury et al. conducted an experiment by drilling high precision holes in Ti6Al4V using RUM and constructed a set of possibility distributions in order to represent the uncertainty in the output variables to determine the effects of the input variables on output variables quantitatively [19].

This study, for the first time, conducts intermittent RUM on K9 glass, and compares its performance against continuous RUM from the perspectives of cutting force, surface roughness, and chipping size. The remainder of this paper presents as follows. Section 2 provides experimental conditions and measurement procedures. Experimental results including effects on cutting force, surface roughness, and edge chipping are described in Section 3. Section 4 presents conclusions drawn from this study.

3.2 Material, Experimental Set-Up and Measurement Procedures

3.2.1 Material

The workpiece was K9 glass with the size of 40 mm × 30 mm × 5 mm. The properties of workpiece are listed in Table 3.1.

Table 3.1 Properties of K9 glass [20]

Property	Unit	Value
Density	g/cm^3	2.5
Young's modulus	GPa	85.9
Poisson's ratio	-	0.28
Vickers hardness	GPa	7.2
Fracture toughness	$MPa \cdot m^{1/2}$	0.8

3.2.2 Experimental set-up

The experiments were conducted on a rotary ultrasonic machine (Series 10, Sonic-Mill, Albuquerque, NM, USA). As illustrated in Figure 2.1, rotary ultrasonic machining set-up mainly consisted of an ultrasonic spindle system, a coolant system, and a data acquisition system. The ultrasonic spindle, a power supply, an electric motor, a control panel, and a hydraulic feeding device (not shown in the figure) comprised the ultrasonic spindle system. The power supply converted electrical input of 110 V and 50–60 Hz signal in to 20,000 Hz electrical signal which fed to a piezoelectric device that located at inside of the ultrasonic spindle. Then piezoelectric device converted 20,000 Hz signal into high frequency mechanical vibration, namely ultrasonic vibration. That low amplitude ultrasonic vibration was amplified by the acoustic horn located in the ultrasonic spindle and delivered to the cutting tool. Amplitude of the vibration is mainly depending on the output level of the power supply. Rotation of the spindle was provided by the electric motor located on top of the spindle. The coolant system included a coolant tank, a pump, valves, flowrate and pressure gauges, and pressure regulators. The data acquisition system contained a dynamometer (Model 9272, Kiestler Inc., Winterthur, Switzerland), a charge amplifier (Model 5070, Kiestler Inc., Winterthur, Switzerland), an analog to digital converter, a data acquisition card (PC-CARD-DAS16/16), and a computer with software (Type 2815A, Kiestler Inc., Winterthur, Switzerland).

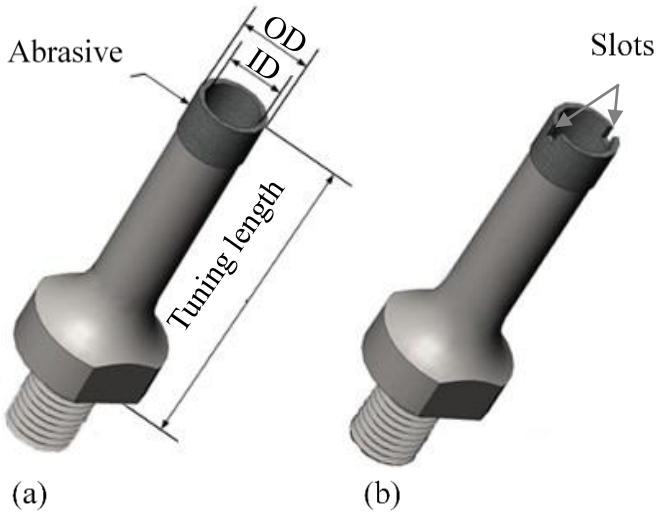

Figure 3.2 Illustration of cutting tools

(a) Tool in continuous RUM (b) Tool in intermittent RUM

Experiments were conducted using metal-bonded diamond core drills as illustrated in Figure 3.2. Figure 3.2 (a) shows a metal-bonded diamond cutting tool without slots for continuous RUM, and Figure 3.2 (b) shows a slotted metal-bonded diamond cutting tool for intermittent RUM. Their outer and inner diameters (OD and ID) were 9 mm and 7 mm, respectively. Four input variables (cutting tool: intermittent and continuous, ultrasonic power, tool rotation speed, and feedrate) were studied during the experiment and the experimental design is shown in Table 3.2. Ultrasonic power was presented as the percentage at ultrasonic power supply.

Table 3.2 Experimental conditions

Input Variable	Values
Ultrasonic power (%)	0; 10; 20; 30; 40; 50
Tool rotation speed (rpm)	2000; 3000; 4000; 5000
Feedrate (mm/s)	0.01; 0.02; 0.03; 0.04

3.2.3 Measurement procedures

Cutting force in the axial direction was measured by using a dynamometer. A charge amplifier was used to amplify the signal of cutting force from the dynamometer, and an analog to digital converter was used to convert the signal. Cutting force data was collected by the Dynoware software (Type 2815A, Kisler Inc., Winterthur, Switzerland).

A surface profilometer (Surftest-402, Mitutoyo Corporation, Kanagawa, Japan) was used to measure the surface roughness of the holes. Test range and cut-off length were set at 4 mm and 0.8 mm, respectively. Surface roughness of a hole was measured at the entrance and the exit locations along the axial direction of the hole and characterized by average surface roughness (Ra). Four measurements were taken at each quadrant. The reported Ra value was the average of eight collected data.

Figure 3.3 illustrates the edge chipping in RUM of K9 glass. RUM uses core drill as the tool, so drilling a hole also produces a cylindrical disk-shape core at the same time and the core is addressed as the machined disk. Edge chipping thickness was measured on the machined disk by using a microscope (Model BX51M Olympus Inc., Tokyo, Japan) as illustrated in Figure 3.4. The microscope has high resolving power along its longitudinal axis, referred as depth of focus (DOF). Based on DOF, edge chipping thickness was measured with the assistance of fine-adjustment of the microscope. The K9 machined disc was placed flat on the adjustable table of the microscope, then the fluorescent lamp was turned on. The corresponding reading of the fine adjustment was noted down after focused on the edge of the exit surface. According to the same procedure, the reading of the fine adjustment was taken after focus on the uppermost surface of the chipping area. Edge chip thickness was calculated by the difference of the two readings on the fine adjustment.

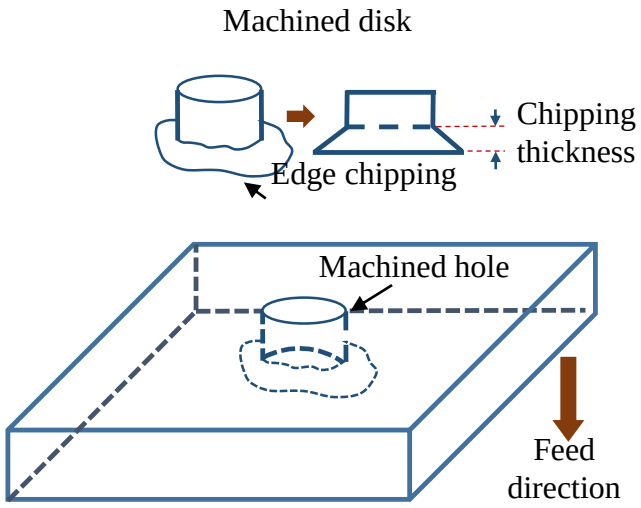

Figure 3.3 Illustration of edge chipping

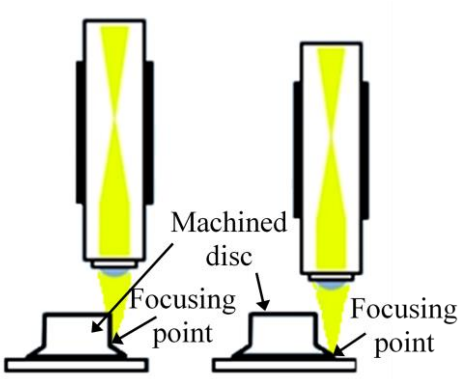

Figure 3.4 Illustration of the measurement of chipping size (thickness) on a microscope

3.3 Experimental results

3.3.1 Effects on cutting force

Cutting force is one of the main output variables, since it is associated with tool wear, cutting temperature, surface roughness, and torque [21, 22]. Figure 3.5 (a) shows a comparison of cutting force between intermittent and continuous RUM. Figure 3.5 presents the average value of the cutting force of three holes drilled on K9 glass under the same condition. It can be seen that cutting force of intermittent RUM was always lower than that of continuous RUM. However,

previous intermittent RUM study of alumina reported that cutting force has no significant difference compared with cutting force of continuous RUM [18].

Cutting force decreased with the increase of ultrasonic power for both intermittent and continuous RUM. The difference in cutting force between intermittent and continuous RUM was larger at lower ultrasonic power levels.

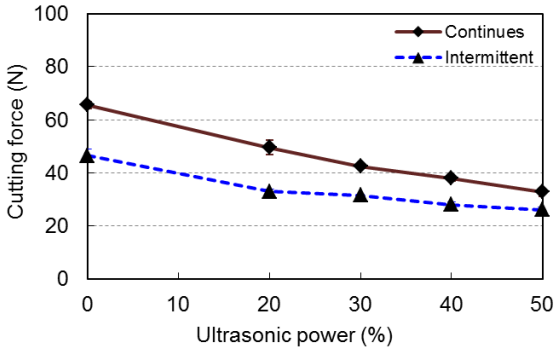

(a)

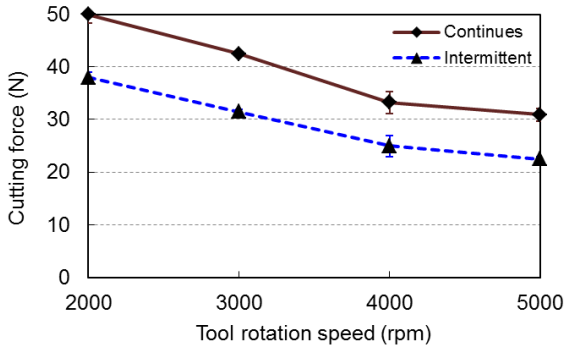

(b)

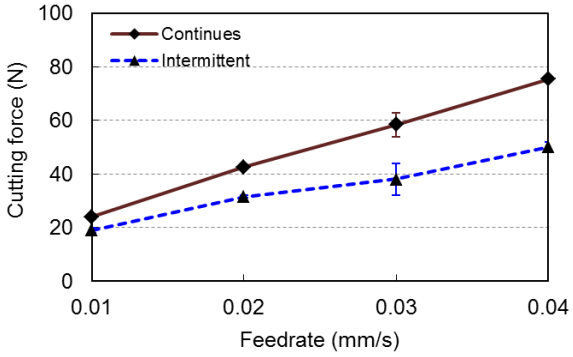

(c)

Figure 3.5 Effects of input variables on cutting force

(a) Effects of ultrasonic amplitude; (b) Effects of tool rotation speed; (c) Effects of feedrate.

According to the Figure 3.5 (b), cutting force of intermittent RUM is lower than that of continuous RUM at the same tool rotation speed. Cutting force of both intermittent RUM and continuous RUM decreased as tool rotation speed increased. As shown in Figure 3.5 (c), cutting force of both intermittent and continuous RUM increased with the increase of feedrate. The difference in cutting force between intermittent and continuous RUM became larger as feedrate increased.

3.3.2 Effects on Surface Roughness

Figure 3.6 shows the effects of ultrasonic power, tool rotation speed, and feedrate on surface roughness. Surface roughness of intermittent RUM was higher than the surface roughness of continuous RUM except for that at 50% ultrasonic power. This is not consistent with the outcome of the study of intermittent RUM by Zeng et al., which reported that surface roughness of machined hole decreased significantly by using intermittent RUM compared to continuous RUM [3].

As shown in Figure 3.6 (a), in continuous RUM, the lowest and the highest surface roughness were obtained at 20% and 50% ultrasonic power, respectively. According to Figure 3.6 (b), surface roughness of continuous RUM decreased as tool rotation speed increased. However, surface roughness of intermittent RUM increased with the increase of tool rotation speed beyond 3000 rpm. The difference in surface roughness between intermittent RUM and continuous RUM was enlarged as tool rotation speed increased. It can be seen from Figure 3.6 (c), for both intermittent and continuous RUM, surface roughness increased with the increase of feedrate. The

difference in surface roughness between intermittent RUM and continuous RUM did not change much as feedrate increased.

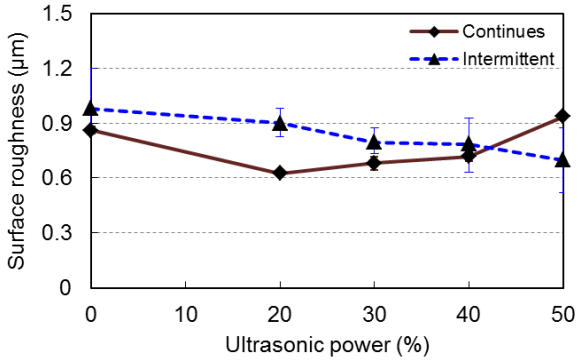

(a)

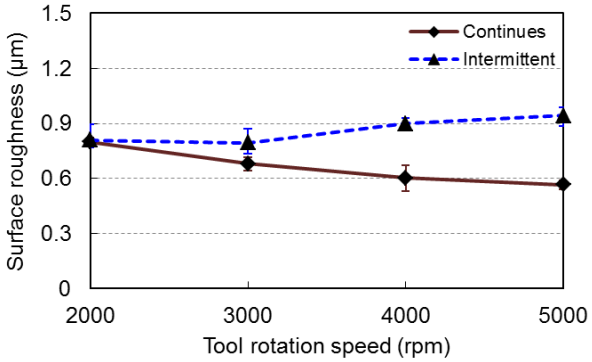

(b)

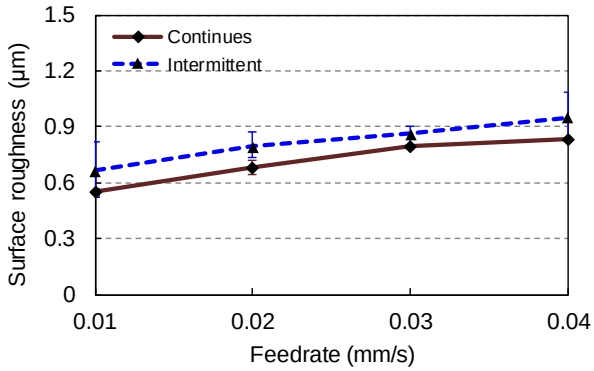

(c)

Figure 3.6 Effects on surface roughness

3.3.3 Effects on Edge Chipping

A comparison of edge chipping size between the two types of RUM is shown in Figure 3.7. According to Figures 3.7, the chipping size of intermittent RUM was smaller than that of continuous RUM. The chipping size decreased as ultrasonic power increased for both continuous and intermittent RUM. The difference in chipping size was larger at lower ultrasonic power levels. According to Figure 3.7 (b), chipping size decreased with the increase of tool rotation speed for both RUM. The lowest chipping size was obtained for intermittent RUM at the tool rotation speed of 3000 rpm. As shown in Figure 3.7 (c), chipping size increased as feedrate increased. The difference in chipping size between intermittent RUM and continuous RUM did not change much as feedrate increased beyond 0.02 mm/s.

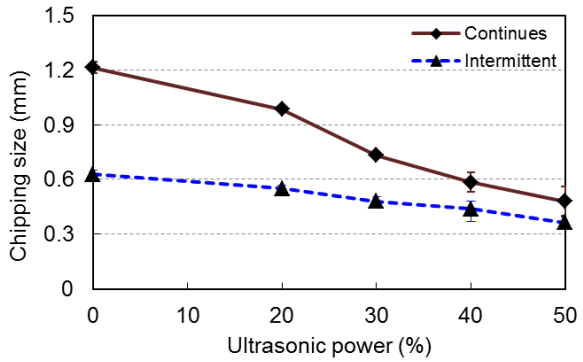

(a)

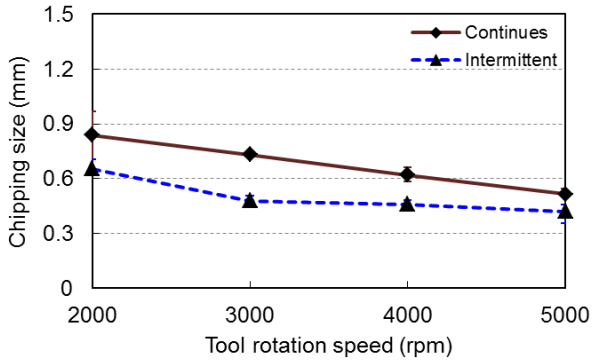

(b)

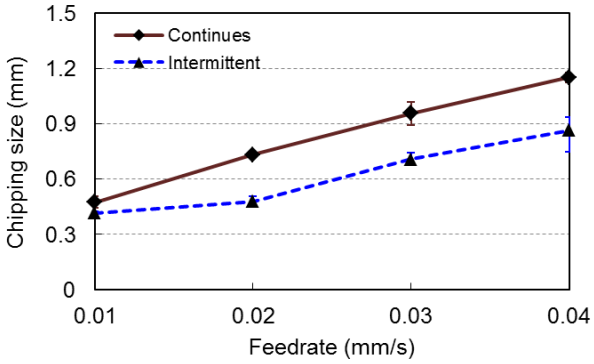

(c)

Figure 3.7 Effects on edge chipping

(a) Effects of ultrasonic amplitude; (b) Effects of tool rotation speed; (c) Effects of federate.

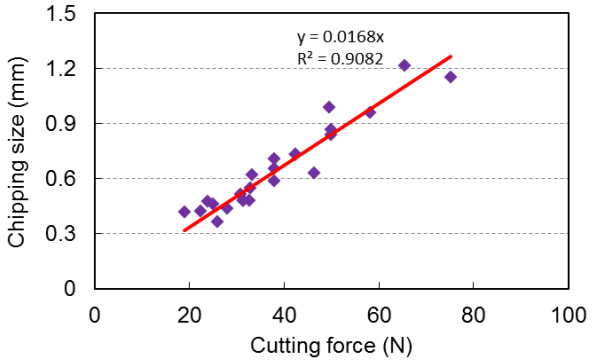

Figure 3.8 Relationship between cutting force and chipping size

Figure 3.8 shows the relationship between cutting force and chipping size. The fitted regression line ($y = 0.0168x$) graphically shows the expecting chipping size to cutting force. The coefficient of "x" indicates that the expecting chipping size increases by average of 0.0168 mm for the increment per cutting force. The coefficient of determination obtained for this model fitting is $R^2 = 0.9082$.

3.4 Conclusions

This paper, for the first time, reported an experimental investigation of rotary ultrasonic machining of K9 glass using both intermittent and continuous RUM. Effects of ultrasonic power, tool rotation speed, and feedrate on cutting force, surface roughness, and chipping size were compared. The following conclusions are drawn:

1. Using intermittent RUM led to a lower cutting force than using continuous RUM in K9 glass machining.
2. Compared to the continuous RUM, intermittent RUM didn't improve the surface roughness of drilled holes.
3. Chipping size in intermittent RUM was smaller than that in continuous RUM when other input variables stayed constant.
4. It was observed that higher cutting force resulted in a larger chipping size, and this relationship was close to linear.

References

[1]. Gu, W., Yao, Z., 2011, "Evaluation of surface cracking in micron and sub-micron scale scratch tests for optical glass BK7", Journal of Mechanical Science and Technology, Vol. 25, pp. 1167-1174.

[2]. Choi, J.P., Jeon, B.H., Kim, B.H., 2007, "Chemical-assisted ultrasonic machining of glass", Journal of Materials Processing Technology, Vol. 191, pp. 153-156.

[3]. Zhang, C., Cong, W., Feng, P., Pei, Z., 2014, "Rotary ultrasonic machining of optical K9 glass using compressed air as coolant: a feasibility study", Proceedings of the Institution of Mechanical Engineers, Part B: Journal of Engineering Manufacture, Vol. 228, pp. 504-514.

[4]. Gu, W., Yao, Z., Li, H., 2011, “Investigation of grinding modes in horizontal surface grinding of optical glass BK7”, Journal of Materials Processing Technology, Vol. 211, pp. 1629-1636.

[5]. Park, D.S., Cho, M.W., Lee, H., Cho, W.S., 2004, “Micro-grooving of glass using micro-abrasive jet machining” Journal of Materials Processing Technology, Vol. 146, pp. 234-240.

[6]. Matsumura, T., Muramatsu, T., Fueki, S., 2011, “Abrasive water jet machining of glass with stagnation effect”, CIRP Annals – Manufacturing Technology, Vol. 60, pp. 355-358.

[7]. Lv, D., Huang, Y., Wang, H., Tang, Y., Wu, X., 2013, “Improvement effects of vibration on cutting force in rotary ultrasonic machining of BK7 glass”, Journal of Materials Processing Technology, Vol. 213, pp. 1548-1557.

[8]. Lv, D., Huang, Y., Tang, Y., Wang, H., 2013, “Relationship between subsurface damage and surface roughness of glass BK7 in rotary ultrasonic machining and conventional grinding processes”, International Journal of Manufacturing Technology and Management, Vol.67, pp. 613-622.

[9]. Lv, D., Wang, H., Tang, Y., Huang, Y., Li, Z., 2013, “Influences of vibration on surface formation in rotary ultrasonic machining of glass BK7”, Precision Engineering, Vol. 37, pp. 839-848.

[10]. Zeng, W.M., Li, Z.C., Pei, Z.J., Treadwell, C., 2005, “Experimental observation of tool wear in rotary ultrasonic machining of advanced ceramics”, International Journal of Machine Tools and Manufacture, Vol. 45, pp. 1468-1473.

[11]. Prabhakar, D., 1992, “Machining advanced ceramic materials using rotary ultrasonic machining process”, M. S. Thesis, University of Illinois at Urbana-Champaign, IL.

[12]. Hu, P., Zhang, J.M., Pei, Z.J., Treadwell, C., 2002, “Modeling of material removal rate in rotary ultrasonic machining: designed experiments”, Journal of Materials Processing Technology, Vol. 129, pp. 339-344.

[13]. Zhang, C., Feng, P., Zhang, J., Wu, Z., Yu, D., 2012, “Investigation into the rotary ultrasonic face milling of K9 glass with mechanism study of material removal”, International Journal of Manufacturing Technology and Management, Vol. 25, pp. 248-266.

[14]. Lv, D., Tang, Y., Wang, H., Huang, Y., 2013, “Experimental investigations on subsurface damage in rotary ultrasonic machining of glass BK7”, Machining Science and Technology, Vol. 17, pp. 443-463.

[15]. Lv, Dongxi, Wang, Hongxiang, Zhang W., Yin, Z., 2016, “Subsurface damage depth and distribution in rotary ultrasonic machining and conventional grinding of glass BK7”, International Journal of Manufacturing Technology, Vol. 86, pp. 2361-2371.

[16]. Lv, D., 2014, “Influences of high-frequency vibration on tool wear in rotary ultrasonic machining of glass BK7”, International Journal of Advanced Manufacturing Technology, Vol. 84, pp. 1443-1455.

[17]. Cong, W.L., Pei, Z.J., Deines, T.W., Treadwell, C., 2011, “Rotary ultrasonic machining of CFRP using cold air as coolant: feasible regions”, Journal of Reinforced Plastics and Composites, Vol. 30, pp. 899-906.

[18]. Zeng, W., Li, Z., Xu, X., Pei, Z.J., Liu, J., Pi, J., 2007, “Experimental investigation of intermittent rotary ultrasonic machining”, Key Engineering Materials, Vols. 359-360, pp. 425-430.

[19]. Chowdhury, M., Ullah, A., Anwar, S., 2017, “Drilling high precision holes in Ti6Al4V using rotary ultrasonic machining and uncertainties underlying cutting force, tool wear, and production inaccuracies,” Materials, Vol. 10, pp. 1069.

[20]. Wang, J., Zhang, C., Feng, P., Zhang, J., 2016, “A model for prediction of subsurface damage in rotary ultrasonic face milling of optical K9 glass”, International Journal of Manufacturing Technology, Vol. 83, pp. 347-355.

[21]. Cong, W.L., Feng, Q., Pei, Z.J., Deines, T.W., Treadwell, C., 2012, "Rotary ultrasonic machining of carbon fiber reinforced plastic composites: Using cutting fluid versus cold air as coolant", Journal of Composite Materials, Vol. 46, pp. 1745-1753.

[22]. Cong, W.L., Pei, Z.J., Sun, X., Zhang, C.L., 2014, “Rotary ultrasonic machining of CFRP: A mechanistic predictive model for cutting force”, Ultrasonics, Vol. 54, pp. 663-675.

Chapter 4 - Rotary ultrasonic machining of rocks: An experimental and theoretical investigation

4.1 An experimental investigation of rotary ultrasonic machining of rocks

Paper title:

Rotary Ultrasonic Machining of Rocks: An Experimental Investigation

Published in:

Advances in Mechanical engineering, Vol. 10, pp. 1-9

Authors' names:

Fernando, P.[1], Zhang, M.[1], Pei, Z.J.[2],

Authors' affiliations:

1. Department of Industrial and Manufacturing Systems Engineering, Kansas State University, Manhattan, KS 66506, USA
2. Department of Industrial and Systems Engineering, Texas A & M University, College Station, TX 77843 USA

4.1.1 Introduction

Rock drilling is widely used in geoengineering, rock engineering, petroleum engineering, mining, and tunnel engineering [1]. It is also used to collect samples to analyze polar ice sheets and search for life on Mars [2, 3]. During the initial development of rock drilling, the penetration rate was primarily dependent on the power of the drilling machines [4]. Today, however, the limiting factor of penetration rate is the severe tool wear from rock drilling [4, 5] which is caused by the high hardness and abrasiveness of the rocks and the possible long-term exposure to multiple rock types during a single drilling process [6]. If the penetration rate were doubled, the estimated yearly cost of $1,200 million for hard rock drilling in the United States could be significantly reduced by $200-$600 million [7]. Therefore, it is crucial to develop more cost-effective rock drilling processes.

Percussive drilling is the most commonly used drilling method. It has a higher penetration rate than the conventional rotary or diamond drilling [1]. Jiren et al. [8] and Lu et al. [9] studied a new method of rock drilling by combining the traditional mechanical drilling with an assistance of abrasive water jet. This method increased the drilling depth and decreased the axial force, torque, and tool wear [8, 9]. Clydesdale et al. [10] developed a core drill bit for the core drilling of rocks, which reduced the fluid invasion and resulted in a higher penetration rate compared to that when using a conventional polycrystalline diamond compact core bit.

Core drilling produces an annular shape cut, which helps in excavating cylindrical cores. Cylindrical cores, as the expected subsurface scientific samples, are used to explore geologic formations, climate histories, biota, and solar activity in terrestrial and extraterrestrial environments [11]. Future extraterrestrial exploration (i.e., on Mars) requires core drilling to collect materials from the subsurface for scientific analysis [2, 3, 12]. However, extraterrestrial

drilling has many constraints such as the extreme environmental conditions and the necessity of complex autonomous systems to acquire cores [13, 14]. There is a growing interest in Mars exploration mission to acquire and return subsurface samples as solid cores to the earth for further analyze [13]. Recent studies showed that a combination of conventional drilling techniques with ultrasonic vibration can address the key shortcomings of the drilling in planetary exploration missions [12, 15].

Machining processes that employ ultrasonic vibration as an assistance can be divided into two main categories: ultrasonic machining (USM) and rotary ultrasonic machining (RUM). USM removes material by the abrasive particles in the form of slurry that accelerated and vibrated by the tool. The material removal mechanisms of USM are the impact action of abrasive particles and the hammering action of abrasive particles that removes material by micro-chipping and mechanical abrasion. Rotary ultrasonic machining (RUM) is a hybrid of ultrasonic machining and abrasive grinding. The main difference between RUM and USM is that RUM uses a metal bonded diamond abrasive core drill with tool rotation. In addition, Bar-Cohen et al. developed a new ultrasonic drilling and coring device based on USM to drill a wide range of rocks without tool rotation [15]. This device can be performed with low preload (<10 N) and low power (average of 5W consumption) [15].

RUM could offer a great advantage in core drilling for future extraterrestrial exploration as opposed to ultrasonic drilling and coring device and ultrasonic machining because of its hybrid material removal mechanism. However, most of the reported studies on RUM have been related to engineering materials (e.g. stainless steel, titanium alloy, composite materials, ceramic materials, and glass). Since natural rocks represent a large group of brittle materials, and RUM has been successfully applied to the machining of many brittle engineering materials, studying the

feasibility and the material removal mechanism in RUM of natural rocks will broader the application of RUM and in the meanwhile shed light on the study of material removal mechanism based on the brittle fracture criteria.

This investigation reports RUM of natural rocks, which are inhomogeneous materials. This research, for the first time, reports feasibility and experimental studies on this new application. In this study, three types of rock (basalt, marble, and travertine) were used, six input variables (tool rotation speed, feedrate, ultrasonic power, abrasive size, abrasive concentration, and drill bit diameter) were examined, and two output variables (cutting force and surface roughness) were measured. The remainder of this paper is presented as follows: Section 2 lists experimental conditions and procedures including the materials, experimental set-up, design of experiments, and measurement procedures; Section 3 describes experimental results, including the effects of six input variables on cutting force and surface roughness; finally, Section 4 presents conclusions.

4.1.2 Experimental conditions and procedures

4.1.2.1 Workpiece materials and properties

There are three main categories of rocks, sedimentary, metamorphic, and igneous. In this study, three types of rocks were chosen to represent the categories. They were basalt (high strength) from the igneous category, marble (medium strength) from the metamorphic category, and travertine (low strength) from the sedimentary category. Workpiece dimensions were 15 mm × 300 mm × 25 mm. Properties of the three types of rocks are shown in Table 4.1.

Table 4.1 Properties of rocks [20]

Property	Unit	Basalt	Marble	Travertine
Density	kg/m^3	2900 – 3100	2400 – 2700	2700
Moh's hardness	–	6	3 – 4	3 – 4
Abrasion resistance	–	High	Medium	Low
Porosity	–	Low	Low	High

4.1.2.2 Experimental setup and conditions

The experiments were conducted on a rotary ultrasonic machine (Series 10, Sonic-Mill, Albuquerque, New Mexico, USA). Figure 2.1 shows a schematic of the experimental setup, which consists of an ultrasonic spindle system, a coolant system, and a data acquisition system. The ultrasonic spindle system was comprised of an ultrasonic spindle, a power supply, an electric motor, and a control panel. The power supply converted the low frequency (60 Hz) electrical power into a high frequency (20,000 Hz) AC output that was then converted into mechanical vibrations by the piezoelectric transducer in the ultrasonic spindle. The coolant system was comprised of a pump, coolant tank, pressure regulator, flow rate and pressure gauges, and valves and provided coolant to the spindle and the interface of machining. The data acquisition system was comprised of a dynamometer, a charge amplifier, an analog to digital converter, and software to collect cutting force data.

4.1.2.3 Experimental conditions

Six input variables, as listed in Table 4.2, were studied. The effective cutting area (A) of a drill bit is calculated by using the formula: $A = \frac{\pi}{4} \times \left({D_o}^2 - {D_i}^2\right)$, where Do and Di are the outer and inner diameters of a drill bit. Drill bit diameters were selected to keep the difference between the effective cutting areas of two consecutive drill bit diameters about the same.

Experimental conditions are listed in Table 4.3. Abrasive size indicates the average diameter of the abrasives bonded to cutting tool. Abrasive concentration is based on the weight of diamond per cm^3 (the base value of 100 concentration is 4.4 carat/cm^3). Three replicates were used for each experimental condition and the output variables were cutting force and surface roughness.

Table 4.2 Input variables and their levels

Input variable	Unit	Level 1	Level 2	Level 3
Tool rotation speed	rpm	1500	2500	3500
Feedrate	mm/s	0.1	0.3	0.5
Ultrasonic power	%	20	40	60
Abrasive size	mm	0.08	0.12	0.16
Abrasive concentration	-	50	100	150
Drill bit outer, inner diameters (D_o, D_i)	mm	(9,7)	(12,10)	(15,13)
and their effective cutting area (A)	mm^2	25.13	34.56	43.98

Table 4.3 Experiment conditions

Test order	Tool rotation speed (rpm)	Feedrate (mm/s)	Ultrasonic power (%)	Abrasive size (mm)	Abrasive concentration	Drill bit diameter D_o, D_i (mm)
1	1500	0.3	40	0.12	100	12, 10
2	2500	0.3	40	0.12	100	12, 10
3	3500	0.3	40	0.12	100	12, 10
4	2500	0.1	40	0.12	100	12, 10
5	2500	0.5	40	0.12	100	12, 10
6	2500	0.3	20	0.12	100	12, 10
7	2500	0.3	60	0.12	100	12, 10
8	2500	0.3	40	0.08	100	12, 10
9	2500	0.3	40	0.16	100	12, 10
10	2500	0.3	40	0.12	50	12, 10
11	2500	0.3	40	0.12	150	12, 10
12	2500	0.3	40	0.12	100	9, 7
13	2500	0.3	40	0.12	100	15, 13

4.1.2.4 Measurement procedures

A dynamometer (Kistler 9272, Kistler Instrument Corp, Switzerland) was used to measure the cutting force along the tool axis (feedrate) direction, and the workpiece was mounted on top of the fixture of the dynamometer. Bolts were used to attach the dynamometer to the machine table, as shown in Figure 2.1. A charge amplifier (Kistler 5070, Kistler Instrument Corp, Switzerland) was used to amplify the signal from the dynamometer and analog to the digital converter (PCIM-DAS 1602/16, Measurement Computing Corporation, Norton, MA, USA) was used to convert the signal to a digital signal. The cutting force data was recorded by using the Dynoware software (Version 2.4.1.6 type 2825A-02, Kistler Instrument Corp, Switzerland).

Surface roughness of the machined rods was measured by using a surface profilometer (Mitutoyo SJ-400, Mitutoyo Corporation, Kanagawa, Japan). The sampling range was set as 4 mm and the surface roughness was characterized by the average surface roughness value (R_a). Rock drilling by RUM produced a hole and a rod after each drilling process and the surface roughness was measured on the cylindrical surface of the extracted rod at the entrance and exit locations along the axial direction of the rod. Four measurements were taken at each quadrant, as shown in Figure 2.2 and eight Ra values were obtained for each test. The mean and standard deviation of these eight R_a values are reported in this study (Section 3). Table 4.4 lists the average values of the measurements.

4.1.3 Experimental results

4.1.3.1 Effects on cutting force

Cutting force is the predominant output variable in rotary ultrasonic machining. Cutting force has a significant impact on other output variables such as tool wear and cutting temperature

[9, 24]. The maximum cutting force for each test was used in this paper. Table 4.4 presents experimental results on cutting force and surface roughness.

Table 4.4 Experimental results

Run Order	Travertine Cutting Force (N)	Marble Cutting Force (N)	Marble R_a (μm)	Basalt Cutting Force (N)	Basalt R_a (μm)
1	56.11	53.45	2.06	93.02	0.78
2	65.04	39.81	2.10	79.52	0.98
3	50.72	36.53	1.92	61.42	0.78
4	51.50	33.25	1.82	55.31	0.92
5	75.53	47.40	1.81	106.66	0.65
6	53.96	47.40	1.80	60.26	0.95
7	65.42	38.58	2.11	75.18	0.99
8	69.54	64.91	1.67	88.60	1.04
9	63.49	59.12	1.18	96.09	1.03
10	58.34	41.93	1.53	93.75	0.91
11	73.27	54.69	1.15	93.68	0.79
12	39.87	32.89	1.19	71.65	0.80
13	97.83	64.99	1.66	130.66	0.89

The effects of tool rotation speed, feedrate, ultrasonic power, abrasive size, abrasive concentration, and drill bit diameter on cutting force are shown in Figures 4.1 and 4.2 – 4.7. The mean values of cutting force are presented with the corresponding standard deviations as the error bars.

As shown in Figure 4.1, cutting force decreased for marble and basalt as tool rotation speed increased. The cutting force in RUM mainly depends on the interaction force between diamond abrasives on the tool end surface and the workpiece material [22]. This interaction force increases as penetration depth of diamond abrasives increases [22]. When tool rotation speed increases, this penetration depth tends to decrease when the feedrate is fixed, hence reducing the interaction force [22]. This leads to a reduction in the cutting force [22]. Whereas cutting force increased for

travertine as tool rotation speed increased. This outcome for travertine was consistent with previous reports on RUM of other materials including carbon fiber-reinforced plastic composites, sapphire, and dental ceramics [22, 23, 25]. For travertine, the increased cutting force associated with the increase in tool rotation speed from 1500 to 2500 rpm was similar to that of RUM of ceramic matrix composites [18]. As shown in Figure 4.2, travertine was the most porous material; it contained extensive impurities as proven by the dark spots that indicate a different type of rock.

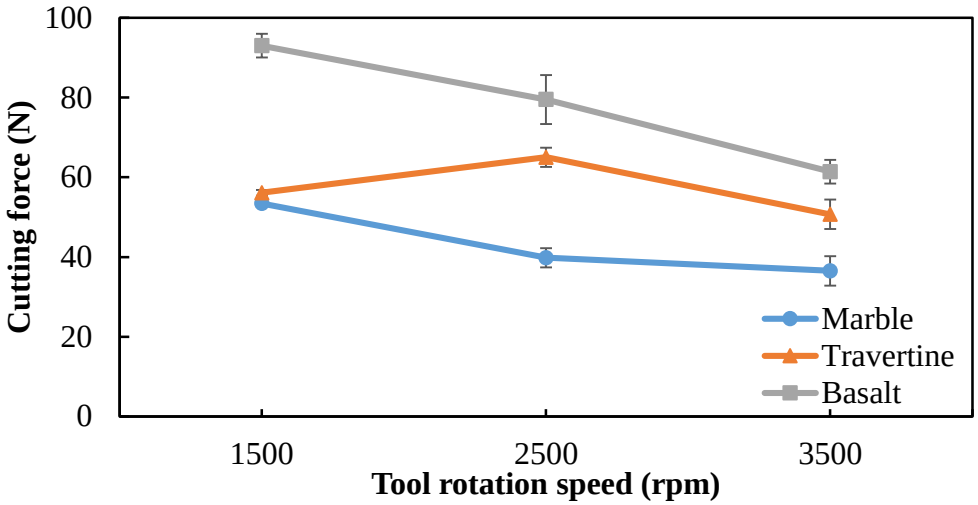

Figure 4.1 Effects of tool rotation speed on cutting force

(Feedrate = 0.3 mm/s, Ultrasonic power = 40%, Abrasive size = 0.12 mm, Abrasive concentration = 100, and drill bit diameters (Do, Di) = (12, 10) mm)

When feedrate increases the penetration depth of diamond abrasives increases and as a result, interaction force increases. This results in an increase in cutting force. Figure 4.3 illustrates that cutting force increased as per a close-to-linear trend within the feed rate ranging from 0.1 to 0.5 mm/s. This trend was consistent with previous RUM studies of drilling carbon fiber-reinforced plastics, ceramic matrix composites, and ceramics [18, 19, 22].

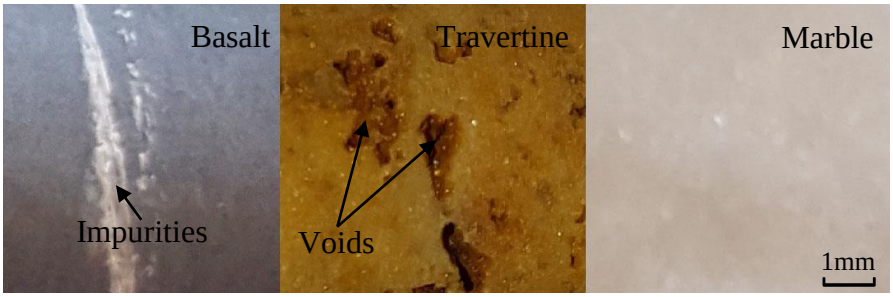

Figure 4.2 Rock surfaces of machined rods extracted by RUM

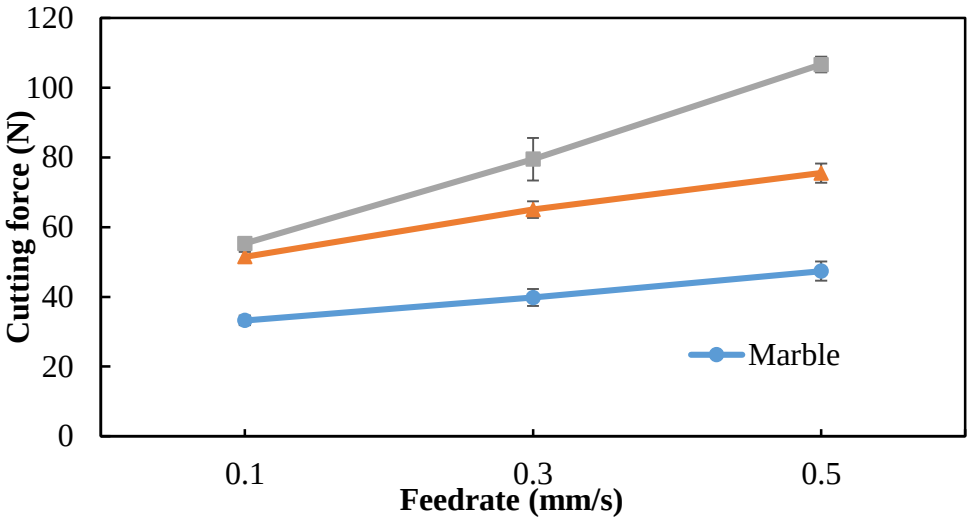

Figure 4.3 Effects of feedrate on cutting force

(Tool rotation speed = 2500 rpm, Ultrasonic power = 40%, Abrasive size = 0.12 mm, Abrasive concentration = 100, and drill bit diameters (D_o, D_i) = (12, 10) mm)

Ultrasonic vibration amplitude increases as ultrasonic power increases, resulting in an increase in the penetration depth of diamond abrasives into the workpiece material, hence increasing the interaction force. This also results in an increase in cutting force. But as shown in Figure 4.4, the increasing ultrasonic power caused cutting force to decrease only for marble. For travertine, cutting force increased with an increase in ultrasonic power and basalt showed a peak cutting force at 40% ultrasonic power. Cong et al. reported that when ultrasonic power was set at

20% - 40%, the peak cutting force was obtained at 30% ultrasonic power for RUM of stainless steel, which is similar to the behavior of basalt [26].

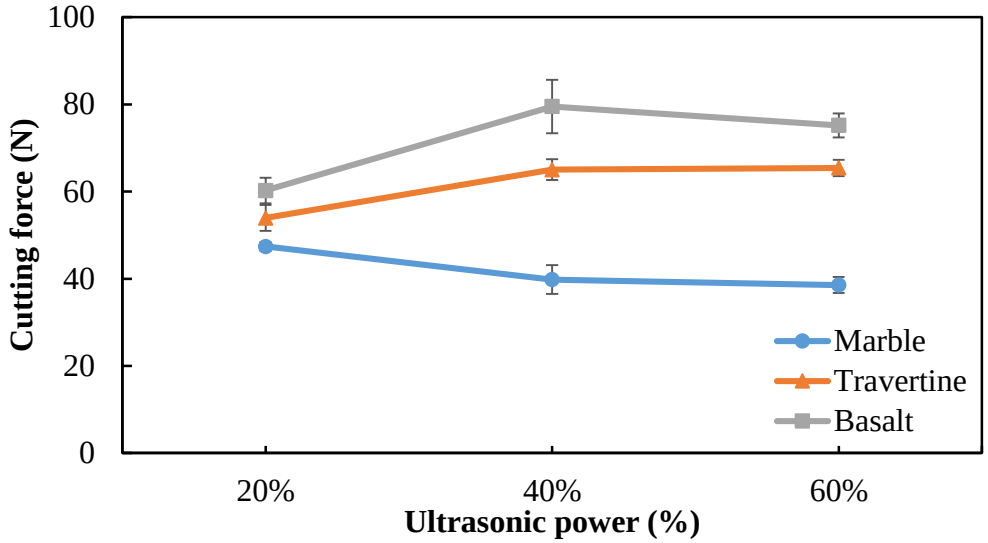

Figure 4.4 Effects of ultrasonic power on cutting force

(Tool rotation speed = 2500 rpm, Feedrate = 0.3 mm/s, Abrasive size = 0.12 mm, Abrasive concentration = 100, and drill bit diameters (D_o, D_i) = (12, 10) mm)

When abrasive size increases penetration depth of diamond abrasives decrease if the ultrasonic power is a constant, hence reducing the interaction force. This results in a reduction in cutting force. Figure 4.5 shows that the cutting force of travertine decreased as abrasive size increased. Basalt and marble obtained the minimum cutting force at an abrasive size of 0.12 mm. Cong et al. reported that cutting force decreased as abrasive size increased, which was consistent with the reported trend for travertine in this study [27].

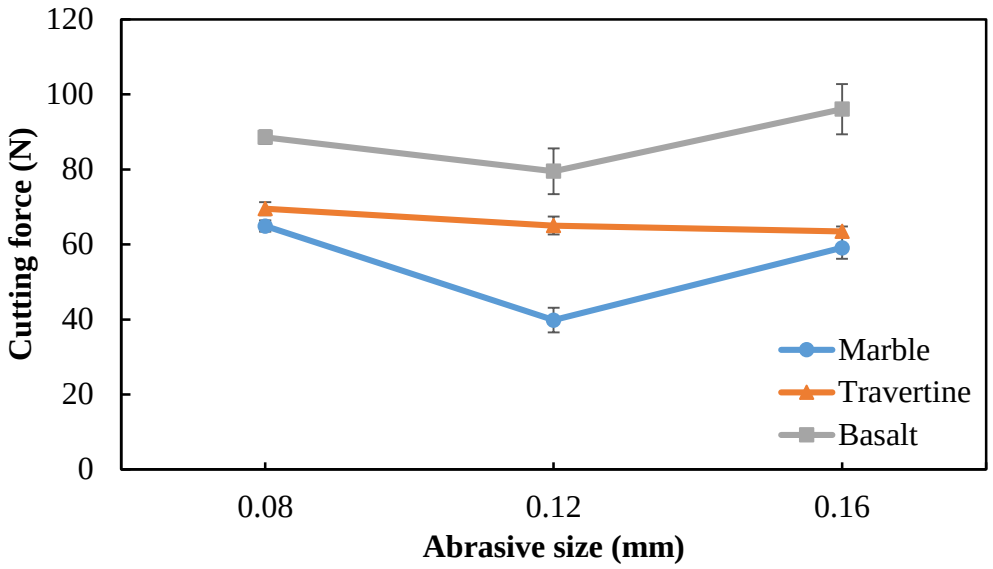

Figure 4.5 Effects of abrasive size on cutting force

(Tool rotation speed = 2500 rpm, Feedrate = 0.3 mm/s, Ultrasonic power = 40%, Abrasive concentration = 100, and drill bit diameters (D_o, D_i) = (12, 10) mm)

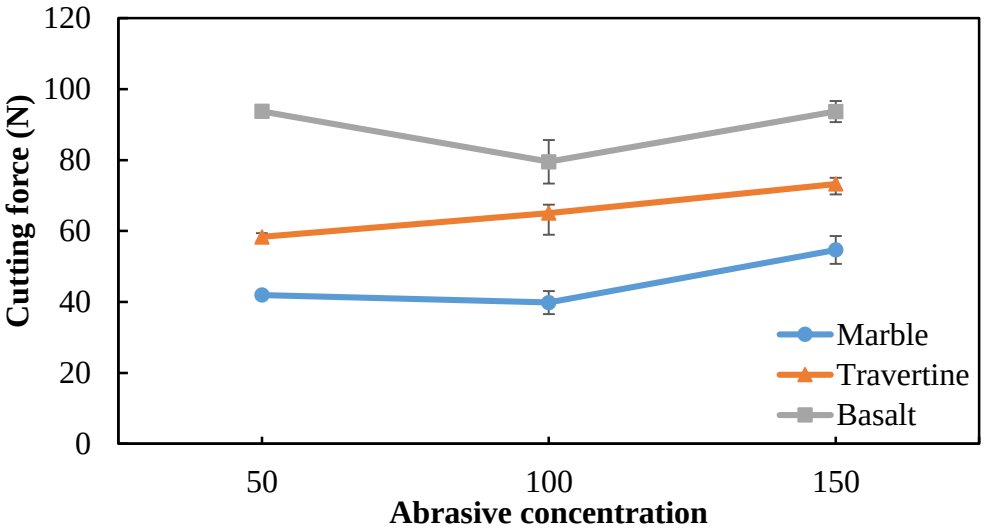

Figure 4.6 Effects of abrasive concentration on cutting force

(Tool rotation speed = 2500 rpm, Feedrate = 0.3 mm/s, Ultrasonic power = 40%, Abrasive size = 0.12 mm, Abrasive concentration = 100, and drill bit diameters (D_o, D_i) = (12, 10) mm)

As shown in Figure 4.6, cutting force had a positive correlation with abrasive concentration only for travertine. Basalt and marble showed the minimum cutting force at an abrasive concentration of 100.

Cutting force increased as drill bit diameter increased for all three rock types as shown in Figure 4.7. The increment of cutting force from drill bit diameters (9, 7) mm to drill bit diameters (12, 10) mm was much lower than the increment of cutting force from drill bit diameters (12, 10) mm to drill bit diameters (15, 13) mm, despite the difference between the effective cutting areas of the two drill bits being constant.

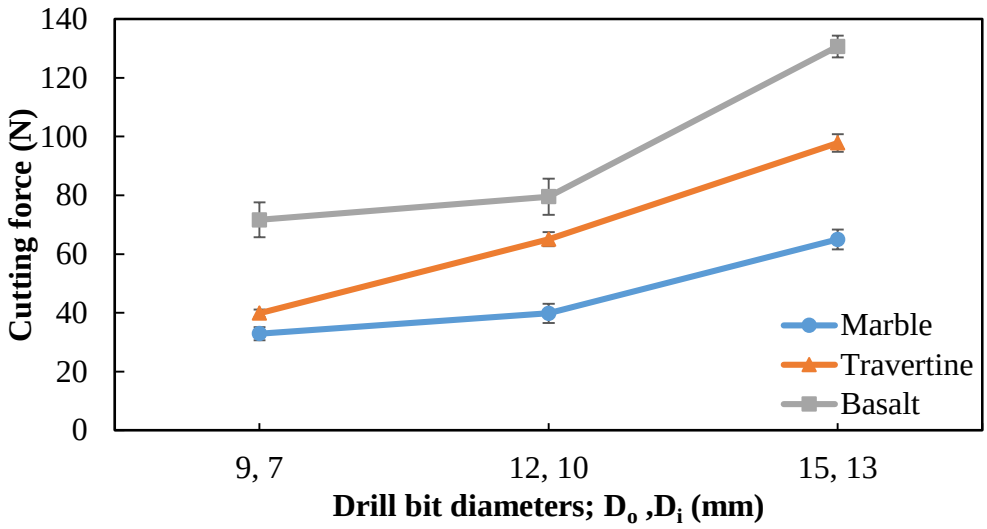

Figure 4.7 Effects of drill bit diameters on cutting force

(Tool rotation speed = 2500 rpm, Feedrate = 0.3 mm/s, Ultrasonic power = 40%, Abrasive size = 0.12 mm, and Abrasive concentration = 100)

The highest cutting force was recorded when drilling basalt, which was the hardest rock in the study. RUM can drill holes of 15 mm or smaller in diameter in hard rocks with a cutting force of less than 150 N and a feed rate of 0.5 mm/s. One study on the optimization of rotary-percussion drill for lunar exploration reported that a minimum of 399 N cutting force was obtained when drilling a 33 mm diameter hole in marble [28]. They obtained a penetration rate of 0.17 mm/s at a

percussion frequency of 20 Hz [28]. RUM of a 15 mm diameter hole on marble could reach a feed rate of 0.5 mm/s with a cutting force of 64.99 N. Therefore, RUM could offer improved performance over rotary-percussion drilling when drilling rocks such as marble.

4.1.3.2 Effects on surface roughness

Figures 4.8 – 4.13 show the effects of tool rotation speed, feed rate, ultrasonic power, abrasive size, abrasive concentration, and drill bit diameters on surface roughness. Consistent surface roughness values were impractical to obtain for travertine due to its high porosity (Figure 4.2). Thus, surface roughness measurements of travertine were not presented in this study as the measured local surface roughness might misrepresent the surface roughness of the machined surface of the travertine workpiece.

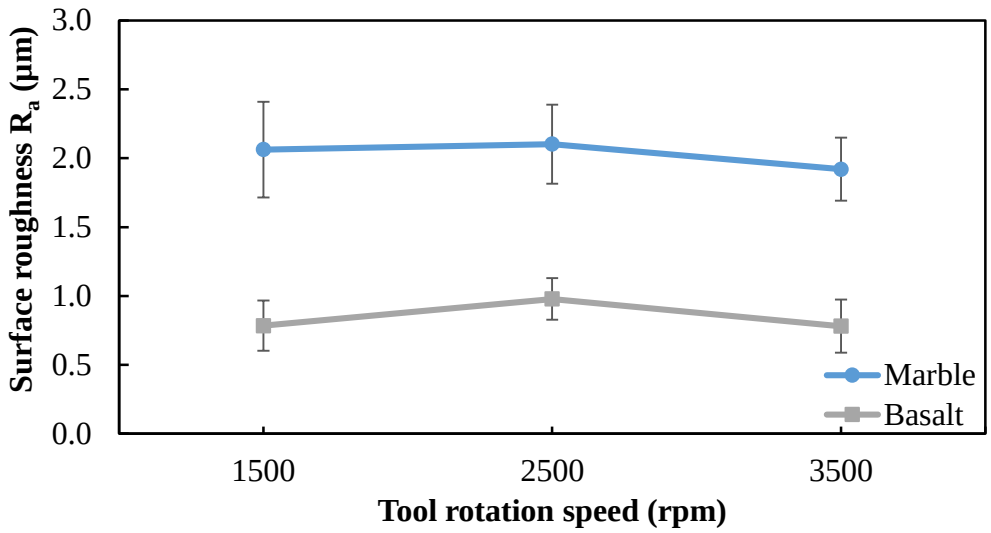

Figure 4.8 Effects of tool rotation speed on surface roughness

(Feedrate = 0.3 mm/s, Ultrasonic power = 40%, Abrasive size = 0.12 mm, Abrasive concentration = 100, and drill bit diameters (Do, Di) = (12, 10) mm)

As shown in Figure 4.8, the highest surface roughness was reported at a tool rotation speed of 2500 rpm for basalt and marble. The surface roughness ranges of basalt and marble were 0.18 µm and 0.20 µm, respectively.

As shown in Figure 4.10, ultrasonic power had an insignificant effect on the surface roughness of basalt. The three measurements of surface roughness at each level of ultrasonic power were all within the range of 0.95 and 0.99 µm. Marble showed a direct, positive correlation between surface roughness and ultrasonic power, but the range was only 0.31 µm. Jiao et al. reported that ultrasonic power did not significantly affect surface roughness in RUM of ceramics, as confirmed by the obtained results for basalt in this study [19].

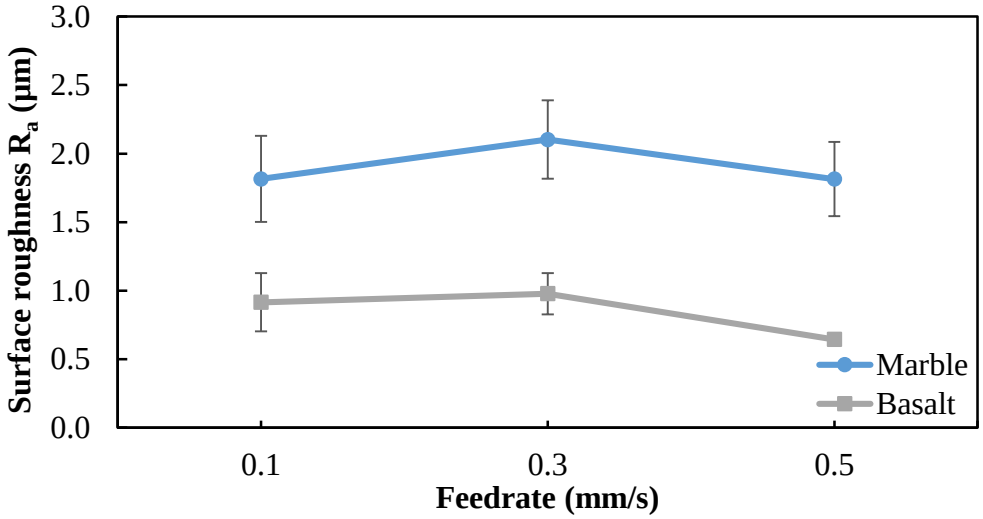

Figure 4.9 Effects of feedrate on surface roughness

(Tool rotation speed = 2500 rpm, Ultrasonic power = 40%, Abrasive size = 0.12 mm, Abrasive concentration = 100, and drill bit diameters (D_o, D_i) = (12, 10) mm)

As shown in Figure 4.11, the surface roughness of basalt had overlapping error bars, indicating that abrasive size had a statistically insignificant effect on the surface roughness of basalt. However, abrasive size did have a significant effect on the surface roughness of marble, with the highest surface roughness being observed when using the 0.12 mm abrasive size followed by the 0.08 mm and 0.16 mm abrasive sizes. For basalt and marble, surface roughness values were similar (only differing by 0.15 µm) when using the 0.16 mm abrasive size. According to Jiao et

al., abrasive size had a significant effect on surface roughness for RUM of ceramics, as agreed upon by the obtained results for marble in this study [19].

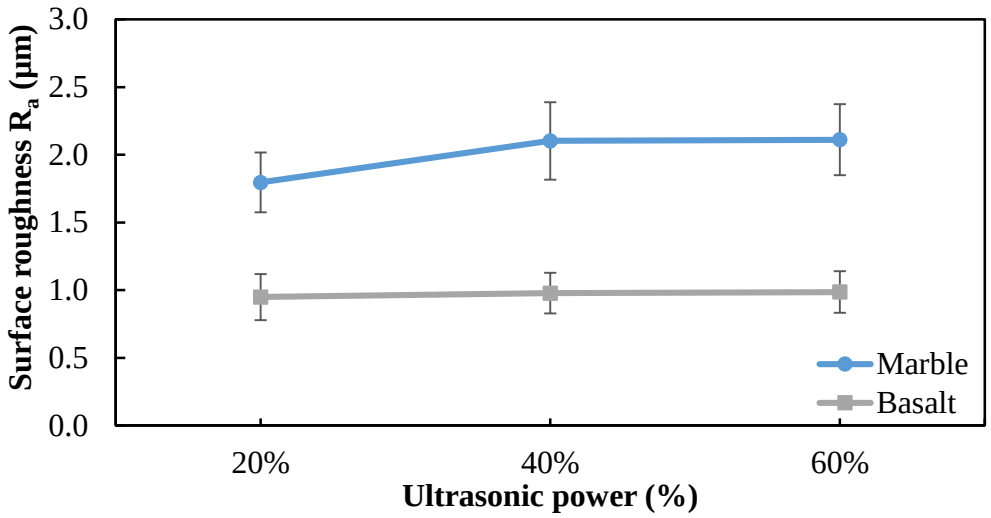

Figure 4.10 Effects of ultrasonic power on surface roughness

(Tool rotation speed = 2500 rpm, Feedrate = 0.3 mm/s, Abrasive size = 0.12 mm, Abrasive concentration = 100, and drill bit diameters (D_o, D_i) = (12, 10) mm)

As shown in Figure 4.12, abrasive concentration had more influence on the surface roughness of marble than basalt. A smoother surface finish was obtained when using the highest abrasive concentration of 150 for both rocks. Higher abrasive concentration means that a larger number of abrasive particles were involved in cutting, which produces smaller chips and finer scratches on the surface, resulting in a better surface finish.

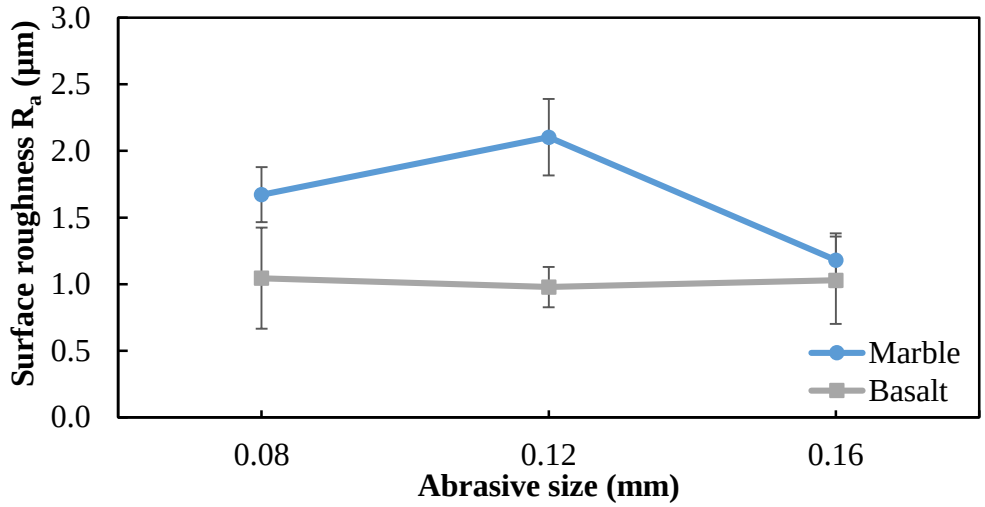

Figure 4.11 Effects of abrasive size on surface roughness

(Tool rotation speed = 2500 rpm, Feedrate = 0.3 mm/s, Ultrasonic power = 40%, Abrasive concentration = 100, and drill bit diameters (Do, Di) = (12, 10) mm)

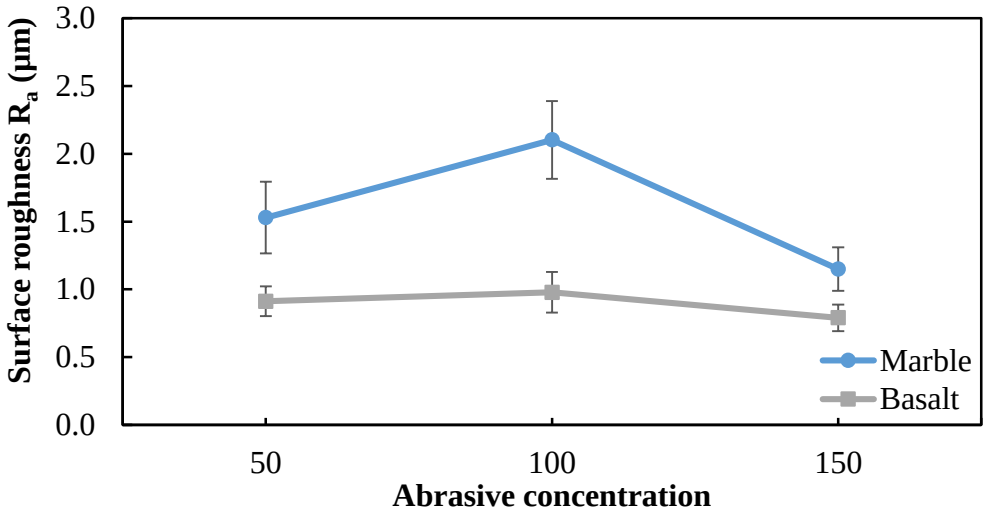

Figure 4.12 Effects of abrasive concentration on surface roughness

(Tool rotation speed = 2500 rpm, Feedrate = 0.3 mm/s, Ultrasonic power = 40%, Abrasive size = 0.12 mm, and drill bit diameters (Do, Di) = (12, 10) mm)

As shown in Figure 4.13, drill bit diameters significantly affected surface roughness, especially for marble. The smallest drill bit resulted in the best surface finish for both rock types. However, drill bit diameters had a minor effect on the surface roughness for basalt. For both rock

types, the highest surface roughness was reported for the drill bit with the outer and inner diameters of 12 mm and 10 mm, respectively.

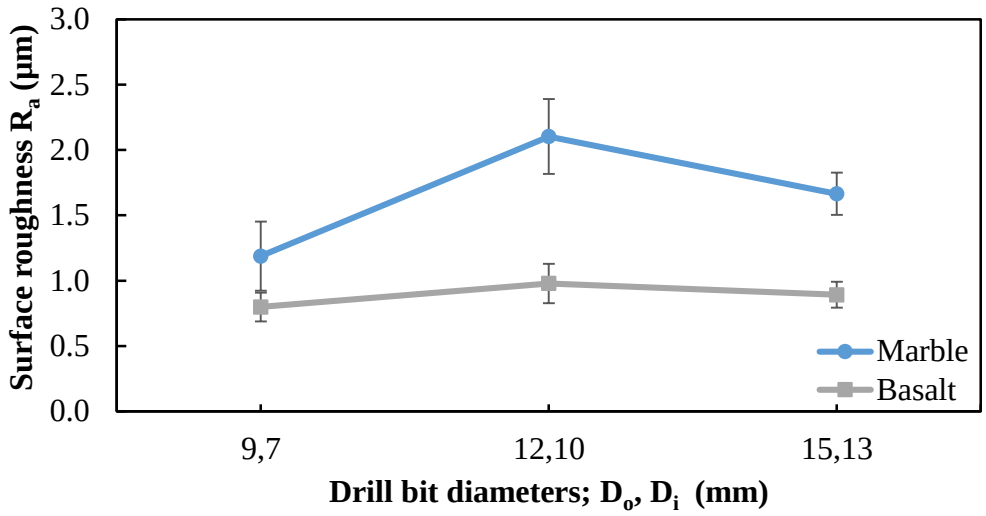

Figure 4.13 Effects of drill bit diameters on surface roughness

(Tool rotation speed = 2500 rpm, Feedrate = 0.3 mm/s, Ultrasonic power = 40%, Abrasive size = 0.12 mm, and Abrasive concentration = 100)

4.1.4 Conclusions

This paper presents an experimental study on rotary ultrasonic machining (RUM) of three types of rocks: basalt, travertine, and marble. The following conclusions are drawn:

1. This investigation demonstrated that RUM is capable of drilling hard rocks with a feed rate comparable to that of existing drilling procedures.
2. The effects of feed rate and drill bit diameter on cutting force were significant. A higher feed rate and larger drill bit diameter led to a higher cutting force.
3. For basalt and marble, an abrasive concentration of 100 gave the lowest cutting force and cutting force decreased as tool rotation speed increased.
4. Tool rotation speed, feed rate, and ultrasonic power had an insignificant effect on surface roughness.

4.2 Rotary ultrasonic machining of basalt rock using compressed air as coolant: a study on edge chipping and surface roughness

Paper title:

Rotary ultrasonic machining of basalt rock using compressed air as coolant: a study on edge chipping and surface roughness

Published in:

Proceedings of the ASME 2019 International Manufacturing Science & Engineering Conference (MSEC-2019), June 10-14, 2019, Erie, PA, USA

Authors' names:

Fernando, P.[1], Zhang, M.[1], Pei, Z.J.[2], Owens, A.[1]

Authors' affiliations:

1. Department of Industrial and Manufacturing Systems Engineering, Kansas State University, Manhattan, KS 66506, USA
2. Department of Industrial and Systems Engineering, Texas A & M University, College Station, TX 77843 USA

4.2.1 Introduction

Rock drilling is a challenging practice due to several reasons: an infinite variability of rock properties, the relatively high hardness and abrasiveness of rocks, large friction between the rock and tool, severe tool wear and damage, etc. [6, 29]. Most of the recent investigations focused on finding superior materials and designs for tools to avoid tool damage and reduce wear to improve drilling efficiency [30-34]. Throughout the history of rock drilling, research on developing novel and cost-effective rock drilling techniques has lagged behind.

There are three main rock drilling techniques: rotary/percussive drilling for very hard rock (basalt, quartz, etc.), rotary/crushing drilling for rocks of average hardness (travertine, sandstone, etc.), and cutting for soft rock (talc, marble, etc.) [30]. In mining, most of the energy is consumed to crack the rock/coal to produce large fragments; therefore, the cutting operation can be closely related to the edge chipping [35]. However, an in-situ investigation to control edge chipping conditions in mining is a difficult and costly task [35]. Hence, laboratory testing is the feasible way to investigate edge chipping, since it is more cost and time effective, and can also obtain more accurate data compared to in-situ investigations [35].

Rock drilling studies have been conducted using various types of drilling techniques. For example, there are studies that have used impregnated diamond bits in rock drilling [36-38], Huang et al. investigated the mechanics of the diamond core drilling of rocks by performing a series of laboratory experiments [39], and a core drill bit was designed by Clydesdale et al. that allows the penetration rate to increase while also reduced the fluid invasion [31].

Rotary ultrasonic machining (RUM) is able to offer advantages over conventional hole-making processes because of its combination of ultrasonic machining and grinding from its core drill with metal-bonded abrasives, which has been a successful hole-making process for brittle

materials such as ceramics, glass, etc. [19, 25, 26, 40-43]. RUM shows many advantages over conventional hole-making processes: RUM is capable of drilling deeper holes with a lower cutting force, better surface quality, and higher hole accuracy [19]. Compared to conventional grinding, RUM is more efficient due to its increased material removal rate (6-10 times faster) and lower cutting force, the latter of which increases tool life and lowers the machining temperature [16, 17, 44]. A schematic illustration of rotary ultrasonic machining is shown in Figure 1. In RUM, the cutting tool is capable of rotating and vibrating along the cutting tool axis simultaneously. RUM has the ability to use fluid coolants or compressed/cold air as coolant. Since RUM uses a core cutting tool, coolant is supplied through the cutting tool to flush away the swarf from the cutting zone, keeping the cutting tool cool and also preventing the cutting tool from jamming.

Dry machining, which eliminates the use of cutting fluids, has been widely adopted because it is safe and environmentally benign. Sixteen to twenty percent of the manufacturing cost is associated with coolants and lubricants used for machining; therefore, eliminating or reducing cutting fluid can lower the cost of machining, which is a significant incentive for the manufacturing industry [45]. Besides the cost reduction, dry machining provides several other benefits including less pollution and health issues, reduction in cleaning, and hassle-free disposal of cutting chips due to the lack of residue on them [45, 46]. However, in dry machining, lubrication is impossible with the absence of fluidic coolant, hence friction and adhesion increase at the cutting zone [45]. In turn, cutting force and temperature increase, causing an increase in tool wear, which reduces the tool life [45, 46]. In addition, gaseous coolants are impossible to circulate in the coolant system and cannot be reused because of vaporization [47, 48].

Many investigations on dry drilling have been reported in the literature. Choi et al. did a comparison of the cooling effects between compressed cold air and coolant in grinding Cr-Mo

steel (SCM4 and SCM21) with a CBN wheel [24]. They found that compressed cold air was able to minimize thermal defects on the ground surface layer and that both had a similar tendency on surface roughness of the ground surface [46]. Su et al. reported an investigation on the cutting of difficult-to-cut materials by using refrigerated cooling air and found that it was capable of providing better machinability for difficult-to-cut materials such as Inconel 718 alloy and AISI D2 tool steel [49].

In addition, one of the present aims of extraterrestrial exploration missions is to perform in-situ geological investigations and to send subsurface scientific samples to the earth for further examination [50]. As an example, the mission to Mars has a strong interest in obtaining subsurface samples to examine thoroughly. The best method of subsurface sample extracting is mechanical core drilling without using a water-based liquid coolant [50]. Since Mars' atmospheric pressure is 1% of the earth's atmospheric pressure, water evaporates very fast. Dry machining can be considered as the best approach to eliminate the water-based liquid coolant in extraterrestrial exploration missions.

In general, the reduction of edge chipping and surface roughness of machined components ensures the geometric accuracy and long lifespan of the components [9, 20]. Ng et al. reported three types of edge chipping in ceramic milling: edge chipping at the entrance, interior, and exit of the machining [20]. The main reasons for the initiation and propagation of the edge chipping are the microstructure of the material and stress distribution during machining [20]. Cao's finite element analysis revealed the key factors on exit edge chipping in the milling of dental ceramics as the size, length, and orientation of the pre-existing microcrack and the location of the applied force [9]. Li et al. studied edge chipping in rotary ultrasonic machining of ceramics to investigate the effects of cutting depth, support length, and retightening load on exit edge chipping and the

findings of the study reported a reduction in exit edge chipping by increasing the support length [24]. Fernando et al. investigated on intermittent and continuous rotary ultrasonic machining of K9 glass and found that the exit edge chipping increased as cutting force increased [22].

Surface roughness of a drilled hole depends on the material, tool geometry, chip formation, process parameters, and vibration of the machining system [51]. The surface roughness produced in RUM mainly depends on the machining marks created by the abrasive particles embedded to the cutting tool. Magnitude of feedrate, tool rotation speed, and ultrasonic power, abrasive properties (abrasive concentration, size, and type) are the other factors that affect the surface roughness in RUM.

This study, for the first time, reports a study on edge chipping and surface roughness in RUM of basalt rock using cold compressed air as coolant. The effects of three input variables (tool rotation speed, feedrate, and ultrasonic power) on cutting force, torque, edge chipping, and surface roughness were studied.

4.2.2 Experimental set-up, conditions, and measurement procedures

4.2.2.1 Workpiece properties

The material of the workpiece was basalt rock, which is an igneous rock. The dimensions of the workpiece were 40 mm × 100 mm × 9 mm, and its properties are listed in Table 4.5.

Table 4.5 Properties of basalt rock [20]

Property	Unit	Basalt
Density	$g \cdot cm^{-3}$	2.9 - 3.1
Moh's hardness	-	6
Compressive strength	$N \cdot mm^{-2}$	37.5
Porosity	%	1 - 10

4.2.2.2 Experimental setup

The experiments were carried out on a rotary ultrasonic machine (Series 10, Sonic-Mill, Albuquerque, New Mexico, USA). As illustrated in Figure 4.14, the main aspects of the experimental setup are an ultrasonic spindle system, a data acquisition system, and a cold air cooling system. Ultrasonic spindle system has four major components: an ultrasonic spindle, a power supply, an electric motor, and a control panel. The power supply generates a high frequency (20 kHz) electrical output from a low frequency (60 Hz) 110 V electric input. That high frequency electric signal is converted into low-amplitude mechanical vibrations by the piezoelectric transducer in the ultrasonic spindle. Then the acoustic horn amplifies the low-amplitude mechanical vibrations before transmitting to them to the cutting tool. The amplitude of the vibration can be adjusted by varying the output power level (%) of the power supply. Above the spindle is an electric motor that provides the rotational motion to the spindle. The cold air cooling system mainly consists of an air compressor, oil and water filters, and a vortex tube. Cold air is generated in a vortex tube, which has the capability to separate the compressed air stream into two separate streams: one stream of hot air and one stream of cold air. The cold air outlet of the vortex tube is fixed onto the spindle to blow out cold air (with a temperature of 5 ^{o}C and a pressure of 50 psi) through the cutting tool. The data acquisition system contains 5 parts that combine to allow cutting force and torque data to be collected: a dynamometer (9272, Kiestler Inc., Winterthur, Switzerland), a charge amplifier (5070, Kiestler Inc., Winterthur, Switzerland), an analog to digital converter, a data acquisition card (PCIM-DAS 1602/16, Measurement Computing Corporation, Norton, MA, USA), and a computer with software (2815A, Kiestler Inc., Winterthur, Switzerland).

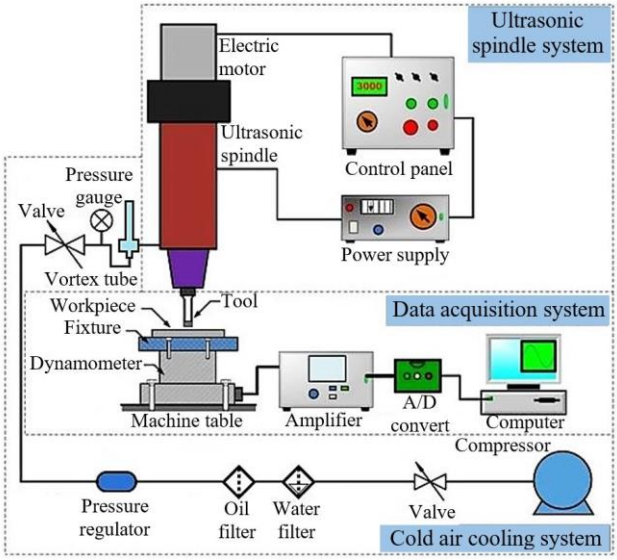

Figure 4.14 Experimental setup

4.2.2.3 Experimental conditions

The three input variables (tool rotation speed, feedrate, and ultrasonic power) are studied at five levels. The tool variables (inner and outer tool diameters, abrasive size, and abrasive concentration) were 10 mm, 12 mm, 0.106 - 0.120 mm, and 100, respectively. Abrasive size specifies the range of diameters of the abrasive particles bonded to the tool and an abrasive concentration of 100 is defined as the weight of diamond per cm3 being 4.4 carat. The experimental conditions are listed in Table 4.6. An ultrasonic power of 100% is equivalent to 900 W. Three replicates were carried out for each experimental condition.

Table 4.6 Experiment conditions

Test condition	Tool rotation speed (rpm)	Feedrate (mm/s)	Ultrasonic power (%)
1	2000	0.05	40
2	4000	0.05	40
3	4000	0.05	60
4	6000	0.05	40
5	4000	0.05	20
6	3000	0.05	40
7	4000	0.05	30
8	5000	0.05	40
9	4000	0.05	50
10	4000	0.07	40
11	4000	0.01	40
12	4000	0.09	40
13	4000	0.03	40

4.2.2.4 Measurement procedures

A dynamometer allowed cutting force and torque data to be collected. A charge amplifier received the signal from the dynamometer, amplifying it and transmitting it to the analog-to-digital converter to be converted into a numerical signal. Dynoware software was used to collect cutting force and torque data.

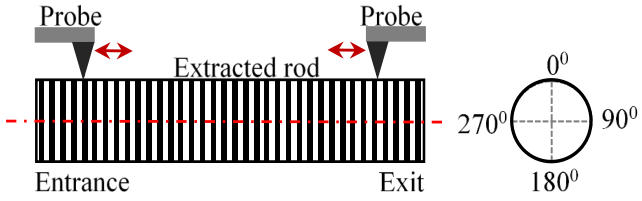

Figure 4.15 Measurement procedure of surface roughness

A surface profilometer (SJ-400, Mitutoyo Corporation, Kanagawa, Japan) was used to measure surface roughness on the cylindrical surface of the extracted rod after each drilling test. The sampling range was 4 mm and the average surface roughness value (Ra) was used to determine the surface quality of the machined surface. Surface roughness measurements were taken at both

the entrance and exit locations along the axial direction of the rod. As shown in Figure 4.15, four measurements were taken at each quadrant, and eight Ra values were obtained for each test. The means and standard deviations of these values are reported in this study.

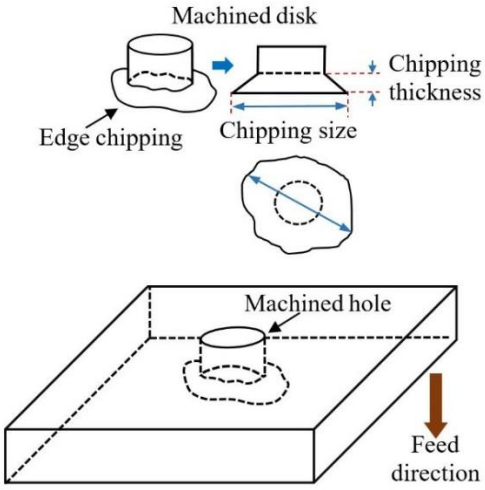

Figure 4.16 Illustration of edge chipping

RUM of brittle materials has a tendency for the machined rod to break through the workpiece before the tool has reached the end surface of the workpiece. This phenomenon has an impact on forming edge chipping at the exit of the hole, as shown in Figure 4.16. A microscope (BX51M, Olympus Inc., Tokyo, Japan) was utilized to inspect the edge chipping at the exit of the machined hole and the extracted rod. After each test, the chipping thickness and the chipping size was measured with a caliper (IP-65, Mitutoyo Corporation, Kanagawa, Japan).

4.2.3 Results and discussions

This section reports and discusses the main effects of input variables (ultrasonic power, tool rotation speed, and feedrate) on output variables (cutting force, surface roughness, edge chipping thickness, and edge chipping diameter). Figure 4.17 presents images of machined holes

and rods of basalt machined by RUM. It shows that RUM has the capability to drill basalt without severe damage to the entrance and exit surfaces.

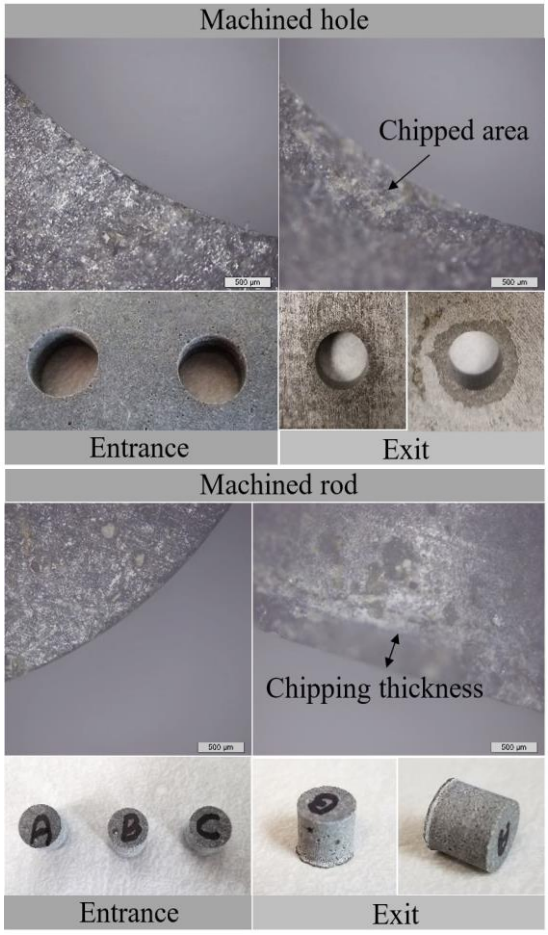

Figure 4.17 Images of machined hole and rod at the entrance and exit

4.2.3.1 Effects on cutting force

Cutting force is one of the main output variables in drilling because it is the output variable that has the largest effect on other output variables, such as tool wear, cutting temperature, edge chipping, etc. [18, 52]. The maximum and average cutting forces of each test were reported in this study. Table 4.7 presents experimental results on cutting force, surface roughness, edge chipping thickness, and edge chipping diameter.

Table 4.7 Experimental results

Test condition	Maximum cutting force (N)	Average cutting force (N)	Edge chipping thickness (mm)	Edge chipping diameter (mm)
1	256.11	112.92	1.28	21.48
2	304.05	128.19	0.75	18.14
3	355.83	130.41	1.98	22.77
4	264.07	59.61	1.04	19.12
5	270.19	133.30	1.36	20.91
6	329.61	115.01	1.17	19.17
7	327.33	141.09	1.58	21.60
8	264.44	57.98	0.88	18.45
9	430.03	151.08	1.43	23.75
10	448.66	99.71	1.25	23.19
11	142.09	53.44	0.53	14.72
12	450.83	104.17	1.31	21.90
13	319.88	115.19	1.25	21.21

Figures 4.18-4.20 show the effects of tool rotation speed, feedrate, and ultrasonic power on cutting force. The mean values of maximum cutting force and average cutting force of the experimental runs under each test condition are presented. Error bars are represented corresponding standard deviations. As shown in Figure 4.18, the maximum cutting force decreased as tool rotation speed increased from 3000 rpm to 6000 rpm and average cutting force decreased as tool rotation speed increased from 4000 rpm to 6000 rpm. Cutting force in RUM is determined by the interaction force between the abrasive particles on the tool end surface and the workpiece material [53]. When the penetration depth of the diamond abrasives increases the interaction force increases [53]. This penetration depth has a tendency to decrease as tool rotation speed increases for a fixed feedrate, which results in the reduction of the interaction force. This leads to an overall decrease in the cutting force as tool rotation speed increases, although the maximum cutting force increased as the tool rotation speed increased from 2000 rpm to 3000 rpm and average cutting

force increased as the tool rotation speed increased from 2000 rpm to 4000 rpm. This outcome is consistent with previous studies on RUM of travertine, sapphire and dental ceramics [53-55].

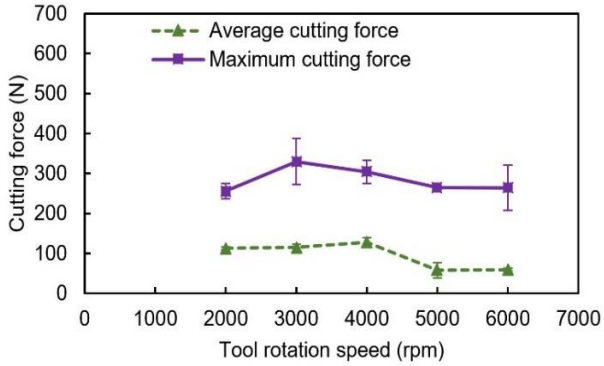

Figure 4.18 Effects of tool rotation speed on cutting force

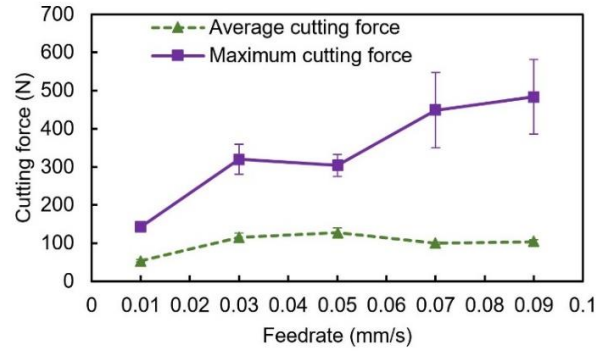

Figure 4.19 Effects of feedrate on cutting force

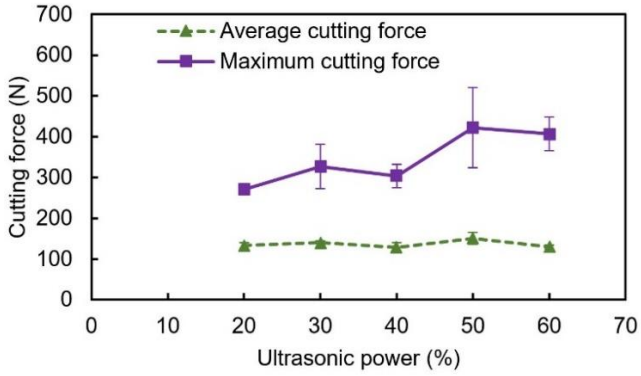

Figure 4.20 Effects of ultrasonic power on cutting force

Figure 4.19 illustrates that the maximum cutting force increased as feedrate increased, except for the feedrate at 0.05 mm/s. The penetration depth of diamond abrasives increases as

feedrate increases, which results in an increase in cutting force. This trend is consistent with the previous RUM studies of drilling carbon fiber-reinforced plastics, rocks, ceramic matrix composites, and ceramics [19, 53, 54, 56]. The average cutting force increased as feedrate increased from 0.01 mm/s to 0.05 mm/s.

Ultrasonic vibration amplitude is affected by ultrasonic power. As ultrasonic power increases, ultrasonic vibration amplitude and the penetration depth of abrasive particles into the workpiece increase, which results in an increase of cutting force. As shown in Figure 4.20, the maximum cutting force increased as ultrasonic power increased, except for 40% ultrasonic power.

4.2.3.2 Effects on torque

Figures 4.21-4.23 show the effects of tool rotation speed, feedrate, and ultrasonic power on the maximum and average torque. The three input variables have an insignificant effect on average torque. Figure 4.21 shows a decreasing trend of the maximum torque as tool rotation speed increased, except for 4000 rpm. The lowest maximum torque was obtained under the second test condition of 4000 rpm tool rotation speed, 0.05 mm/s feedrate, and 40% ultrasonic power.

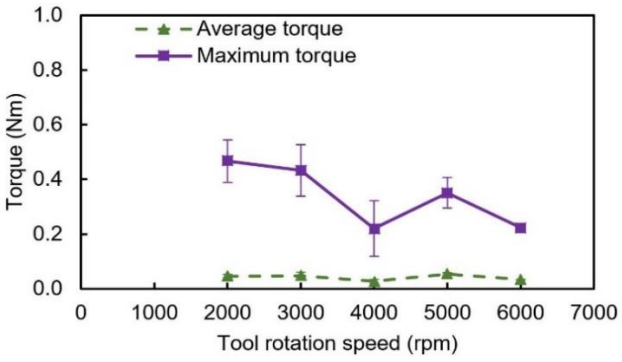

Figure 4.21 Effects of tool rotation speed on torque

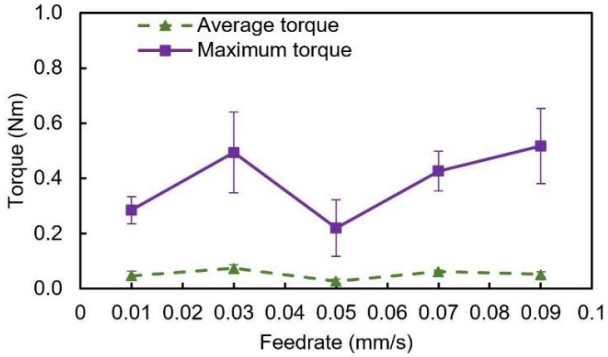

Figure 4.22 Effects of feedrate on torque

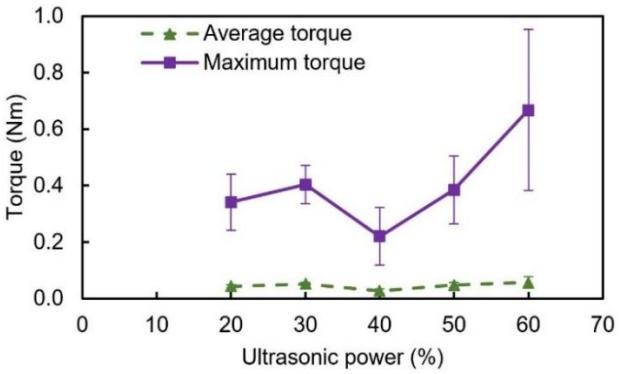

Figure 4.23 Effects of ultrasonic power on torque

4.2.3.3 Effects on surface roughness

Figures 4.24-4.26 show the effects of tool rotation speed, feedrate, and ultrasonic power on average surface roughness and surface roughness at the entrance and the exit. The highest surface roughness (Ra) is reported at the highest tool rotation speed of 6000 rpm, while the lowest surface roughness is reported at the lowest feedrate of 0.01 mm/s. Surface roughness decreased as tool rotation speed increased from 2000 rpm to 5000 rpm, and surface roughness dramatically increased at 6000 rpm. Surface roughness showed an increasing trend with increased feedrate. The minimum surface roughness was observed when 40% ultrasonic power was used.

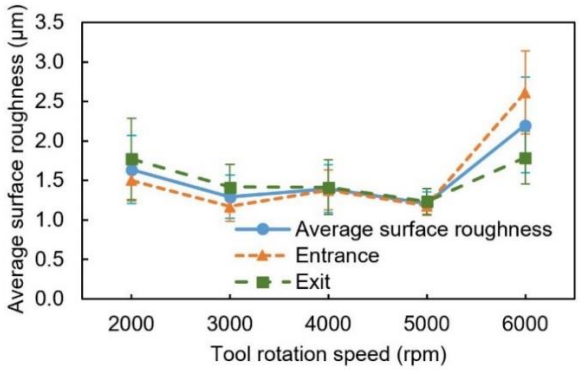

Figure 4.24 Effects of tool rotation speed on surface roughness

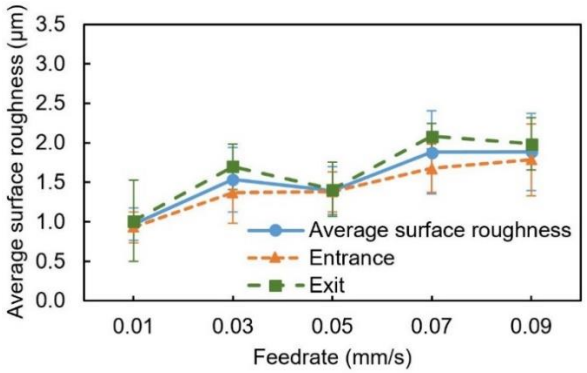

Figure 4.25 Effects of feedrate on surface roughness

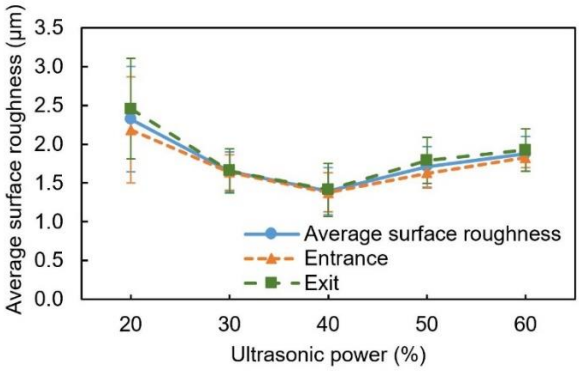

Figure 4.26 Effects of ultrasonic power on surface roughness

4.2.3.4 Effects on edge chipping

Figures 4.27-4.29 show the effects of tool rotation speed, feedrate, and ultrasonic power on the thickness and diameter of edge chipping. The lowest edge chipping thickness and diameter

were obtained by the lowest feedrate of 0.01 mm/s. The maximum thickness and diameter of the edge chipping were reported at 60% and 50% ultrasonic power, respectively. When ultrasonic power increases, the penetration depth of the abrasive particles into the workpiece also increases. This results in an increase in the edge chipping at the exit surface of the drilling.

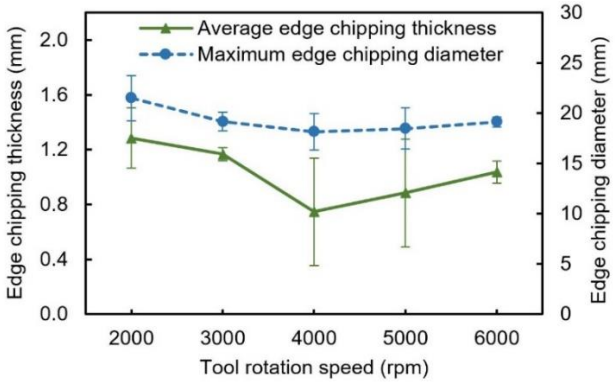

Figure 4.27 Effects of tool rotation speed on edge chipping

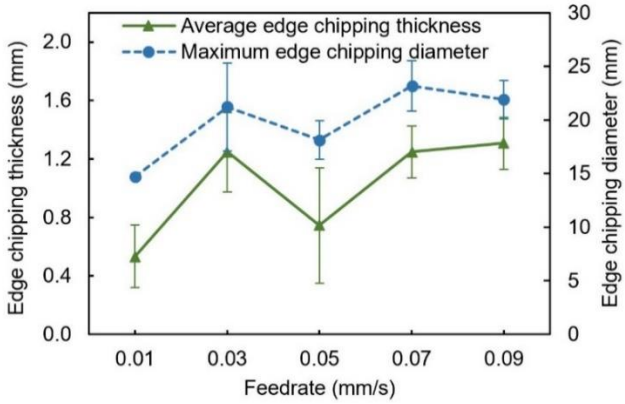

Figure 4.28 Effects of feedrate on edge chipping

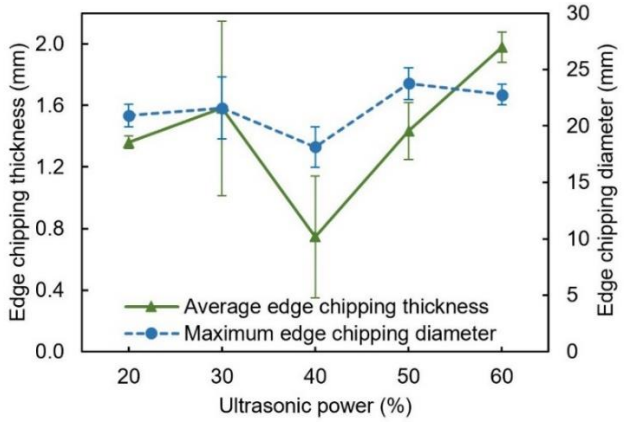

Figure 4.29 Effects of ultrasonic power on edge chipping

4.2.4 Concluding remarks

This study reports an experimental study on rotary ultrasonic machining of basalt rock using cold air as coolant. The effects of the tool rotation speed, feedrate, and ultrasonic power on cutting force, torque, surface roughness, and edge chipping were studied. The following conclusions are drawn:

1. Cutting force and torque increased as feedrate and ultrasonic power increased. As tool rotation speed increased from 2000 rpm to 6000 rpm with 0.05 mm/s feedrate and 40% ultrasonic power, cutting force firstly increased and then decreased.
2. The surface roughness (R_a) at the exit of the drilled holes had larger R_a values compared to that at the entrance and higher feedrate led to a higher surface roughness. As ultrasonic power increased from 20% to 60% with 0.05 mm/s feedrate and 4000 rpm tool rotation speed, surface roughness firstly decreased and then increased.
3. The increase of the tool rotation speed had a tendency to decrease the average edge chipping thickness and maximum edge chipping diameter.

The work reported in this paper was an experimental study of RUM of a heterogeneous material, basalt rock. The obtained results on the effects of the input variables of cutting force, torque, surface roughness, and edge chipping are valuable to provide a foundation for further studies on the RUM of rock drilling.

4.3 Mechanistic cutting force model for rotary ultrasonic machining of rocks

Paper title:

Mechanistic cutting force model for rotary ultrasonic machining of rocks

Published in:

Submitted to The International Journal of Advanced Manufacturing Technology.

Authors' names:

Fernando, P.[1], Zhang, M.[1], Pei, Z.J.[2],

Authors' affiliations:

3. Department of Industrial and Manufacturing Systems Engineering, Kansas State University, Manhattan, KS 66506, USA
4. Department of Industrial and Systems Engineering, Texas A & M University, College Station, TX 77843 USA

Nomenclature

Symbol	Description	Unit
A	Ultrasonic vibration amplitude	m
A_0	Area of the tool end face	m^2
C_a	Abrasive concentration	-
C_h	Lateral crack depth	m
C_L	Lateral crack length	m
d_a^1 and d_a^2	Abrasive sizes related to the pore sizes of sieves	m
d_c	critical depth of cut for brittle-to-ductile transition	m
d_o and d_i	Outer and inner diameters of the tool	m
E	Elastic modulus of the rock	
F	Cutting force measured during RUM of rock	N
F_i	Maximum impact force applied by one abrasive particle	N
F_m	Maximum impact force	N
f	Ultrasonic vibration frequency	Hz
f_r	Feedrate	m/s
h_{max}	Maximum protrusion height	m
H_v	Vickers hardness of the rock	Pa
k	Proportionality parameter	-
K_{IC}	Fracture toughness of the rock	$Pa \cdot m^{1/2}$
K_{Id}	Dynamic fracture toughness	$Pa \cdot m^{1/2}$
L	Effective cutting distance	m
L_b	Brittle fracture mode cutting distance	m
L_d	Ductile mode cutting distance	m
MRR_a	Material removal rate of one abrasive particle	m^3/s
MRR_c	Material removal rate of the tool	m^3/s
N	Number of abrasive particles on the tool end face	-
N_a	Number of effective abrasive particles on the tool end face	-
R_d	Distance of an abrasive particle to the center of the tool	m
S	Tool rotation speed	rpm
S_1 and S_2	Standard mesh numbers	
S_a	Abrasive size	mm
t	Time	s

V	Actual volume of material removed by one abrasive particle during one ultrasonic vibration cycle	m^3
V_b	Volume of brittle mode material removal	m^3
V_d	Volume of ductile mode material removal	m^3
$V_{\Delta t}$	Volume of material removed by one abrasive particle during effective cutting time	m^3
ν	Poisson's ratio of the rock	-
z_0	Penetration depth	m
α	Geometric factor of the shape of the abrasive particle	-
β	Semi-angle between two opposite edges of an abrasive particle	Degree
β_0	Half-top angle of an abrasive particle	Degree
λ_0	Integrative factor	-
μ	Mean value of abrasive protrusion height	
ρ	Density of the abrasive material	g/mm^3
σ	Standard deviation of protrusion heights	

4.3.1 Introduction

Rock drilling has been performed using a number of techniques including rotary drilling, rotary-percussive drilling, and rotary-crushing drilling [30]. Recently, rotary ultrasonic machining (RUM) has been reported as another feasible technique to rock drilling [51, 57]. Studies showed that introducing ultrasonic vibration along the feedrate direction of a diamond core drill reduced cutting force and enhanced material removal rate compared to conventional core drilling [51, 57]. RUM, shown in Figure 1.1, is a hybrid machining process of grinding and ultrasonic machining. It has been used mainly for drilling brittle materials such as glass, ceramics, potassium dihydrogen phosphate, and rocks [19, 42, 51, 55]. RUM employs a rotating tool (core drill) with metal bonded abrasives that vibrates along the feeding axis at ultrasonic frequency.

Cutting force is the predominant output variable in rotary ultrasonic machining (RUM). It dictates other output variables, such as tool wear, cutting temperature, and edge chipping [24, 58].

Cutting force prediction over a wide range of input variables is crucial for explaining experimental observations and optimizing the RUM process. There have been several cutting force models developed for predicting cutting forces in RUM of brittle, ductile, and composite materials [27, 59, 60]. Most of these models are developed for RUM systems that use constant feedrate instead of constant weight (or force) on the tool. There are also a few models developed to predict material removal rate for RUM systems that use constant weight (or force) on the tool to drive the tool into the workpiece [61-66].

Studies on cutting force modeling for rotary ultrasonic machining primarily consider input variables and mechanical properties of workpiece materials [27, 59, 60]. Numerous researchers have developed theoretical approaches to predict cutting force in RUM considering the main material removal mechanism as brittle fracture by the impact of the abrasive particles bonded to the tool [16, 67], nevertheless, the combined effects of material removal on cutting force model has not been investigated.

This study focuses on developing a cutting force model for rotary ultrasonic machining of rock considering the ductile mode removal and brittle fracture mode removal of rock under the indentation of a single abrasive particle and input variables. A proportionality parameter is used to represent the ratio between the actual and the theoretical volumes of material removed by one abrasive particle during the effective cutting time. This proportionality parameter is regarded as a constant for a particular material in the model development, and the proportionality parameter can be obtained by preliminary experiments. Then the model can be used to predict cutting force over a wide range of input variables.

This paper consists of six sections. Following this introduction section, Section 2 describes the development of cutting force model. Section 3 presents the process of obtaining the

proportionality parameter for basalt rock through preliminary experiments. In Section 4, predicted effects of input variables (feedrate, tool rotation speed, ultrasonic vibration amplitude, abrasive size, abrasive concentration, and tool size) on cutting force are presented. Intermediate variables (maximum impact force, penetration depth, and the effective cutting time) are used to assist explaining the predictions. Model verification by pilot experiments is presented in Section 5. Finally, concluding remarks are drawn in Section 6.

4.3.2 Development of mechanistic cutting force model

4.3.2.1 Approach to model development

RUM is a hybrid machining process of ultrasonic machining and grinding. It involves a large number of input variables. Several analyses start with one abrasive particle and then aggregates the effects of all active abrasive particles involved in cutting [27, 59-61, 63, 65, 66, 68]. This approach is employed in this study. The following steps are executed in the model development:

(1) Establish a relationship between tool variables and the number of effective abrasive particles on the tool end face;

(2) Establish a relationship between material properties and the critical depth of cut for brittle-to-ductile transition;

(3) Establish a relationship between cutting force and abrasive particle penetration depth;

(4) Estimate the volume of material removed by one abrasive particle during one ultrasonic vibration cycle;

(5) Develop the cutting force model by aggregating the effects of all active abrasive particles.

The input variables considered in the model development include machining variables, core drill variables, and properties of the workpiece material, as listed in Figure 4.30.

The following is a list of assumptions and simplifications that are considered in the model development:

(1) The abrasive particles are rigid regular octahedrons of the same size (Figure 4.31(a) & (b)).

(2) As shown in Figure 4.31(b), the semi-angle (β) between two opposite edges of an abrasive particle is 45°.

(3) All the effective abrasive particles on the tool end face have the same protrusion height and all of them are involved in cutting during each ultrasonic vibration cycle.

(4) The workpiece is a homogeneous material.

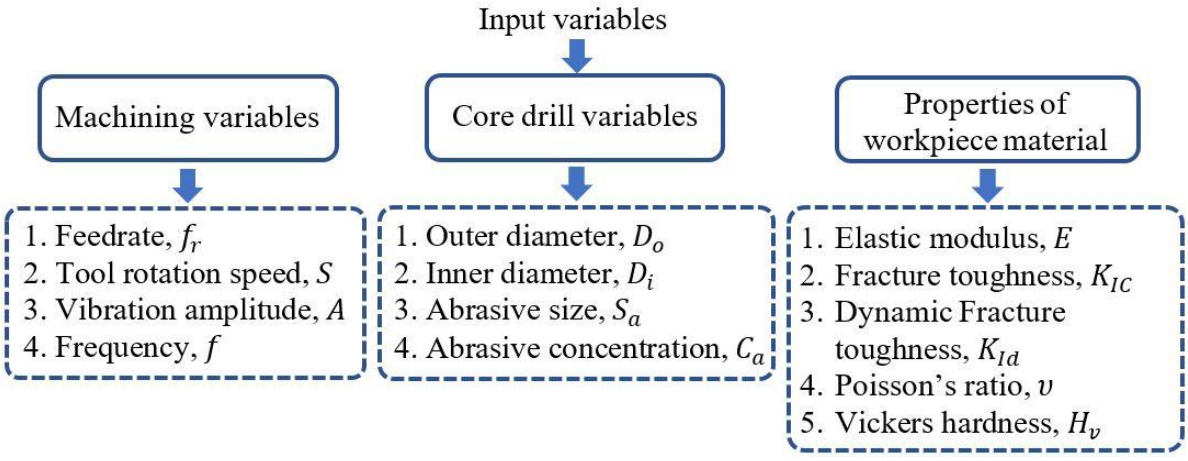

Figure 4.30 Input variables in cutting force model for RUM of rocks

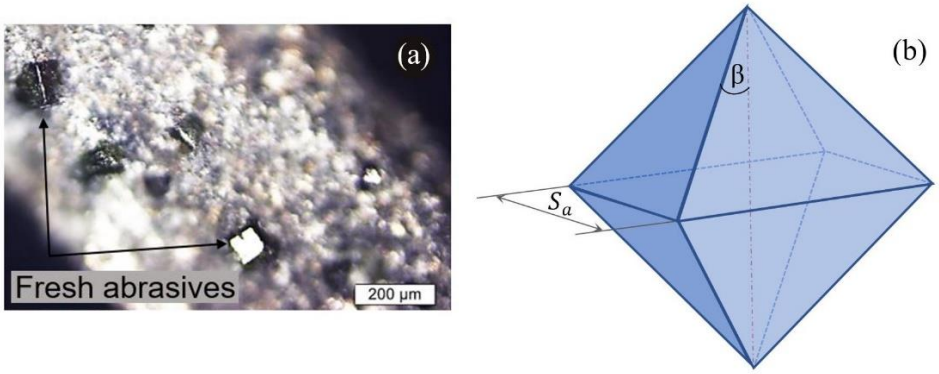

Figure 4.31 Illustration of a diamond abrasive particle simplified as a regular octahedron and microscopic image of the fresh diamond abrasives at the tool end face

Some researchers assumed abrasive particles as spheres in model development [27, 60-66]. However, diamond abrasive particles, as shown in Figure 4.31(a), are more like sharp indenters. In order to establish a more realistic model, this study considers diamond abrasive particles as regular octahedrons. The length of the 12 edges of an abrasive particle is the same and the size of an abrasive particle (S_a) is expressed by the length of an edge.

4.3.2.1 Analysis of rock material removal mechanism

Generally, material removal mechanisms can be classified into brittle fracture and ductile deformation [69]. In grinding of brittle materials, brittle fracture occurs predominantly, and the material is removed after the propagation and intersection of cracks [69]. Recently, researchers have been found that micro scale geometry of abrasive particles affects the material removal mode of brittle materials [70]. This was first reported by Giovanola and Finnie by achieving ductile mode machining of certain types of glasses [70]. Since then, ductile mode machining of brittle materials has been actively investigated by many researchers [69-77]. Bifano et al. studied ductile mode grinding of brittle materials and carried out analytical and experimental investigations to obtain necessary infeed rates for ductile mode grinding [71]. Chen et al. developed a theory to calculate the critical depth of cut in ductile-brittle transition based on the abrasive indentation in ultra-

precision grinding [72]. Liu et al. presented a theoretical analysis for the ductile chip formation mechanism for brittle materials and proved by conducting experiments for ductile cutting of tungsten carbide [73]. Xiao et al. investigated the mechanism of brittle-ductile cutting mode and proposed a mechanistic model to analyze the relationship between deformation, stress states, and undeformed chip thickness [74]. Arif et al. proposed a model based on specific cutting-energy to predict the ductile-brittle transition point in machining of brittle materials and ductile-brittle transition point was identified by measuring the undeformed chip thickness [75]. Zhu et al. carried out a single-grit modeling and simulation study for silicon carbide (SiC) and the results demonstrate that the ductile-regime grinding is dominated if the undeformed chip thickness was kept below a certain value [76]. Cheng et al. presented the interaction behavior and brittle-ductile transition (as shown in Figure 4.32) of micro-grinding of single crystal silicon using a single grit diamond tool and established a model based on the single diamond grit geometry to describe the interaction between the diamond grit and workpiece [77].

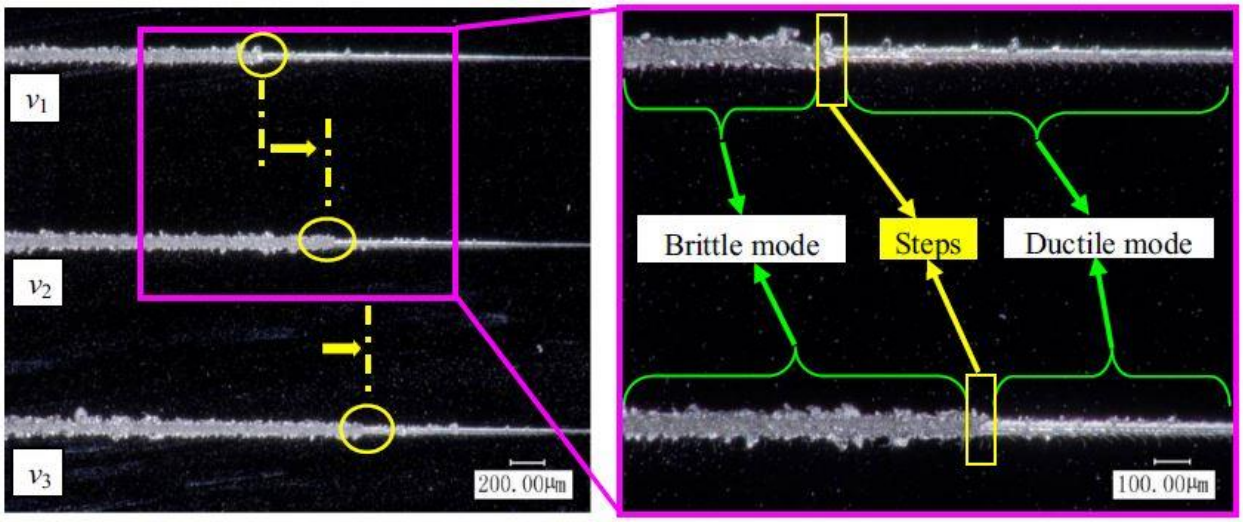

Figure 4.32 Experimental observations of ductile-brittle transition. Adapted from [77] with permission

In RUM, the kinematic motion of the abrasive particles involves in the hybrid motion of ultrasonic vibration in feedrate direction and the tool rotation on horizontal plane. As the tool feeds towards the workpiece during the first half of the ultrasonic vibration cycle (this will be further explained in Section 2.3 by Figure 4.37), abrasive particles at the tool end face start cutting through the material. Up to a certain indentation, material removal by abrasive particles can be considered as ductile mode cutting. A machined surface of basalt rock with machining marks is shown in Figure 4.33. Scratch marks (circled in red) with decreasing cutting depth can be identified as ductile-brittle mode transitions. Due to the intrinsic features of the RUM process, it is difficult to directly observe the fracture mechanism during typical RUM experiments [61, 68]. Nano-indentation tests were carried out to observe the indented zone after high-frequency indentation load. In contrast to traditional hardness experiments, nano-indentation offers in-situ specimen imaging of the sample surface before and after indentation performed. A nano-indenter (Hysitron nano-indenter from Bruker) was used to compare fracture modes of three materials (basalt, glass, and zirconium) under the same indentation load condition. Nano-indentation tests were performed by applying 12 mN peak force under variable load conditions with a constant frequency of 300 Hz using nano-dynamic mechanical analysis test mode. The average stress applied during each indentation test was above 30 GPa, which exceeded the compressive strength of all materials tested. Figure 4.34 provides the in-situ specimen images of the indentation zones generated by a piezo scanner. It can be seen that, basalt has the imprint of the nano-indenter and no cracks propagating from the indented zone can be observed. In comparison to basalt, it is hard to see the imprint of the nano-indenter in zirconium due to considerably high fractures in the indented zone. Glass has moderate fractures compared to the other two materials. Therefore, it can be concluded that the material removal mechanism of basalt rock up to a certain indentation depth is not the

same pure brittle fracture as glass and zirconium have, and it is more appropriate to consider ductile mode and brittle fracture mode material removal mechanisms in RUM model development.

Brittle fragmentation of rocks occurs when abrasive particles are indented beyond a threshold depth into the rock surface, as illustrated in Figure 4.35 [78]. Rock indentation experiments reveal that a highly pulverized zone is created immediately beneath the indentation tip [78, 79]. The initial median crack and secondary side cracks spread out from the pulverized zone forming a cracked zone beneath the pulverized zone [78].

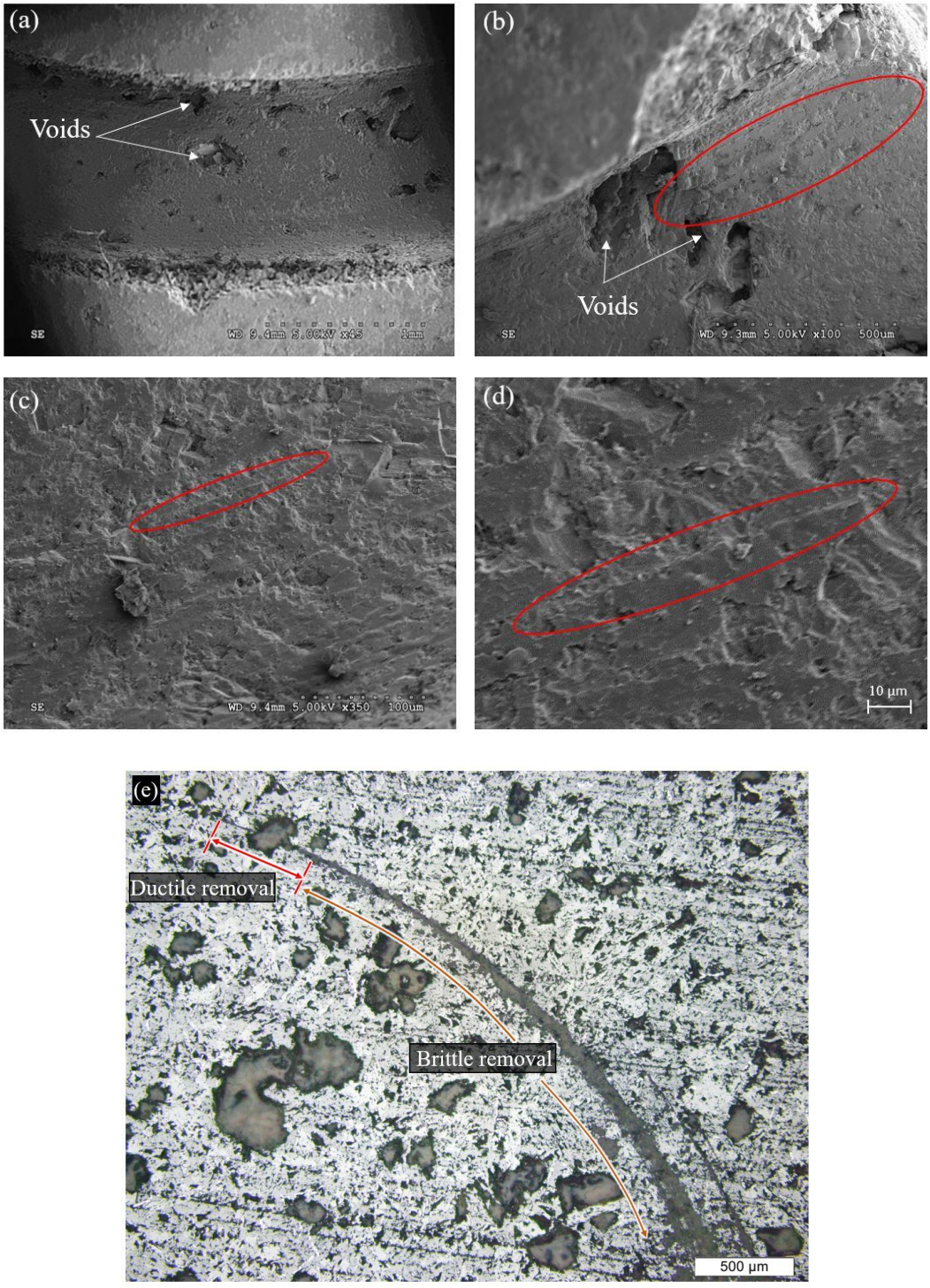

Figure 4.33 SEM and microscopic images of machined surface of basalt rock
(a) Segment of a machined surface of a half way drilled hole, (b) Ductile mode removal close to the inner edge of the hole, (c) Ductile-brittle transition, (d) close view of (c), and (e) Microscopic image of a scratch test

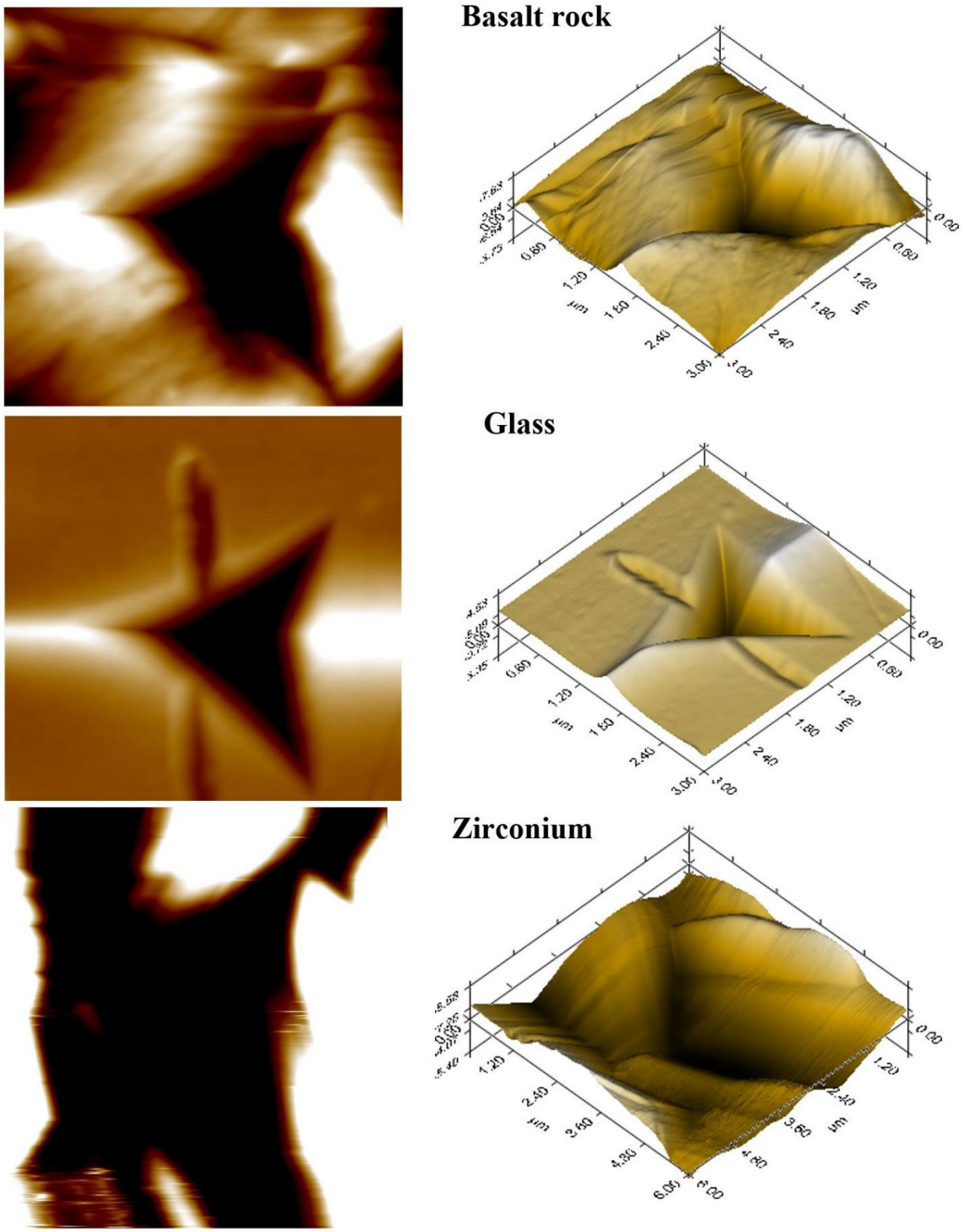

Figure 4.34 Nano-indentation testing of basalt rock, glass, and zirconium

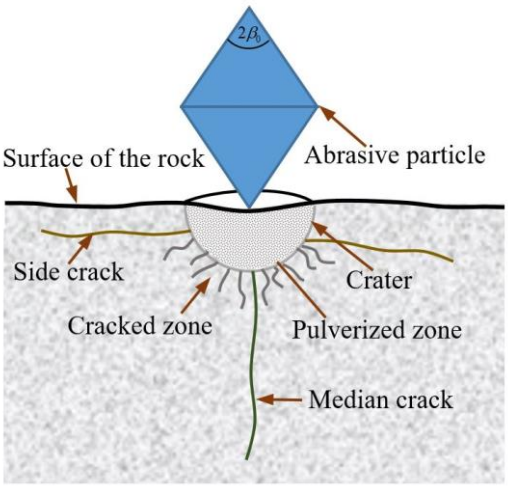

Figure 4.35 General rock fragmentation under indentation

4.3.2.3 Relation between cutting force and penetration depth

The ultrasonic vibration in RUM makes abrasive particles bonded to the tool end face intermittently engage in material removal. Therefore, each abrasive particle on the tool end face contacts the workpiece for a certain time period (Δt – effective cutting time) during one ultrasonic vibration cycle. When the impact force between the abrasive particle and the workpiece reaches its maximum, the abrasive particle reaches the maximum penetration depth while rock being fragmented.

The maximum impact force (F_i), applied by one abrasive particle can be expressed as by the following equation:

$$F_i = \frac{F_m}{N_a} \tag{1}$$

where F_m is the maximum impact force between tool and workpiece, N_a is the number of effective abrasive particles on the tool end face.

The number of abrasive particles on the tool end face (N) can be calculated by Equation (2), which is based on the definition of abrasive concentration. Abrasive concentration 100 is

defined as the weight of abrasives being 4.4 carat/cm^3 (or 0.88 × 10^{-3} g of abrasive particles per mm^3). It is assumed that the distribution of abrasive particles on the tool is uniform and the volume of one abrasive particle is $\sqrt{2}S_a^3/3$ (volume of a regular octahedron).

$$N = \left(\frac{3C_a \times 0.88 \times 10^{-3}}{100\sqrt{2}\rho S_a^3} \right)^{2/3} A_0; \quad A_0 = \frac{\pi}{4}\left(d_0^2 - d_i^2\right) \tag{2}$$

C_a is the abrasive concentration; S_a is the abrasive size, A_0 is the area of the tool end face, d_o and d_i are the outer and inner diameters of the tool, ρ is the density of abrasive material, for diamond; ρ = 3.52 ×10^{-3} g/mm^3.

Abrasive size is related to the pore sizes (d_a^1 and d_a^2) of sieves with standard mesh numbers of S_1 and S_2, and the relationship between abrasive size and standard mesh numbers can be obtained by Equation (4) [80].

$$d_a^i = 25.4\left(\frac{0.6}{S_i}\right); \quad i = 1, 2 \tag{3}$$

$$S_a = 7.62\left(\frac{1}{S_1} + \frac{1}{S_2}\right) \tag{4}$$

Abrasive protrusion height is defined as the distance between the sharp edge of an abrasive particle and the base surface of bond material of a tool [81]. Protrusion height of abrasive particles influences the machining performances, as an example low protrusion height increases the load on a single abrasive particle resulting an increase in cutting force. Studies showed that the abrasive protrusion height follows a Gaussian distribution [80-86]. Therefore, all of the abrasive particles would not participate in the material removal in the cutting zone. A number of effective abrasive

particles (N_a) have certain protrusion height or higher can be calculated by using Gaussian function as shown in Equation (5) [86].

$$N_a = N \int_{h_{\max}}^{\mu} \frac{1}{\sigma\sqrt{2\pi}} e^{-(h-\mu)^2/2\sigma^2} dh \tag{5}$$

where σ is the standard deviation, μ is the mean value of abrasive protrusion height, and $h_{\max}$ is the maximum protrusion height.

It is assumed that the abrasive particles are rigid. Therefore, the impulse in terms of the maximum impact force between tool and workpiece during one ultrasonic vibration cycle can be described as:

$$Impulse = \int_{Cycle} F_m dt \approx F_m \Delta t \tag{6}$$

The abrasive particles on the tool end face oscillate sinusoidally due to ultrasonic vibration. The position (z) of an abrasive particle at time (t) in the axial direction of the tool (z direction) can be described by the following equation:

$$z = A\sin(2\pi f t) \tag{7}$$

where A is the ultrasonic vibration amplitude, f is the frequency of the ultrasonic vibration.

Figure 4.36 shows the illustration of the motion and ductile mode and brittle fracture mode material removal by an abrasive particle. z_0 is the maximum penetration depth achieved by a single abrasive particle.

As shown in Figure 4.37, an abrasive particle takes $\Delta t/2$ time to move from $z = A - z_0$ to $z = A$ and Δt can be calculated by the following equation:

$$\Delta t = \frac{1}{\pi f}\left[\frac{\pi}{2} - \sin^{-1}\left(1 - \frac{z_0}{A}\right)\right] \tag{8}$$

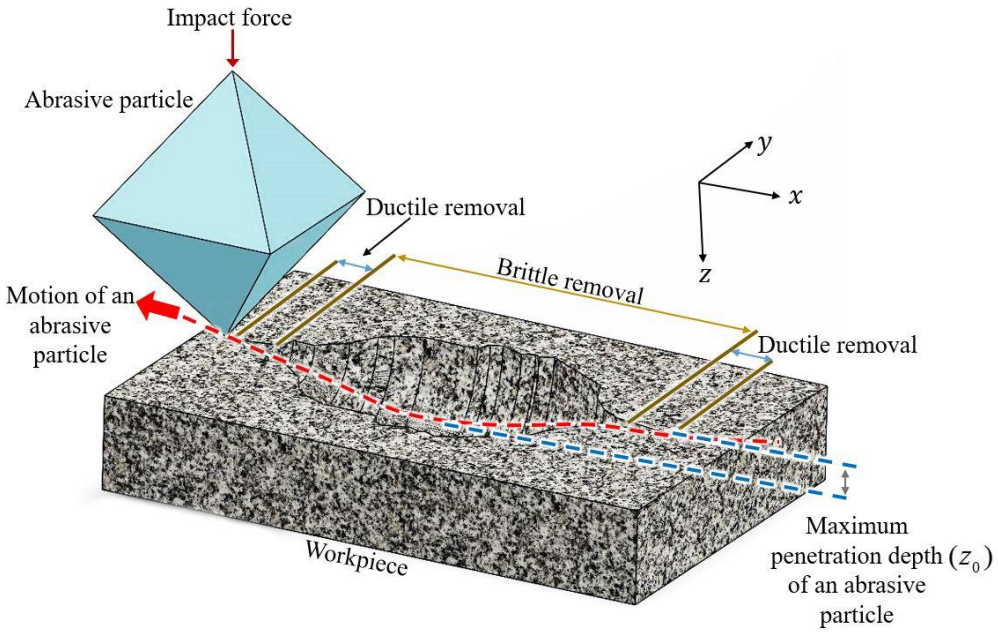

Figure 4.36 Illustration of the motion and material removal of a single abrasive particle

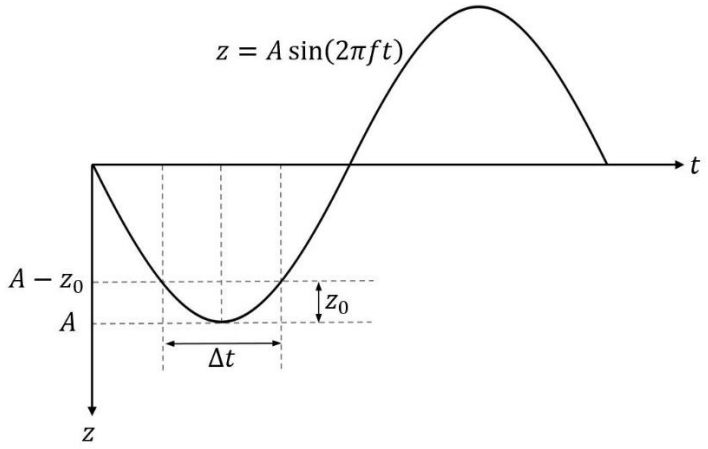

Figure 4.37 Effective cutting time per ultrasonic vibration cycle

The impulse can also be expressed in terms of the cutting force during one ultrasonic vibration cycle by the following equation:

$$Impulse = \frac{1}{f}F \tag{9}$$

where F is the cutting force measured during RUM of rocks.

By equaling two impulses (Equations (6) and (9)), the following relationship between F and F_m can be obtained:

$$F = \Delta t f F_m \tag{10}$$

By substituting Equations (1) and (8) into Equation (10), the relation between F and F_i can be expressed as:

$$F = \frac{N_a}{\pi}\left[\frac{\pi}{2} - \sin^{-1}\left(1 - \frac{z_0}{A}\right)\right]F_i \tag{11}$$

The maximum penetration depth (z_0) can be obtained by using the definition of Vickers hardness as following equation:

$$z_0 = \left(\frac{F_i}{2H_v \tan\beta\sqrt{2+\tan^2\beta}}\right)^{1/2} \tag{12}$$

By substituting Equation (11) into Equation (12), the relation between F and Z_0 can be expressed as:

$$z_0 = \left(\frac{\pi \cdot F}{2N_a H_v\left[\frac{\pi}{2} - \sin^{-1}\left(1 - \frac{z_0}{A}\right)\right]\tan\beta\sqrt{2+\tan^2\beta}}\right)^{1/2} \tag{13}$$

4.3.2.5 Volume of material removed by one abrasive particle

The effective cutting distance (L) is the distance that one abrasive particle travels during the effective cutting time as shown in Figure 4.38 (a). It can be calculated by

$$L = \frac{2\pi S R_d}{60}\Delta t \tag{14}$$

where R_d is the distance from an abrasive particle to the center of the tool, S is the tool rotation speed.

For simplification, assume that the abrasive particle is at the center of the tool end surface between d_i and d_o. Therefore, R_d can be calculated as follows:

$$R_d = \left(\frac{d_o + d_i}{4} \right) \tag{15}$$

The critical depth of cut for brittle-to-ductile transition (d_c) can be determined by the formula proposed by Chen *et al*. [48].

$$d_c = k_c \cot \beta_0 \sqrt{\frac{2\lambda_0}{\alpha}} \left(\frac{K_{Id}}{H_v} \right)^2 \tag{16}$$

where $\beta_0 = \sin^{-1}\left(1/\sqrt{3} \right)$ is the half-top angle of an abrasive particle as shown in Figure 4.31, α is the geometric factor of the shape of the abrasive particle; for axially symmetric shapes, $\alpha = 1$ [87, 88], λ_0 is the integrative factor whose value best fitted to experimental data is 1.6×10^4 [89], K_{Id} is the dynamic fracture toughness of the material, and k_c is the affecting coefficient of coolant to brittle-to-ductile transition of the material.

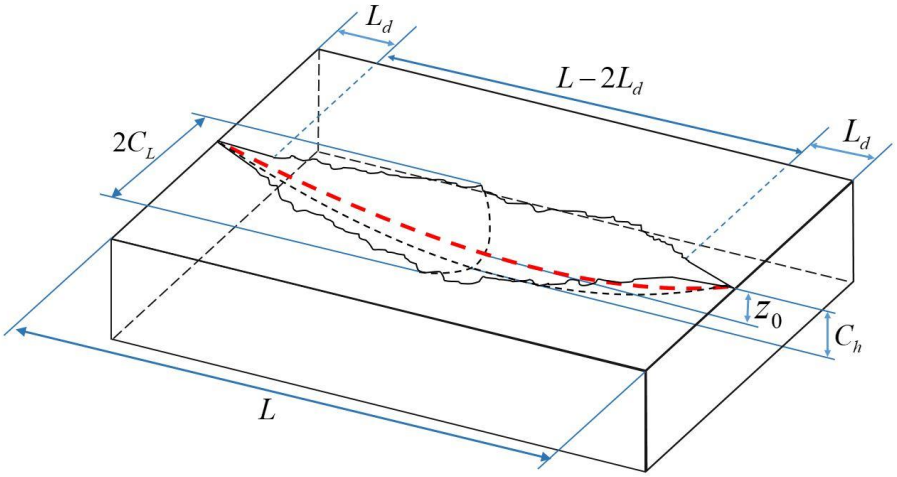

(a) Illustration of the ductile and brittle modes removal

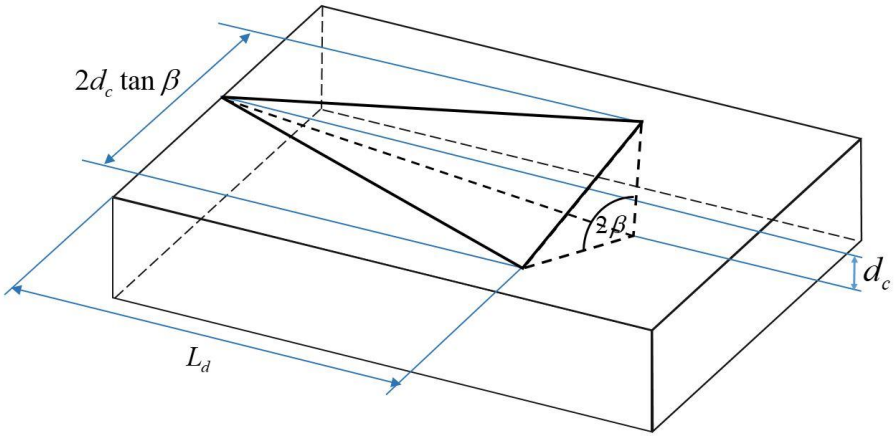

(b) Illustration of the volume of ductile mode removal

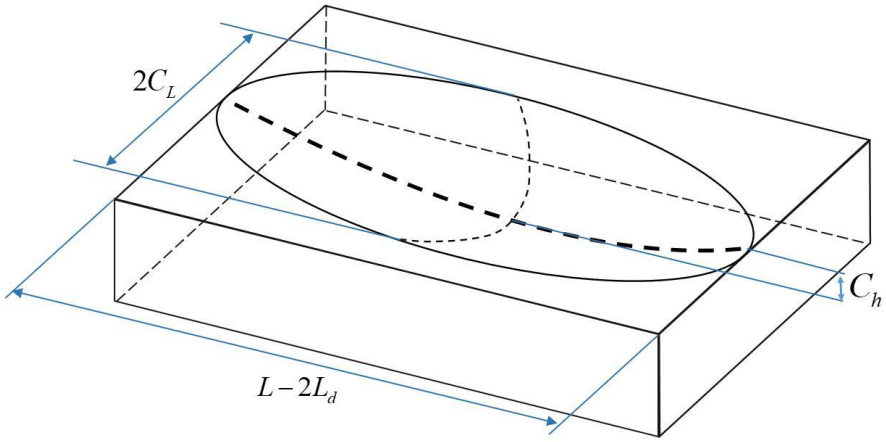

(c) Illustration of the simplified volume of brittle fracture mode removal

Figure 4.38 Illustration of the volume of material removed by one abrasive particle

As shown in Figure 4.38 (b), ratio between ductile mode cutting distance (L_d) and effective cutting distance can be deduced from the proportional relationships and hence brittle removal distance (L_b) can be expressed by Equation (18):

$$L_d = \frac{L}{2z_0} d_c \tag{17}$$

$$L_b = L\left(1 - \frac{d_c}{z_0}\right) \tag{18}$$

The volume of material removed by one abrasive particle during the effective cutting time ($V_{\Delta t}$) can be divided into two segments as follows:

$$\begin{cases} V_d, & z_0 \le d_c \\ V_b, & z_0 > d_c \end{cases} \tag{19}$$

where V_d is volume of ductile mode material removal and V_b is volume of brittle fracture mode material removal.

Therefore, as shown in Figure 4.38 (a), $V_{\Delta t}$ can be expressed by Equation (20).

$$V_{\Delta t} = V_d + V_b \tag{20}$$

As shown in Figure 4.38 (b), V_d can be obtained from the following integral. According to the geometrical and proportional relationships V_d can be expressed by Equation (22).

$$V_d = 2\int_0^{L_d} A' dx \tag{21}$$

$$V_d = \frac{d_c^3 L^5}{108\, z_0^5} \tag{22}$$

The volume of brittle removal can be simplified as a volume of a half ellipsoid, which has half-axes lengths of C_L, C_h, and $L_b/2$, as shown in Equation (23).

$$V_b = \frac{1}{3}\pi C_L C_h L_b \tag{23}$$

where C_L and C_h are lateral crack length and depth as shown in Figure 4.38 (c).

Lateral crack length C_L and lateral crack depth C_h were determined by Marshall *et al.* [90].

$$C_L = C_2\left(\frac{1}{\tan\beta}\right)^{5/12}\left(\frac{E^{3/4}}{H_v K_{IC}\left(1-\nu^2\right)^{1/2}}\right)^{1/2} F_i^{5/8} \tag{24}$$

$$C_h = C_2\left(\frac{1}{\tan\beta}\right)^{1/3}\frac{E^{1/2}}{H_v}F_i^{1/2} \tag{25}$$

The actual volume of material removed by one abrasive particle during one ultrasonic vibration cycle (V) is assumed to be proportional to the theoretical volume of material removed by one abrasive particle during the effective cutting time ($V_{\Delta t}$). This relationship can be expressed as follows:

$$V = kV_{\Delta t} \tag{26}$$

where k is the proportionality parameter that is assumed to be a constant for a given rock type.

4.3.2.6 The cutting force model formulation

The material removal rate of one abrasive particle (MRR_a) is equal to the product of V and f. Therefore, MRR_a can be expressed as follows:

$$MRR_a = fV \tag{27}$$

Material removal rate of the tool (MRR_C) can be calculated from the summation of material removal rate of all abrasive particles on the tool end face and the following relationship can be obtained:

$$MRR_C = N_a MRR_a \tag{28}$$

MRR_C can also be calculated in terms of feedrate (f_r) and area of the tool end face (A_0).

$$MRR_C = f_r A_0 \tag{29}$$

By equaling Equations (28) and (29) and substituting Equation (27), the following relationship can be obtained:

$$N_a fV = f_r A_0 \tag{30}$$

By substituting Equations (1), (8), (10), (14), (16), (18), (20), (22-26), and (30), the cutting force model can be expressed as follows:

$$F = \left\{ \frac{N_a^{1/8} \tan^{3/4}\beta \, K_{IC}^{1/2} (1-\nu^2)^{1/4} \left[\pi/2 - \sin^{-1}\left(1 - z_0/A\right)\right]^{1/8} \left(27 \cdot 120^5 \alpha^{3/2} H_v^6 Z_0^6 f_r \pi (d_o - d_i) f^4 \right.}{36 \cdot 120^4 \alpha \, f^4 H_v^{5/2} z_0^4 \pi^{17/8} k C_2^2 S \left[z_0 H_v^2 \sqrt{\alpha} - k_c K_{Id}^2 \cot\beta_0 \sqrt{2\lambda_0} \right]} \right.$$

$$\left. - \frac{N_a k k_c^3 \cot^3\beta_0 (2\lambda_0)^{3/2} K_{Id}^6 \left\{ S\left[\pi/2 - \sin^{-1}\left(1 - z_0/A\right)\right]\right\}^5 \Big)}{36 \cdot 120^4 \alpha \, f^4 H_v^{5/2} z_0^4 \pi^{17/8} k C_2^2 S \left[z_0 H_v^2 \sqrt{\alpha} - k_c K_{Id}^2 \cot\beta_0 \sqrt{2\lambda_0} \right]} \right\}^{8/9} \quad (31)$$

There are four unknowns in Equation (31), k, k_c, N_a, and z_0. Since k, k_c, and N_a are assumed as constants they can be obtained by preliminary experiments. Therefore, cutting force can be obtained by solving Equations (31) and (13) simultaneously.

4.3.3 Obtaining proportionality parameter k

4.3.3.1 Methodology of obtaining proportionality parameter k

Once the cutting force is obtained from preliminary experiments and substituted into Equation (13), z_0 can be calculated. Then the proportionality parameter k can be calculated by the following equation:

$$k = \frac{V}{V_{\Delta t}} = \frac{f_r A_0 / N_a f}{V_d + V_b} = f_r A_0 \Big/ \left[\frac{2^{3/2} N_a \lambda_0^{3/2} k_c^3 \cot^3\beta_0 \, K_{Id}^6}{108 \cdot f^4 \alpha^{3/2} H_v^6} \left\{ \frac{S(d_o + d_i)}{120 z_0} \left[\frac{\pi}{2} - \sin^{-1}\left(1 - \frac{z_0}{A}\right)\right]\right\}^5 \right]$$

$$+\frac{2\pi^{17/8} C_2^2 E^{7/8} S(d_o + d_i)\left[z_0 - k_c \cot\beta_0 \sqrt{2\lambda_0/\alpha}\left(K_{Id}/H_v\right)^2 F^{9/8}\right]}{720\ z_0\ N_a^{1/8} \tan^{3/4}\beta\, H_v^{3/2} \sqrt{K_{IC}\left(1-\nu^2\right)^{1/2}}\left[\pi/2 - \sin^{-1}\left(1 - z_0/A\right)\right]^{1/8}}\Bigg] \quad (32)$$

4.3.3.2 Experimental setup, conditions, and procedures

In this study, an igneous rock type, basalt, was chosen as the workpiece material. Igneous rocks have a higher strength than the other main rock types, sedimentary and metamorphic. The dimensions of the workpiece are 100 mm × 40 mm × 9 mm. Figure 4.39 shows the surface of the polished basalt rock sample. The properties of the basalt rock are shown in Table 4.8.

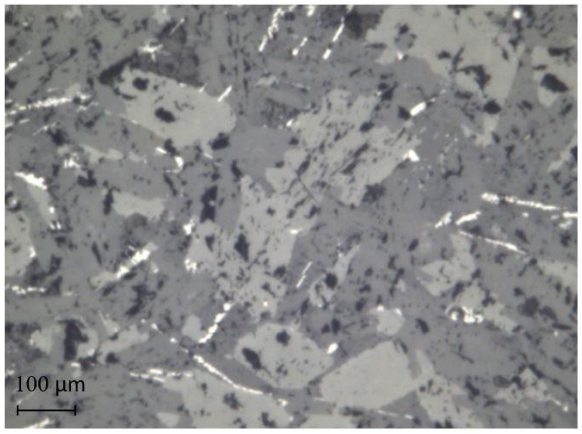

Figure 4.39 Microscopic image of a polished basalt rock sample

The preliminary experiments to obtain k were performed on a rotary ultrasonic machine (Series 10, Sonic-Mill, Albuquerque, New Mexico, USA). As shown in Figure 4.14, the experimental setup consists of an ultrasonic spindle system, an air-charged hydraulic feeding system, a coolant system, and a data acquisition system.

A dynamometer (Kistler 9272, Kistler Instrument Corp, Switzerland) was used to measure the cutting force along the tool axis (feedrate) direction, and the workpiece was mounted on top of the

fixture of the dynamometer. A charge amplifier (Kistler 5070, Kistler Instrument Corp, Switzerland) was used to amplify the signal from the dynamometer and an analog-to-digital converter (PCIM-DAS 1602/16, Measurement Computing Corporation, Norton, MA, USA) was used to convert the signal to a digital signal. Cutting force data were recorded by using the Dynoware software (Version 2.4.1.6 type 2825A-02, Kistler Instrument Corp, Switzerland).

Table 4.8 Properties of basalt rock [91, 92]

Property	Unit	Basalt
Density	kgm^{-3}	2680 – 2940
Elastic modulus	GPa	50.68
Fracture toughness	$MPa\sqrt{m}$	1.12
Poison's ratio	–	0.2
Vickers hardness	GPa	2.67

4.3.3.3 Design of experiments

Six input variables (tool rotation speed, feedrate, ultrasonic power, abrasive size and concentration, and tool size) were studied. Tool specifications and experimental conditions are listed in Table 4.9 and Table 4.10, respectively. Three replicates were used for each experimental condition and the output variable was cutting force. For each experimental run, tool was dressed to increase the number of effective abrasive particles, which is approximately 60% of the total number of grains and it is applied for the calculations [84].

Table 4.9 Tool specifications

Tool No.	Mesh size (No.)	Average abrasive size (mm)	Concentration	Outer diameter (mm)	Inner diameter (mm)
1	60-80	0.213	100	12	10
2	80-100	0.163	100	12	10
3	100-120	0.137	100	12	10
4	140-170	0.096	100	12	10
5	100-120	0.137	50	12	10
6	100-120	0.137	150	12	10
7	100-120	0.137	200	12	10
8	100-120	0.137	100	9	7
9	100-120	0.137	100	15	13
10	100-120	0.137	100	18	16

Table 4.10 Experimental conditions for obtaining k

Experiment No.	Ultrasonic power (%)	Tool rotation speed (rpm)	Feedrate (mm/s)	Tool No.
1	20, 30, 40, 50	3000	0.02	3
2	40	2000, 2500, 3000, 3500	0.02	3
3	40	3000	0.01, 0.02, 0.03, 0.04	3
4	40	3000	0.02	1, 2, 4
5	40	3000	0.02	5, 6, 7
6	40	3000	0.02	8, 9, 10

4.3.3.4 Analysis of proportionality parameter (*k*) from experimental results

In this section, the proportionality parameter (k) is estimated from the experimental results. For each experimental run, V and $V_{\Delta t}$ are obtained using measured cutting force and input variables. The relationship between V and $V_{\Delta t}$ is plotted in Figure 4.40. Error bars represent the standard deviation of $V_{\Delta t}$. The slope of the least-squares regression line passing through the origin is the estimated proportionality parameter for the given workpiece material. The R^2 value of the

regression line indicates that 94.5% of the experimental data can be predicted by this line. The estimated k value from all of the experimental results for the basalt workpiece is 0.0066.

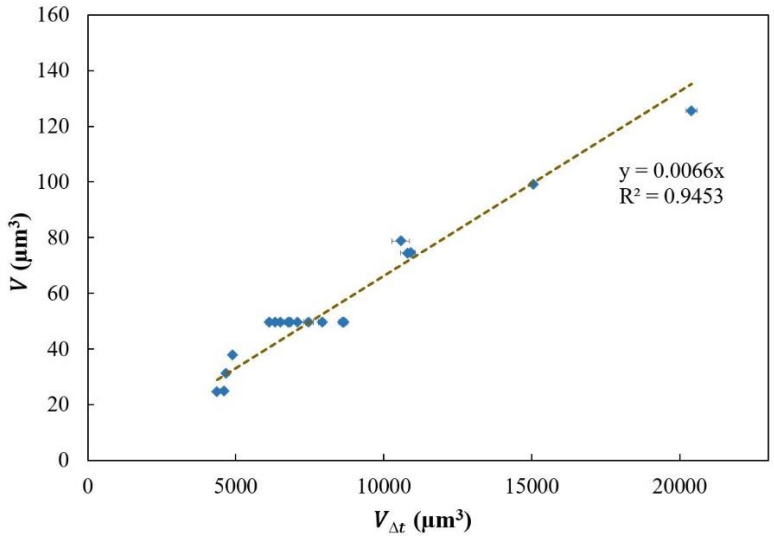

Figure 4.40 Calculation of proportionality parameter from preliminary experimental results

Figure 4.41 shows the effects of input variables (feedrate, tool rotation speed, ultrasonic vibration amplitude, abrasive size, abrasive concentration, and tool outer diameter) on proportionality parameter (k). It can be seen that the estimated k is always $\pm$ 0.0015 to the obtained k values and there are no strong correlations between the input variables and k values. Therefore, it can be assumed that k is a constant for the basalt rock material and this value can be applied to predicting cutting force over a wide range of input variables.

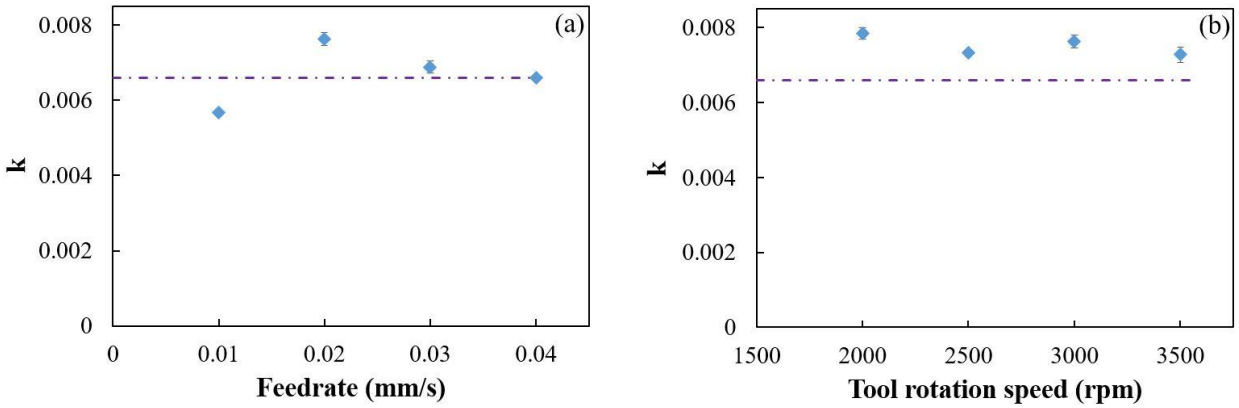

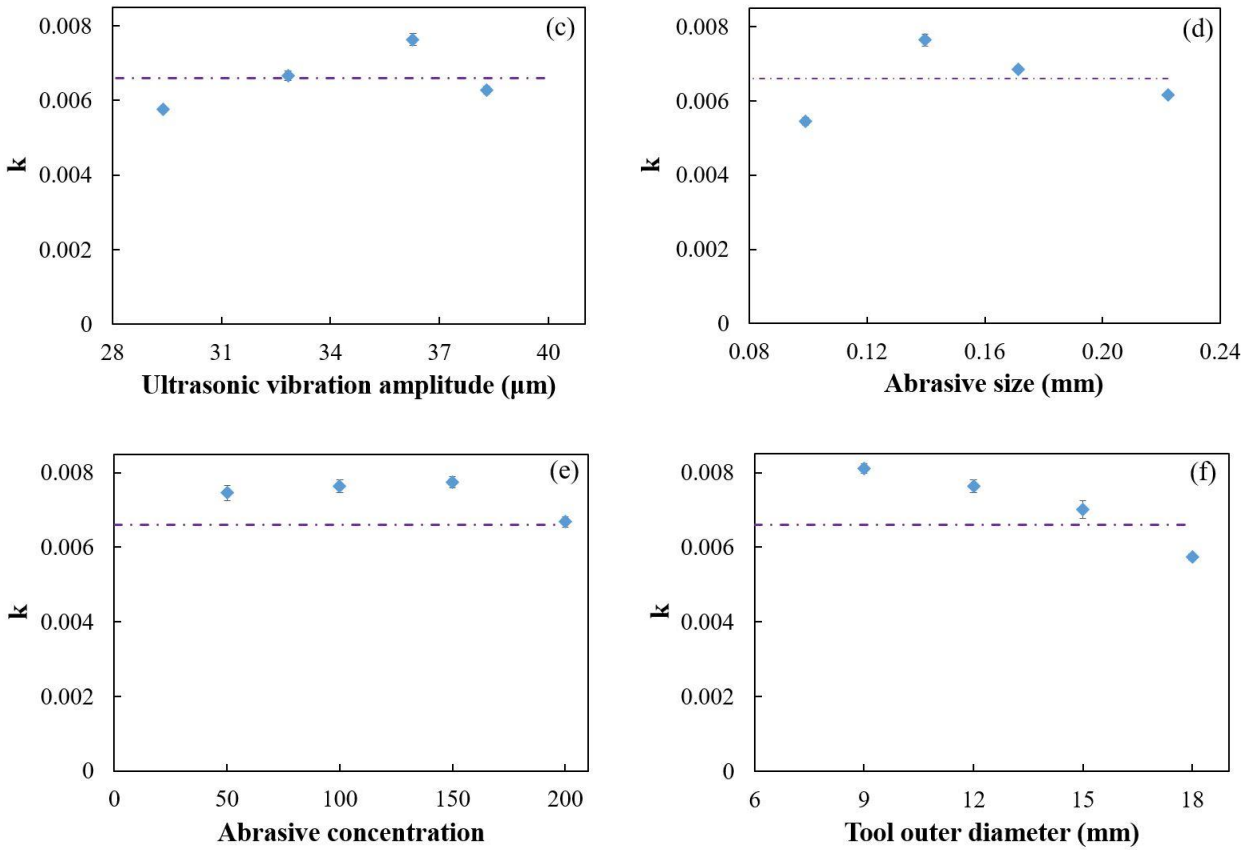

Figure 4.41 Influences of input variables on k

4.3.4 Cutting force model prediction

Based on this mechanistic cutting force model, cutting force is predicted with different input variables, including feedrate, tool rotation speed, ultrasonic vibration amplitude, abrasive size, abrasive concentration, and tool size. The predictions of cutting force and three intermediate variables are plotted in Figures 4.42-4.47. These intermediate variables include maximum impact force, penetration depth, and the effective cutting time of one abrasive particle.

According to the predicted results, cutting force increases approximately linearly as feedrate increases and nonlinearly increases as mesh size, abrasive concentration, and tool size increase. Cutting force decreases nonlinearly as tool rotation speed increases and slightly decreases as ultrasonic vibration amplitude increases. Liu *et al*. developed a cutting force model for RUM of

brittle materials and reported that cutting force varies slightly as ultrasonic vibration amplitude changes [59]. Cong *et al.* reported a cutting force model for RUM of CFRP and had similar outcomes, which showed that ultrasonic vibration amplitude has minimal effects on cutting force [27]. Zhang *et al.* developed a mathematical model for cutting force in rotary ultrasonic face milling of brittle materials and reported that cutting force varies slightly as ultrasonic vibration amplitude changes [93].

Figure 4.42 shows the effects of feedrate on cutting force and intermediate variables. According to Equations (29) and (30), $MRR_C = f_r A_0$; $N_a \cdot f \cdot V = f_r A_0$, material removal rate of tool and the actual material removal rate of one abrasive particle (V) increase as feedrate increases for fixed ultrasonic vibration frequency. Penetration depth should increase as V increases. Increasing penetration depth leads to longer effective cutting time and larger maximum impact force as described in Equations (8) and (13). From Equations (1) and (10), $F = \Delta t f N_a F_i$ can be derived. When the number of abrasive particles and ultrasonic frequency are fixed, cutting force increases as the effective cutting time and the maximum impact force increase.

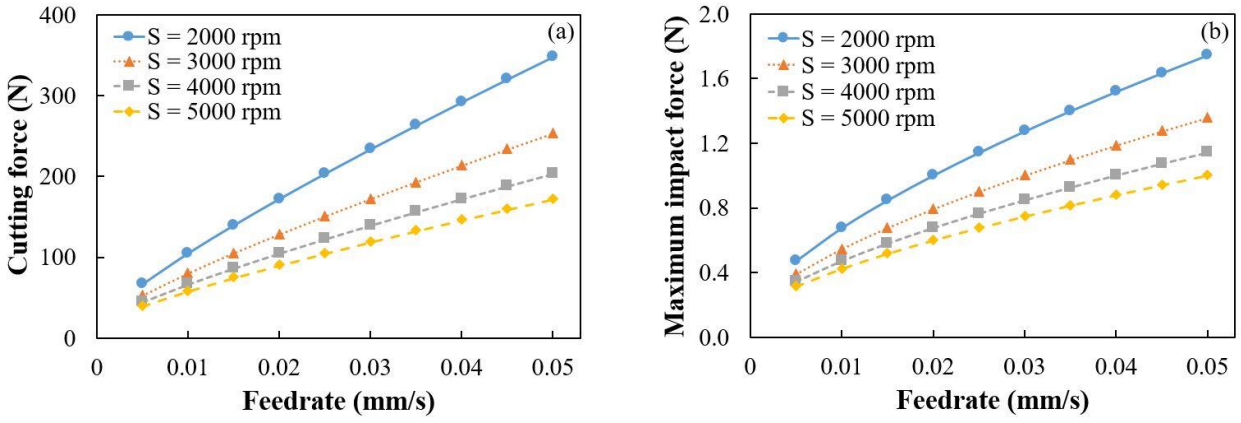

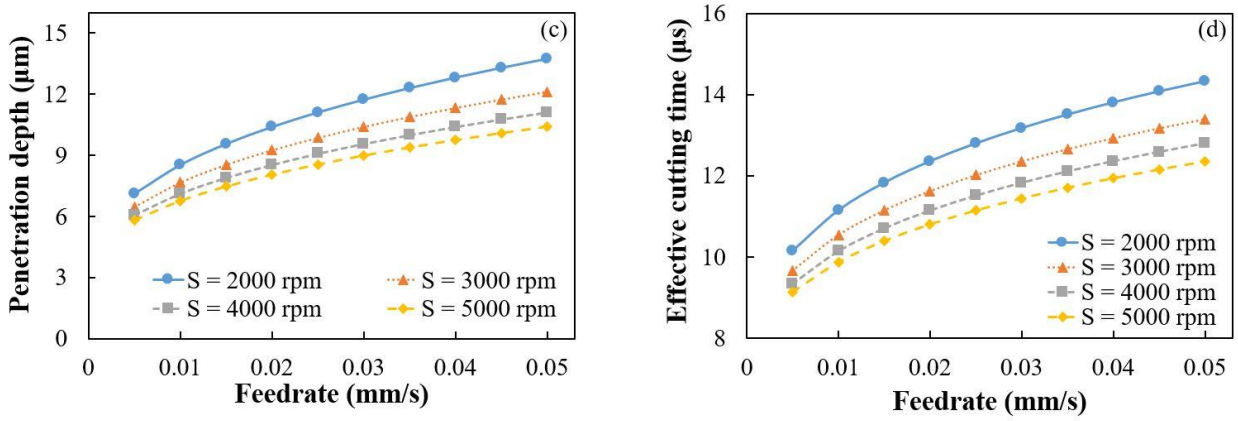

Figure 4.42 Influences of feedrate on cutting force and intermediate variables

A = 36.27 μm, $S_1 - S_2$ = 100 – 120, C_a = 100, (d_o, d_i) = (12, 10) mm

Figure 4.43 illustrates the influences of tool rotation speed on cutting force and intermediate variables. With a fixed feedrate, material removal rate of the tool and the actual material removal rate of one abrasive particle (V) keep unchanged as described by Equations (29) and (30), $MRR_C = f_r A_0$; $N_a \cdot f \cdot V = f_r A_0$. According to Equation (14), as tool rotation speed increases, effective cutting distance increases. This leads to a reduction in penetration depth. As penetration depth decreases, the effective cutting time and the maximum impact force decrease. According to $F = \Delta t f N_a F$, when tool rotation speed increases, cutting force decreases for fixed number of abrasive particles and ultrasonic frequency.

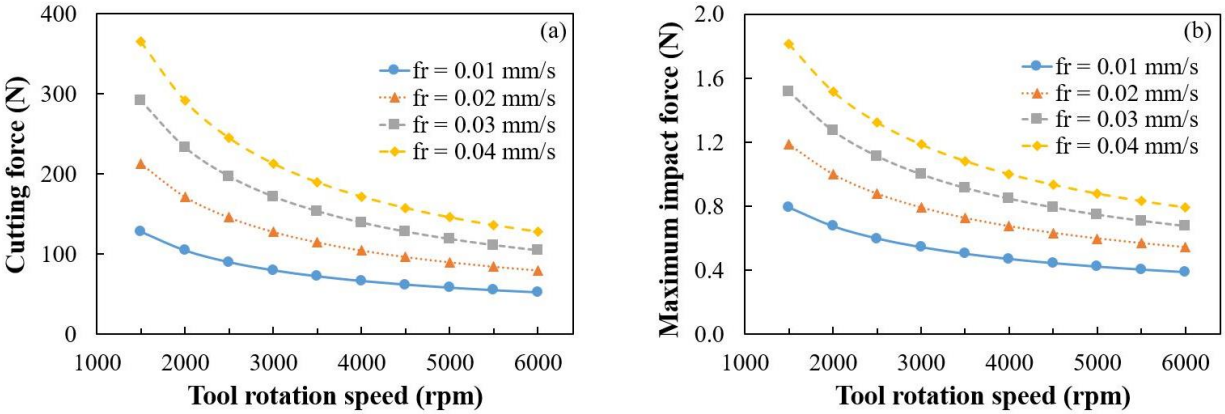

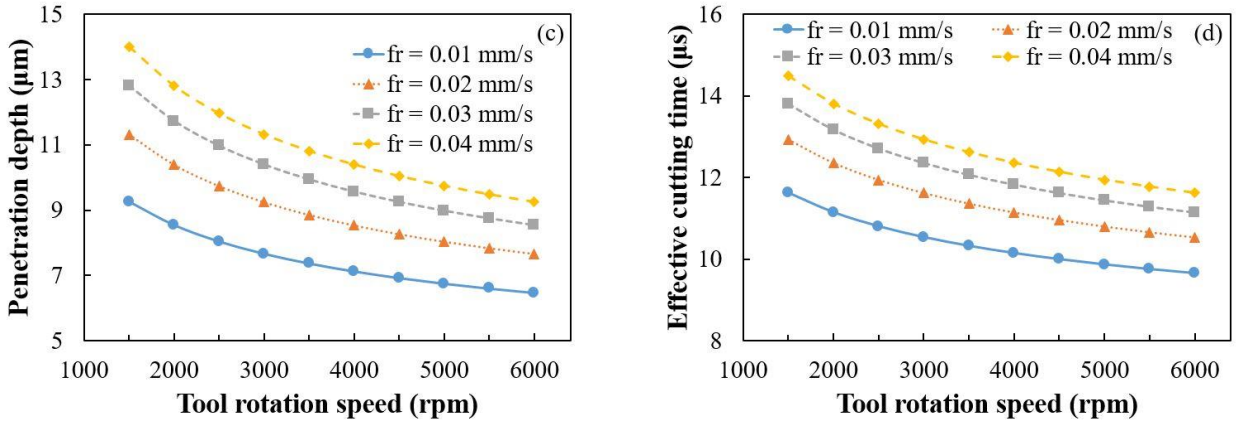

Figure 4.43 Influences of tool rotation speed on cutting force and intermediate variables

$A = 36.27$ μm, $S_1 - S_2 = 100 - 120$, $C_a = 100$, $(d_o, d_i) = (12, 10)$ mm

Figure 4.44 shows the effects of ultrasonic vibration amplitude on cutting force and intermediate variables. As ultrasonic vibration amplitude increases, the maximum impact force and penetration depth increase. According to the Equation (8), with the increase of ultrasonic vibration amplitude, the ratio of $\frac{z_0}{A}$ decreases, which leads to a lower effective cutting time. However, the increasing rate of effective cutting time is greater than the decreasing rate of the maximum impact force. Therefore, based on $F = \Delta t f N_a F$, when ultrasonic vibration frequency and the number of abrasive particles remain unchanged, cutting force slightly decreases as ultrasonic vibration amplitude increases.

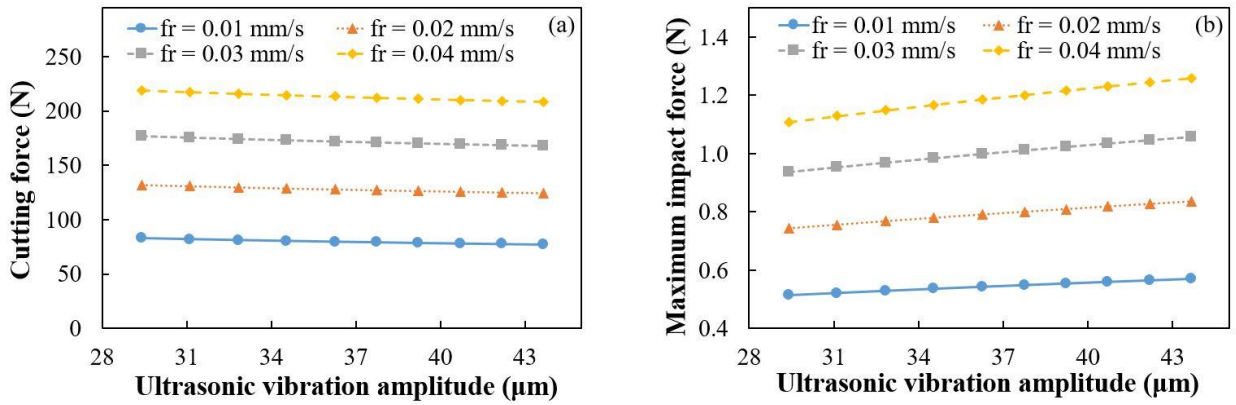

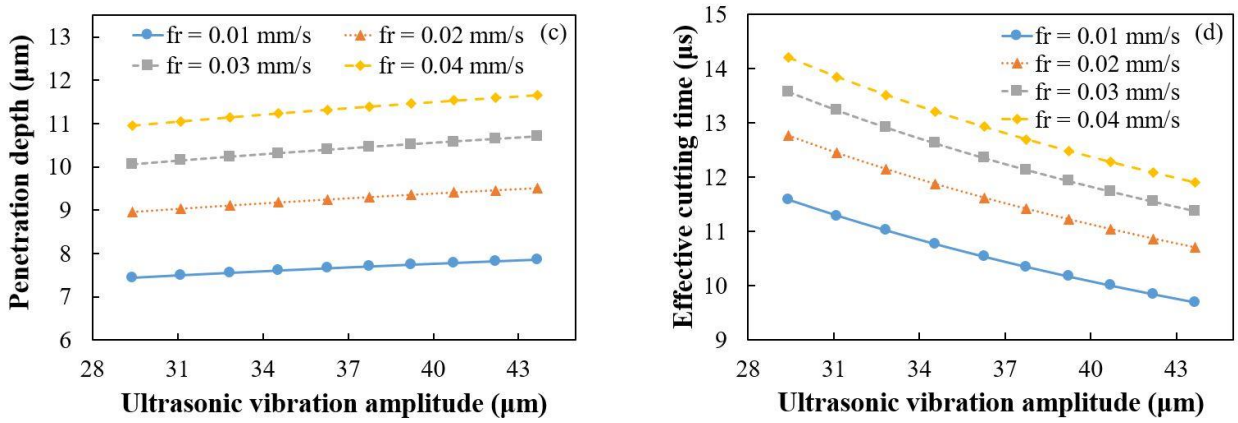

Figure 4.44 . Influences of ultrasonic vibration amplitude on cutting force and intermediate variables

S = 3000 rpm, $S_1 - S_2$ = 100 – 120, C_a = 100, (d_o, d_i) = (12, 10) mm

Figure 4.45 illustrates the influences of mesh size on cutting force and intermediate variables. When mesh size increases, the number of abrasive particles increases as decribed by Equations (2) - (4). If feedrate remains unchanged, MRR_C does not change. According to Euqations (29) and (30), $MRR_C = f_r A_0$; $N_a \cdot f \cdot V = f_r A_0$, V has to decrease to keep MRR_C unchanged. Therefore, the maximum impact force and penetration depth decrease. As penetration depth decreases effective cutting time also decreases as decribed by Equation (8). However, F and Δt decrease and N_a increases as mesh size increases are resulted in cutting force increase, according to $F_C = \Delta t f N_a F$, as increasing rate of N_a dominates the decreasing rate of $F \cdot \Delta t$ when ultrasonic vibration frequency remains unchanged.

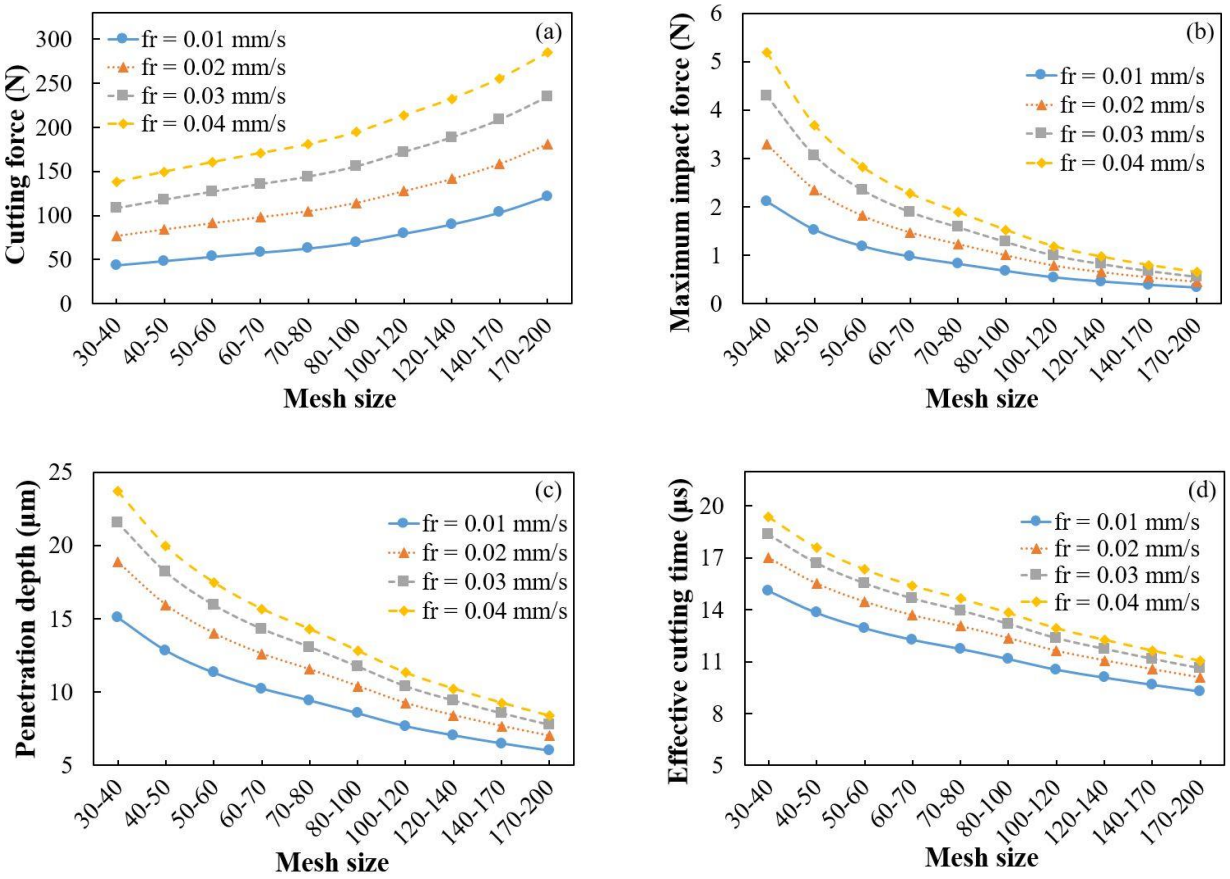

Figure 4.45 Influences of mesh size on cutting force and intermediate variables

S = 3000 rpm, A = 36.27 μm, C_a = 100, (d_o, d_i) = (12, 10) mm

Figure 4.46 shows the effects of abrasive concentration on cutting force and intermediate variables. When abrasive concentration increases, the number of abrasive particles increases as decribed by Equations (2) - (4). With a fixed feedrate, material removal rate of the tool and the actual material removal rate of one abrasive particle (V) keep unchanged as described by Equations (29) and (30), $MRR_C = f_r A_0$; $N_a \cdot f \cdot V = f_r A_0$. From Equations (29) and (30) $MRR_C = N_a \cdot f \cdot V$ can be derived. To keep MRR_C unchanged, V has to decrease when abrasive concentration increases. As V decreases, the maximum impact force and penetration depth decrease, which leads to a reduction in the effective cutting time as decribed by Equation (8). Similar to the effects of mesh size on cutting force, cutting force increases as abrasive

concentration increases, since F and Δt decrease and N_a increases as abrasive concentration increases.

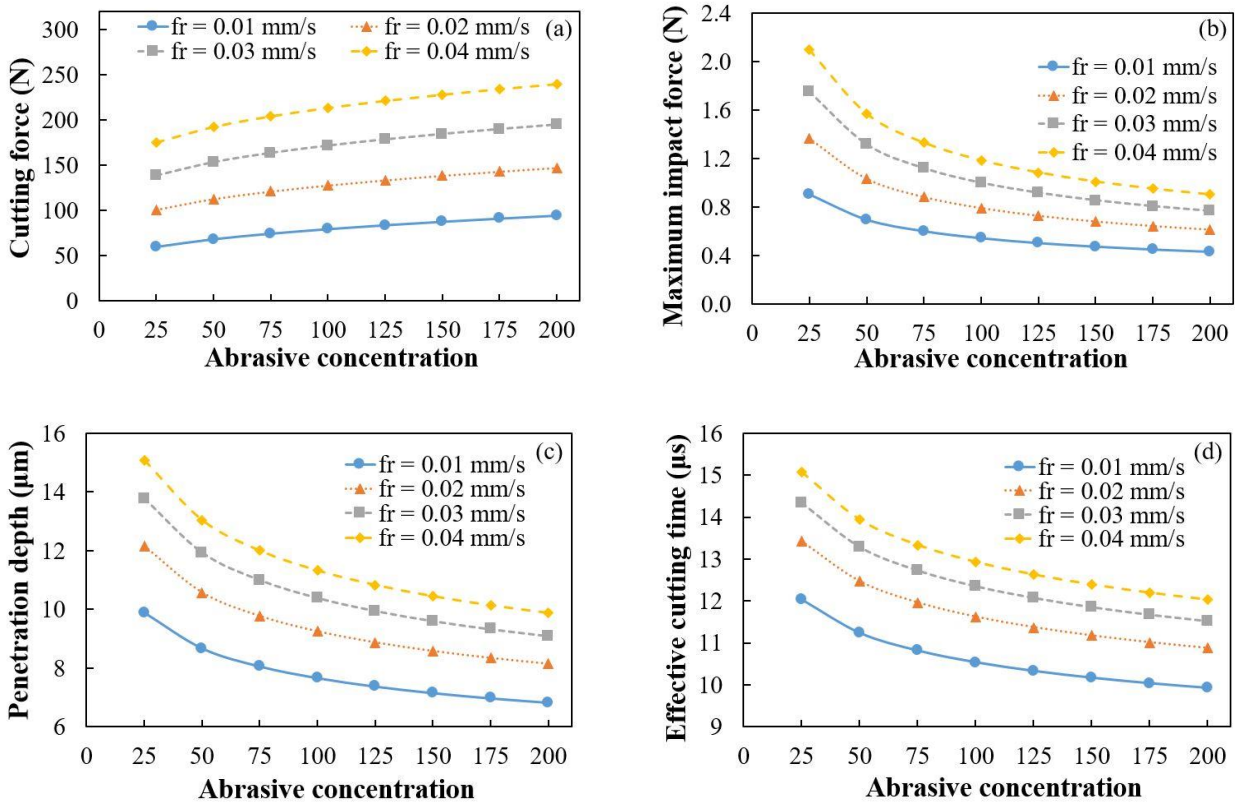

Figure 4.46 Influences of abrasive concentration on cutting force and intermediate variables
S = 3000 rpm, A = 36.27 μm, $S_1 - S_2$ = 100 – 120, C_a = 100, (d_o, d_i) = (12, 10)

Figure 4.47 shows the effects of tool size on cutting force and intermediate variables. When tool size increases, the number of abrasive particles increases as decribed by Equation (2). With a fixed feedrate, material removal rate of the tool increases as tool size increases, as described by Equation (29), $MRR_C = f_r A_0$. According to $MRR_C = N_a \cdot f \cdot V$, V has to decrease since increasing rate of MRR_C is less than the increasing rate of N_a when tool size increases. As V decreases, the maximum impact force and penetration depth decrease, which leads to a reduction in the effective cutting time as decribed by Equation (8). Similar to the effects of mesh size on cutting force,

cutting force increases as tool size increases, since increasing rate of N_a dominates the decreasing rate of $F \cdot \Delta t$ when ultrasonic vibration frequency remains unchanged.

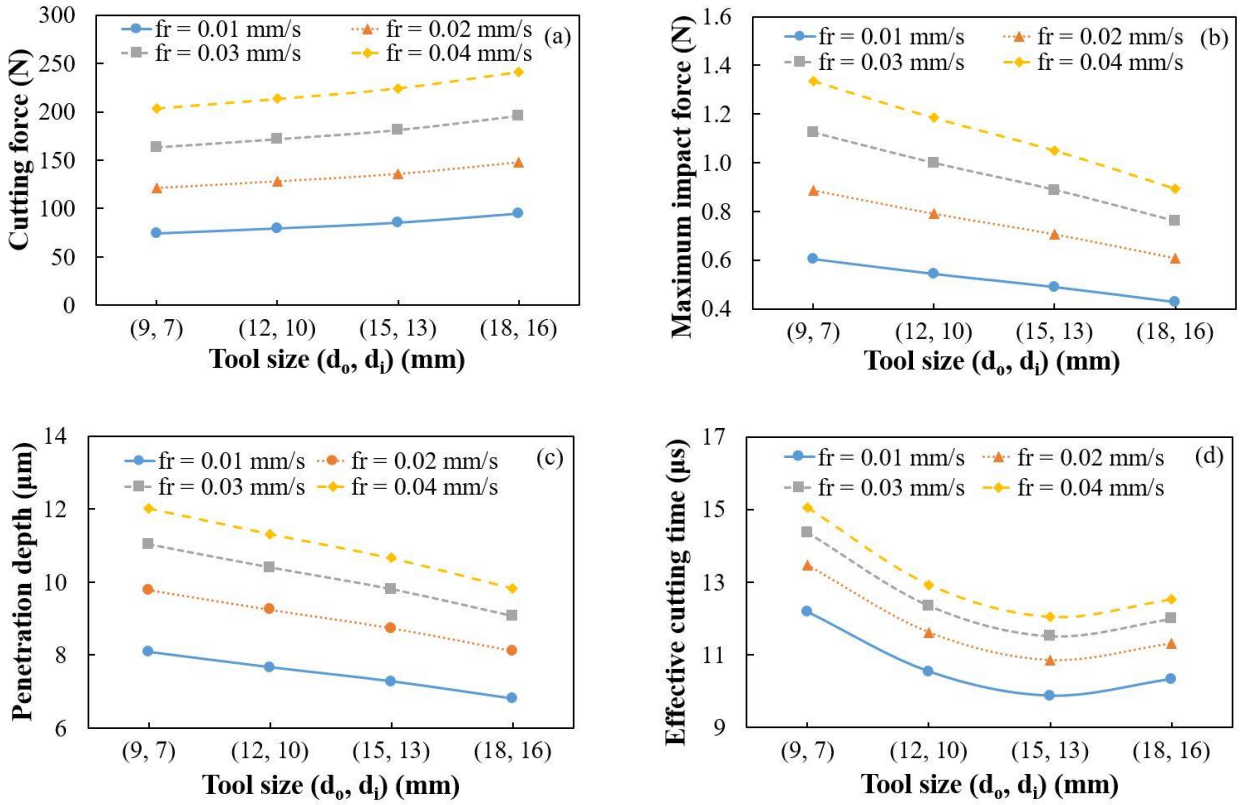

Figure 4.47 Influences of tool size on cutting force and intermediate variables

S = 3000 rpm, A (9,7) = 29 μm, A (12,10) = 36.27 μm, A (15,13) = 39.08 μm, A (18,16) = 33.48 μm, $S_1 - S_2$ = 100 – 120, C_a = 100, (d_o, d_i) = (12, 10) mm

Researchers have experienced that ultrasonic power supply goes overloaded especially when extreme machining conditions such as high feedrate are used. The overload indicates that the ultrasonic power supply doesn't have sufficient power to generate ultrasonic vibration at those conditions. The theoretical reason for this can be derived based on Equation (8), which describes the relationship between effective cutting time, Δt, ultrasonic vibration amplitude, A, and penetration depth, z_0. Effective cutting time is always greater than zero. Therefore, $\Delta t > 0$ has to be satisfied. Based on $\Delta t > 0$, $\frac{z_0}{A} > 0$ can be derived from Equation (8). Considering the

$\sin^{-1}\left(1-\frac{z_0}{A}\right)$ term in Equation (8) and Equation (12), $0 \le \left(\frac{F_i}{2A^2 H_v \tan\beta\sqrt{2+\tan^2\beta}}\right)^{1/2} \le 2$ can be derived. This inequality provides the theoretical explanation for overloading of ultrasonic power supply by not satisfying the inequality, $0 \le F_i \le 8A^4 H^2{}_v (2+\tan^2\beta)\tan^2\beta$.

4.3.5 Pilot experimental verification

A group of ten experiments were conducted to verify the mechanistic cutting force model. The same experimental setup and conditions shown in Table 4.11 were used for the model verification. Experiments were performed by using Tool No. 3 and varying each machining variable on four levels while keeping other variables fixed. The experimental and predicted cutting force values are compared in Figure 4.48. It can be seen that the trends of the predicted influences of the input variables (tool rotation speed, feedrate, and ultrasonic vibration amplitude) on cutting force agreed well with the trends experimentally obtained. The average difference between the predicted and measured cutting force values was 11.18%.

Table 4.11 Experimental conditions for model verification

Input variable	Unit	Levels
Ultrasonic vibration amplitude	μm	29.4; 32.84; 36.27; 39.71
Tool rotation speed	rpm	2000, 2500, 3000, 3500
Feedrate	mm/s	0.005; 0.015; 0.025; 0.035

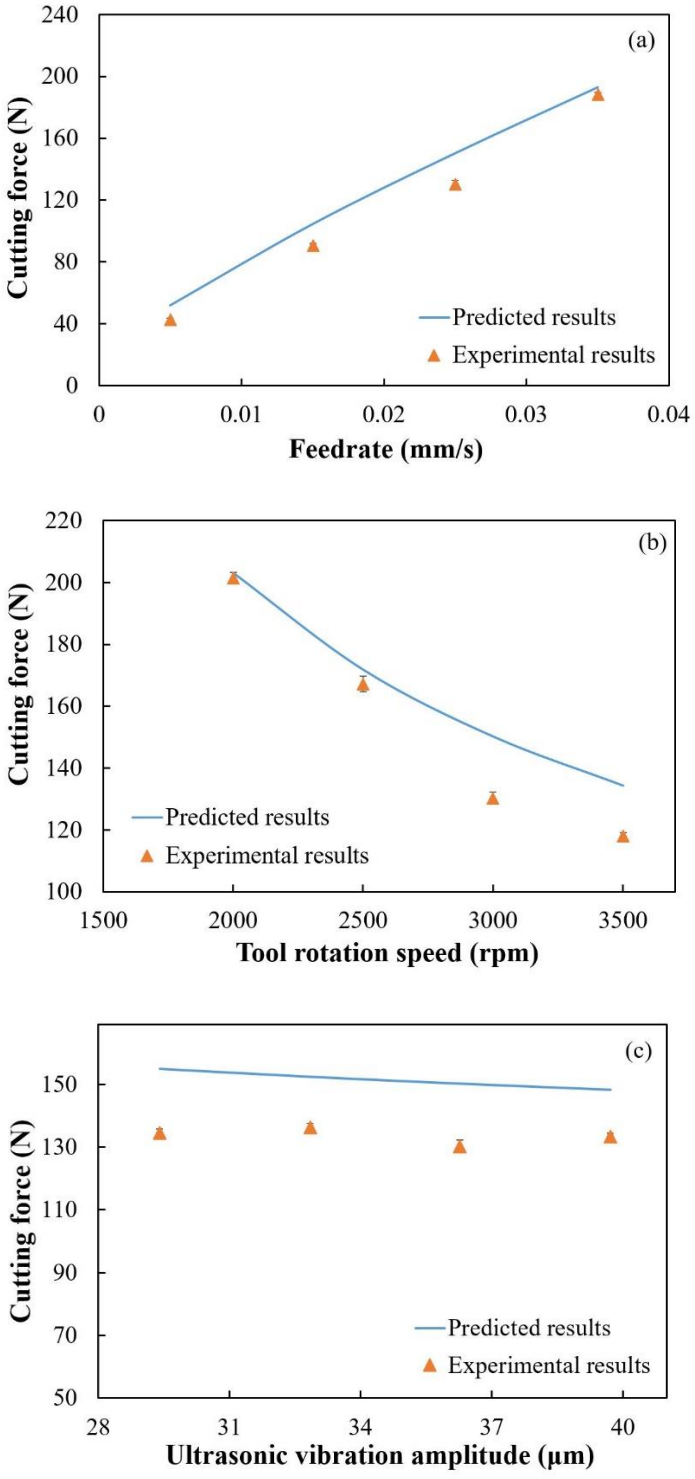

Figure 4.48 Comparison of predicted and experimental cutting force values

4.3.6 Concluding remarks

A physics-based mechanistic model to predict the cutting force for RUM of rocks has been developed considering the ductile mode and brittle fracture mode removal of rock under the indentation of a single abrasive particle and input variables. Rock material removal mechanisms were analyzed by using nano-dynamic mechanical analysis and microscopic imaging.

Preliminary experimental investigations were carried out to obtain the proportionality parameter and it was verified that the parameter is a constant over the range of input variables. The model has been used to investigate the effects of input variables on cutting force and intermediate variables. The predicted relationships between cutting force and input variables were explained by considering the intermediate variables for one abrasive particle. The trends predicted by the model are consistent with those obtained by the pilot validation experiments. The trends are (1) cutting force increases as feedrate, mesh size, abrasive concentration, and tool size increase (2) cutting force decreases as tool rotation speed and ultrasonic vibration amplitude increase.

Cutting force is also affected by the cutting temperature, friction between tool and workpiece, tool wear, the heterogeneity of rock materials, *etc*. This cutting force model can serve as a foundation to develop more sophisticated models for RUM of rocks.

Acknowledgment

The authors would like to thank Dr. Christopher Jones (Department of Civil Engineering at Kansas State University) for his assistance with nano-dynamic mechanical analysis.

References

[1]. Bruno, M.S., 2005, "Fundamental research on percussion drilling: Improved rock mechanics analysis, advanced simulation technology, and full-scale laboratory investigations," Report for the Department of Energy.

[2]. Garry, J.R.C., Wright, I.P., 2004, "Coring experiments with cryogenic water and carbon dioxide ices-toward planetary surface operation," Planetary and Space Science, Vol. 5, pp. 823–831.

[3]. Stoker, C.R., Cannon, H.N., Dunagen, S.E., et al., 2008, "The 2005 MARTE robotic drilling experiment in Rio Tinto, Spain: objectives, approach, and results of a simulated mission to search for life in the Martian subsurface," Astrobiology, Vol. 8, pp. 921–945.

[4]. Beste, U., 2004 "On the nature of cemented carbide wear in rock drilling," PhD Thesis, Uppsala University, Sweden.

[5]. Beste, U., Hartzell, T., Engqvist, H., et al., 2001, "Surface damage on cemented carbide rock-drill buttons," Wear, Vol. 249, pp. 324–329.

[6]. Hawk, J.A., Wilson, R.D., in: Modern Tribology Handbook, New York, 2001, pp. 1331–1370.

[7]. Tibbitts, G.A., Tek, T., Long, R.C., et al., 2002, "World's first benchmarking of drilling mud hammer performance at depth conditions," IADC/SPE Drilling Conference, Dallas, Texas, paper no. IADC/SPE 74540.

[8]. Tang, J., Lu, Y., Ge, Z., et al., 2014, "A new method of combined rock drilling," International Journal of Mining Science and Technology, Vol. 24, pp. 1–6.

[9]. Lu, Y., Tang, J., Ge, Z., et al., 2013, “Hard rock drilling technique with abrasive water jet assistance,” International Journal of Rock Mechanics and Mining Sciences, Vol. 60, pp. 47–56.

[10]. Clydesdale, G., Leseultre ,A., Lamine, E., 1994, “Low invasion corehead reduces mud invasion while improving performances,” Oil Gas Journal, Vol 1994; 92: 51–57.

[11]. Zacny, K., Bar-Cohen, Y., Brennan, M., et al., 2008, “Drilling Systems for Extraterrestrial Subsurface Exploration,” Astrobiology, Vol. 8, pp. 665–706.

[12]. Beaty, D., Miller, S., Zimmerman, W., et al., 2004, “Planning for a Mars in-situ sample preparation and distribution (SPAD) system,” Planetary Space Sci, Vol. 52, pp. 55–66.

[13]. Zacny, K., Cooper, G., 2006, “Considerations, constraints and strategies for drilling on Mars,” Planetary Space Sci, Vol. 54, pp. 345–356.

[14]. Tang, J., Quan, Q., Jiang, S., et al., 2017, “A soil flowing characteristics monitoring method in planetary drilling and coring verification experiments,” Advanced Space Research, Vol. 59, pp. 1341–1352.

[15]. Bar-Cohen, Y., Sherrit, S., Dolgin, B., et al., 2000, “Ultrasonic/sonic drilling/coring (USDC) for in-situ planetary applications,” Proceedings of the SPIE Smart Structures Conference, Newport Beach, CA, Paper No. 101.

[16]. Prabhakar, D., 1992, “Machining advanced ceramic materials using rotary ultrasonic machining process,” University of Illinois at Urbana-Champaign, IL, M.S. Thesis.

[17]. Hu, P., Zhang, J.M., Pei, Z.J., Treadwell, C., 2002, “Modeling of material removal rate in rotary ultrasonic machining: designed experiments,” Journal of Materials Processing Technology, Vol. 129, pp. 339-344.

[18]. Li, Z.C., Jiao, Y., Deines, T.W., Pei, J.J., Treadwell, C., 2005, “Rotary ultrasonic machining of ceramic matrix composites: feasibility study and design experiments,” International Journal of Machine Tools and Manufacture, Vol. 45, pp. 1402-1411.

[19]. Jiao, Y., Ping, H., Pei, Z.J., Treadwell, C., 2005, “Rotary ultrasonic machining of ceramics: design of experiments,” International Journal of Manufacturing Technology and Management, Vol. 7, pp. 192-206.

[20]. Stone Source Inc. Technical performance specs. Report. 10 October 2012. NY, USA.

[21]. Hood, M., 1976, “Cutting strong rock with a drag bit assisted by high-pressure water jets,” International Journal of Rock Mechanics and Mining Sciences and Geomechanics, Vol. 14, pp. 79–90.

[22]. Cong, W., Feng, Q., Pei, Z.J., et al., 2011, “Rotary ultrasonic machining of carbon fiber-reinforced plastic composites: using cutting fluid vs. cold air as coolant,” Journal of Composite Materials, Vol. 46, pp. 1745–1753.

[23]. Zhang, C., Feng, P., Pei, Z., Cong, W., 2014, "Rotary ultrasonic machining of sapphire: feasibility study and designed experiments," Key Engineering Materials, Vol. 589-590, pp. 523-528.

[24]. Fenn, O., 1987, “The use of water jets to assist free-rolling cutters in the excavation of hard rock,” International Journal of Rock Mechanics and Mining Sciences and Geomechanics, Vol. 87, pp. 137–147.

[25]. Churi, N.J., Pei, Z.J., Shorter, C.J., Treadwell, C., 2009, “Rotary ultrasonic machining of dental ceramics,” International Journal of Machining and Machinability of Materials, Vol. 6, pp. 270-284.

[26]. Cong, W.L., Pei, Z.J., Deines, T., Wang, Q.G., Treadwell, C., 2010, “Rotary ultrasonic machining of stainless steels: empirical study of machining variables,” International Journal of Manufacturing Research, Vol. 5, pp. 370-386.

[27]. Cong, W.L., Pei, Z.J., Sun, X., Zhang, C.L., 2014, "Rotary ultrasonic machining of CFRP: A mechanistic predictive model for cutting force," Ultrasonics, Vol. 54, pp. 663-675.

[28]. Jie, D., Li, P., Quan, Q., et al., 2013, “Optimization of percussive mechanism in rotary-percussion drill for lunar exploration,” IEEE International Conference on Robotics and Biomimetics, Shenzhen, China, pp. 2130–2135.

[29]. McGregor, K., 1967, “The drilling of rock,” A Maclaren Company, London.

[30]. Beste, U., Jacobson, S., 2008, “A new view of the deterioration and wear of WC-C_0 cemented carbide rock drill buttons,” Wear, Vol. 264, pp. 1129 – 1141.

[31]. Clydesdale, G., Leseultre, A., Lamine, E., 1994, “Core bit design reduces mud invasion, improves ROP,” Oil and Gas Journal, Vol. 92, pp. 51 – 57.

[32]. Beste, U., Jacobson, S., Hogmark, S., 2008, “Rock penetration into cemented carbide drill buttons during rock drilling,” Wear, Vol. 264, pp. 1142 – 1151.

[33]. Yang, X., Li, X., Lu, Y., 2011, “Wear characteristics of the cemented carbide blades in drilling limestone with water jet,” International Journal of Refractory Metals and Hard Materials, Vol. 29, pp. 320 – 325.

[34]. Miller, D., Ball, A., 1991, “The wear of diamonds in impregnated diamond bit drilling,” Wear,Vol. 141, pp. 311-320.

[35]. Yao, Q., Zhang, L. C., Bao, R., Lunn, J., Melmeth, C., 2010, “Edge chipping of rock: an experimental study,” Key Engineering Materials, Vol. 443, pp. 456-461.

[36]. Beste, U., Tribological aspects of rock and drill in rock drilling, Licentiate thesis, UPTEC 02 005, Department of Materials Science, Uppsala University, 2002.

[37]. Chao, G., Juntang, Y., 2011, “Efficient drilling of holes in Al2O3 armor ceramic using impregnated diamond bits,” Journal of Material Processing Technology, Vol. 211, pp. 1719 – 1728.

[38]. Miller, D., Ball, A., 1990, “Rock drilling with impregnated diamond microbits—An experimental study,” International Journal of Rock Mechanics and Mining Sciences and Geomechanics, Vol. 27, pp. 363 – 371.

[39]. Huang, S. L., Wang, Z. W., 1997, “The mechanics of diamond core drilling of rocks,” International Journal of Rock Mechanics and Mining Science, Vol. 34, pp. 134.

[40]. Churi, N.J., Nikhi, J., 2007, "Rotary ultrasonic machining of silicon carbide: designed experiments," International Journal of Manufacturing Technology and Management, Vol. 12, Issue 1/2/3, pp. 284.

[41]. Feng, Q., Cong, W.L., Pei, Z.J., Ren, C.Z., 2012, "Rotary Ultrasonic Machining of Carbon Fiber-Reinforced Polymer: Feasibility Study," Machining Science and Technology, Vol. 16, pp. 380-398.

[42]. Wang, Q., Pei, Z.J., Gao, H., Churi, N.J., Kang, R., 2009, "Rotary ultrasonic machining of potassium Dihydrogen phosphate (KDL) crystal: an experimental investigation," International Journal of Mechatronics and Manufacturing Systems, Vol. 2, pp. 414-426.

[43]. Zhang, C., Feng, P., Zhang, J., Wu, Z., Yu, D., 2012, “Investigation into the rotary ultrasonic face milling of K9 glass with mechanism study of material removal,” International Journal of Manufacturing Technology and Management, Vol. 25, pp. 248-266.

[44]. Gu, W., Yao, Z., 2011, “Evaluation of surface cracking in micron and sub-micron scale scratch tests for optical glass BK7,” Journal of Mechanical Science and Technology, Vol. 25, pp. 1167-1174.

[45]. Sreejith, P.S., Ngoi, B.K.A., 2000, “Dry machining: Machining of the future,” Journal of Materials Processing Technology, Vol. 101, pp. 287-291.

[46]. Choi, H.Z., Lee, S.W., Jeong, H.D., 2011, “A comparison of the cooling effects of compressed cold air and coolant for cylindrical grinding with a CBN wheel,” Journal of Materials Processing Technology, Vol. 111, pp. 265-268.

[47]. Kim, S.W., Lee, D.W., Kang, M.C., Kim, J.S., 2001, “Evaluation of machinability by cutting environments in high-speed milling of difficult-to-cut materials,” Journal of Materials Processing Technology, Vol. 111, pp. 256-260.

[48]. Hong, S.Y, Ding, Y., Jeong, W., 2001, “Friction and cutting forces in cryogenic machining of Ti-6Al-4V,” International Journal of Machine Tools and Manufacture, Vol. 41, pp. 2271-2285.

[49]. Su, Y., He, N., Li, L., Iqbal, A., Xiao, M.H., Xu, S., Qiu, B.G., 2007, “Refrigerated cooling air cutting of difficult-to-cut materials,” International Journal of Machine Tools and Manufacturing, Vol. 47, pp. 927-933.

[50]. Zacny, K.A., Cooper, G.A., 2004, “Investigation of diamond-impregnated drill bit wear while drilling under earth and mars conditions,” Journal of Geophysical Research, Vol. 109.

[51]. Fernando, P.K.S.C., Zhang, M., Pei, Z., 2018, “Rotary ultrasonic machining of rocks: an experimental investigation,” Advances in Mechanical Engineering, Vol, 10, pp. 1-9.

[52]. Ng, S., Le, D., Tucker, S., Zhang, G., 1996, “Control of machining induced edge chipping on glass ceramics,” Proceedings of the 1996 ASME International Mechanical Engineering Congress and Exposition, Manufacturing Engineering Devision, MED(4), Atlanta, GA, USA, pp. 229-236.

[53]. Cao, Y. Q., 2001, “Failure analysis of exit edges in ceramic machining using finite element analysis,” Engineering Failure Analysis 8, Vol. 8, pp. 325-338.

[54]. Li, Z.C., Cai, L.W., Pei, Z.J., Treadwell, C., 2006, “Edge-chipping reduction in rotary ultrasonic machining of ceramics: finite element analysis and experimental verification,” International Journal of Machine Tools & Manufacture, Vol. 46, pp. 1469-1477.

[55]. Fernando, P., Zhang, M., Pei, Z., Cong, W., 2017, “Intermittent and Continuous Rotary Ultrasonic Machining of K9 Glass: An Experimental Investigation,” Journal of Manufacturing and Materials Processing, Vol. 1, pp. 20.

[56]. Ahamed, A.R., Asokan, P., Aravindan, S., Prakash, M.K., 2010, “Drilling of hybrid Al-5%SiC_p-5%B_4C_p metal matrix composites,” International Journal of Advanced Manufacturing Technology, Vol. 49, pp. 871-877.

[57]. Wiercigroch, M., Wojewoda, J., Krivtsov, A.M., 2005, “Dynamics of ultrasonic percussive drilling of hard rocks,” Journal of Sound and Vibration, Vol. 280, pp. 739-757.

[58]. Lu, Y., tang, J., Ge, Z., Xia, B., Liu, Y., 2013, “Hard rock drilling technique with abrasive water jet assistance,” International Journal of Rock Mechanics and Mining Sciences, Vol. 60, pp. 47 – 56.

[59]. Liu, D., Cong, W.L., Pei, Z.J., Tang, Y., 2012, “A cutting force model for rotary ultrasonic machining of brittle materials,” International Journal of Machine Tools and Manufacture, Vol. 52, pp. 77-84.

[60]. Qin, N., Pei, Z.J., Treadwell, C., Guo, D.M., 2009, "Physics-based predictive cutting force model in ultrasonic-vibration-assisted grinding for titanium drilling," Journal of Manufacturing Science and Engineering ASME, Vol. 131, pp. 41011-1-9.

[61]. Pei, Z.J., Prabhakar, D., Ferreira, P.M., 1993, "A mechanistic approach to the prediction of material removal rates in rotary ultrasonic machining," Journal of Manufacturing Science and Engineering ASME, Vol. 64, pp. 771-784.

[62]. Pei, Z.J., Ferreira, P.M., Haselkom, M., 1995, "Plastic flow in rotary ultrasonic machining of ceramics," Journal of Materials processing Technology, Vol. 48, 771-777.

[63]. Pei, Z.J., Ferreira, P.M., 1998, "Modeling of ductile-mode material removal in rotary ultrasonic machining," International Journal of Machine Tools and Manufacture, Vol. 38, pp. 1399-1418.

[64]. Zhang, Q.H., Wu, C.L., Sun, J.L., Jia, Z.X., 2000, "The mechanism of material removal in ultrasonic drilling of engineering ceramics," Proceedings of the Institution of Mechanical Engineers Part B, Journal of Engineering Manufacture, Vol. 214, pp. 805-810.

[65]. Ya, G., Qin, H.W., Yang, S.C., Xu, Y.W., 2002, "Analysis of the rotary ultrasonic machining mechanism," Journal of Materials Processing Technology, Vol. 129, pp. 182-185.

[66]. Chao, C.L., Chou, W.C., Chao, C.W., Chen, C.C., 2007, "Material removal mechanisms involved in rotary ultrasonic machining of brittle materials," Key Engineering Materials, Vol. 329, pp. 391-396.

[67]. Sarwade, A., 2010, Study of micro rotary ultrasonic machining," M. S. Thesis, University of Nebraska-Lincoln, NE.

[68]. Ning, F., Wang, H., Cong, W., Fernando, P.K.S.C., 2017, "A mechanistic ultrasonic vibration amplitude model during rotary ultrasonic machining of CFRP composites," Ultrasonics, Vol. 76, pp. 44-51.

[69]. Liu, W., Zhang, L., Fang, Q., Chen, J., 2019, "A predictive model of subsurface damage and material removal volume for grinding of brittle materials considering single grit micro-geometry," The International Journal of Advanced Manufacturing Technology, Vol. 102, pp. 2231-2243.

[70]. Giovanola, J. H., Finnie, I., 1980, "On the machining of glass," Journal of materials Science, Vol. 15, pp. 2508-2514.

[71]. Bifano, T. G., Dow, T. A., Scattergood, R. O., 1991, "Ductile-regime grinding: a new technology for machining brittle materials," Journal of Engineering for Industry, Vol. 113, pp. 184-189.

[72]. Chen, M., Zhao, Q., Dong, S., Li, D., 2005, "The critical conditions of brittle-ductile transition and the factors influencing the surface quality of brittle materials in ultra-precision grinding," Journal of Materials Processing Technology, Vol. 168, pp. 75-82.

[73]. Liu, K., Li, X. P., Liang, S. Y., 2007, "The mechanism of ductile chip formation in cutting of brittle materials," International Journal of advance manufacturing Technology, Vol. 33, pp. 875-884.

[74]. Xiao, G., Ren, M., TO, S., 2018, "A study of mechanics in brittle-ductile cutting mode transition," Micromachines, Vol. 9.

[75]. Arif, M., Xinquan, Z., Rahman, M., Kumar, S., 2013, "A predictive model of the critical undeformed chip thickness for ductile-brittle transition in nano-machining of brittle

materials," International Journal of Machine Tools and Manufacture," Vol. 64, pp. 114-122.

[76]. Zhu, D., Yan, S., Li, B., 2014, "Single-grit modeling and simulation of crack initiation and propagation in SiC grinding using maximum undeformed chip thickness," Computational Materials Science, Vol. 92, pp. 13-21.

[77]. Cheng, J., Wu, J., Gong, Y. D., Wen, X. L., Wen, Q., 2017, "Experimental study on the single grit interaction behavior and brittle-ductile transition of grinding with a diamond micro-grinding tool," International Advance Manufacturing Technology, Vol. 91, pp. 1209-1226.

[78]. Paul, B., Gangal, M.D., 1969, "Why compressive loads on drill bits produce tensile splitting in rock," SPE 2392. In: Proceedings 4th Conference on Drilling and Rock Mechanics, pp. 109-114.

[79]. Wang, S. Y., Sloan, S. W., Liu, H. Y., Tang, C. A., 2011, "Numerical simulation of the rock fragmentation process induced by two drill bits subjected to static and dynamic (impact) loading," Rock Mechanics and Rock Engineering, Vol. 44, pp. 317-332.

[80]. Koshy, P., Jain, V. K., Lal, G. K., 1993, "A model for the topography of diamond grinding wheels," Wear, Vol. 169, pp. 237-242.

[81]. Huo, F. W., Guo, D. M., Kang, R. K., Jin, Z. J., 2009, "Characteristics of the wheel surface topography in ultra-precision grinding of silicon wafers," Key Engineering Materials, Vols. 389-390, pp. 36-41.

[82]. Hwang, T. W., Evans, C. J., Malkin, S., 2000, "High speed grinding of silicon nitride with electroplated diamond wheel, Part 2: wheel topography and grinding mechanisms," Journal of manufacturing science and engineering, Vol. 122, pp. 42-50.

[83]. Shi, Z., Malkin, S., 2006, “Wear of electroplated CBN grinding wheels,” Journal of Manufacturing Science and Engineering, Vol. 128, pp. 110-118.

[84]. Aurich, J. C., Herzenstiel, P., Sudermann, H., Magg, T., 2008, “High-performance dry grinding using a grinding wheel with a defined grain pattern,” CIRP Annals – Manufacturing Technology, Vol. 57, pp. 357-362.

[85]. Li, C., Sun, L., Yang, S., Zhang, L., Wu, C., Jiang, Z., 2018, “Three-dimensional characterization and modeling of diamond,” International Journal of Mechanical Sciences, Vol. 144, pp. 553-563.

[86]. Li, Z., Zhang, F., Luo, X., Guo, X., Cai, Y., Chang, W., Sun, J., 2018, “A new grinding force model for micro grinding RB-SiC ceramic with grinding wheel topography as an input,” Micromachines, Vol. 9, pp. 368-385.

[87]. Simoes, M., Antunes, J. M., Fernandes, J. V., Sakharova, N. A., 2018, “Numerical simulation of the depth-sencing indentation test with Knoop indenter,” Metals, Vol. 8, pp. 885-899.

[88]. Lawn, B., 1975, “Indentation fracture: principles and applications,” Jornal of materials science, Vol. 10, pp. 1049-1081.

[89]. Lawn, B. R., Marshall, D. B., 1979, “Hardness, toughness, and brittleness: An Indentation Analysis,” Journal of the American Ceramic Society, Vol. 62, pp. 347-350.

[90]. Marshall, D. B., Lawn, B. R., Evans, A. G., 1982, “Elastic/plastic indentation damage in ceramics: the lateral crack system,” Journal of American Ceramic Society, Vol. 65, pp. 561-566.

[91]. Brandon, J. R., 1974, “Rock mechanics properties of typical foundation rock types,” Earth Sciences Branch, Division of General Research, Engineering and Research center, Denver, Colorado, USA.

[92]. Nejati, H., Hassani, F., Radziszewski, P., 2012, “Experimental Investigation of Fracture Toughness Reduction and Fracture Development in Basalt Specimens under Microwave Illumination,” Earth and Space 2012: Engineering, Science, Construction, and Operations in Challenging Environments, pp. 325-334.

[93]. Zhang, C., Zhang, J., Feng, P., 2013, “Mathematical model for cutting force in rotary ultrasonic face milling of brittle materials,” International Journal of Advanced Manufacturing Technology, Vol. 69, pp. 161-170.

Chapter 5 - Investigations on ultrasonic vibration amplitude

5.1 Effects of tool natural frequency on ultrasonic vibration amplitude

Paper title:

Rotary Ultrasonic Machining: Effects of Tool Natural Frequency on Ultrasonic Vibration Amplitude

Published in:

Submitted to Machining Science and Technology

Authors' names:

Fernando, P.[1], Zhang, M.[1], Pei, Z.J.[2],

Authors' affiliations:

5. Department of Industrial and Manufacturing Systems Engineering, Kansas State University, Manhattan, KS 66506, USA
6. Department of Industrial and Systems Engineering, Texas A & M University, College Station, TX 77843 USA

5.1.1 Introduction

Grinding is an essential machining process for the manufacturing industry to produce quality products with high dimensional accuracy and low surface roughness (Chandra et al., 2016; Li et al., 2018). Recently, many investigations have been carried out to study tool wear, grinding burn, material removal behavior, and surface integrity in grinding of difficult-to-machine materials (Chandra et al., 2016; Li et al., 2018; Dai et al., 2018; Liu and Wang, 2018). Several nontraditional machining processes have also been utilized to machine conventionally difficult-to-machine materials; ultrasonic machining (USM) and rotary ultrasonic machining (RUM) are two of the processes.

Rotary ultrasonic machining has been used to conduct hole-making, surface grinding, and micro-machining on a wide range of brittle, ductile, and composite materials including silicon carbide, ceramics, stainless steel, carbon fiber reinforced plastics, potassium dihydrogen phosphate, rocks, etc. (Churi and Nikhi, 2007; Churi et al., 2009; Cong et al., 2010; Feng et al., 2012; Jiao and Ping, 2005; Wang et al., 2009; Wang et al., 2016; Fernando et al., 2018; Jain and Pandey, 2016). RUM is a hybrid machining process that combines the material removal mechanisms of grinding and ultrasonic machining. In RUM, a rotating tool with metal-bonded abrasive particles vibrates at an ultrasonic frequency (e.g., 20 kHz) in the axial direction and is fed towards the workpiece at a constant feed rate to remove material. Figure 1.1 shows a schematic of RUM. Coolant is pumped through the core of the tool to the cutting interface to flush away the removed material, keep the tool cool, and prevent the tool from jamming.

Cutting force is a critical output variable when machining difficult-to-machine materials; as the tool, machine, spindle, and workpiece can be damaged by a high cutting force (Jiao and Ping, 2005). RUM provides a lower cutting force compared to that of conventional hole-making

processes, as well as many other advantages (Jiao and Ping, 2005). The material removal rate (MRR) of RUM is 6-10 times higher than that of a conventional grinding under similar conditions, and RUM is about 10 times faster than ultrasonic machining (USM) or abrasive machining (Cleave, 1976; Treadwell and Pei, 2003). RUM can drill small and deep holes with a high hole accuracy, low cutting force, low machining temperature, low surface roughness, and long tool life (Cleave, 1976; Hu et al., 2002; Jiao and Ping, 2005; Li, et al., 2005; Lv et al., 2013).

There have been a few studies presenting measurement methods of ultrasonic vibration amplitude (Jain and Pandey, 2016; Cong and Pei, 2011). However, studies on the ultrasonic vibration amplitude of different tools are very limited. Cong and Pei (2011) reported another measurement method of ultrasonic vibration amplitude by observing the microscopic image of a machined workpiece surface (Cong and Pei, 2011).

In RUM, the employment of ultrasonic vibration is the main reason for the advantages mentioned above. In the literature, ultrasonic vibration amplitude in RUM is not studied comprehensively.

Cong and Pei (2011) posited that different tools had different vibration amplitudes on the same ultrasonic power level and this observation stayed consistent on every ultrasonic power level tested (Cong and Pei, 2011). No answer has been seen in the literature to explain this observation. As a result, some reported relationships between input variables (tool rotation speed, feed rate, ultrasonic power, abrasive concentration, abrasive particle size, tool geometry, etc.) and output variables (cutting force, torque, surface roughness, etc.) can be difficult to explain when different tools are used. It also presents an obstacle in establishing more realistic physics-based models in RUM. The objectives of this research are to understand the effects of tool natural frequency on ultrasonic vibration amplitude in RUM, to provide an explanation to the observation and

verification of measurement methods, and also to guide tool design and selection in RUM.

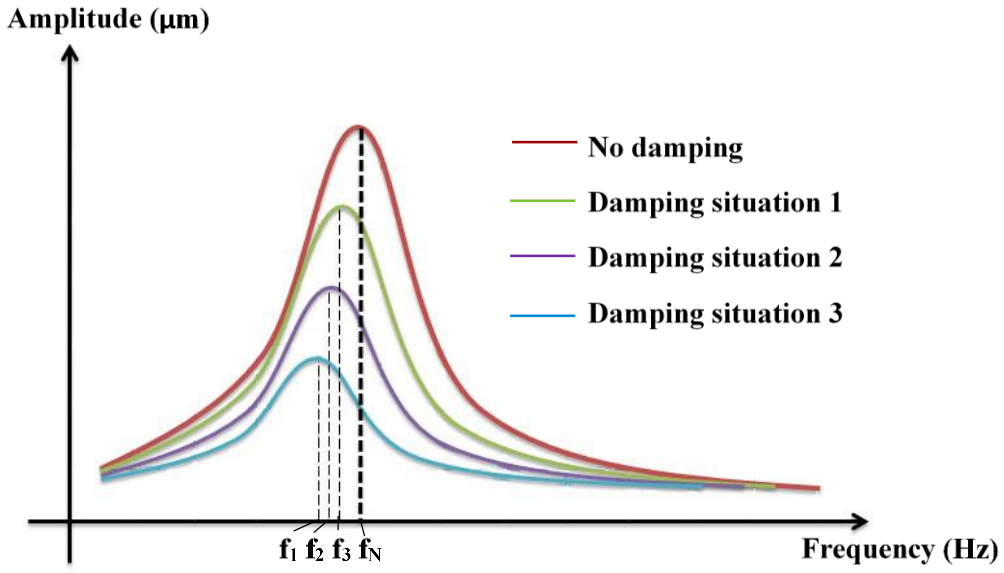

Figure 5.1 The relationship between amplitude and frequency of a forced vibration [after 14]

Vivekananda et al. (2014) designed and analyzed an ultrasonic vibratory tool using finite element analysis and performed an experimental study on ultrasonic vibration-assisted turning (Vivekananda et al., 2014). Using the designed tool, they calculated the natural frequency of the tool to be 19925.5 Hz. This number was very close to 20 kHz, which was the input frequency to the tool from the ultrasonic power supply. This closeness introduced resonance, which occurs when the object is forced to vibrate at its natural frequency. If the object's damping is negligible, the maximum vibration amplitude can be observed in case of resonance. Figure 5.1 shows the relationship between the amplitude and frequency of a forced vibration. Different curves represent different damping situations. It clearly shows that, when damping is present the highest vibration amplitude occurs before the natural frequency (f_N) of an object; when damping is negligible the maximum vibration amplitude occurs at the natural frequency of the object. In this study, the ultrasonic vibration in RUM is considered equivalent to a non-damping situation since as observed

experimentally ultrasonic vibration amplitude stays approximately constant for a given tool on a particular ultrasonic power level without showing damping effects. Finite element analysis simulation is used to find out the natural frequencies of five RUM tools. The effects of tool natural frequency on ultrasonic vibration amplitude are studied. The ultrasonic vibration amplitudes are measured by three methods and a comparison among the measurement methods is also made.

5.1.2 Experimental and measurement procedures

5.1.2.1 Experimental setup and conditions

The experiments are conducted on a rotary ultrasonic machine (Series 10, Sonic-Mill, Albuquerque, New Mexico, USA). Figure 2.1 shows a diagram of the experimental setup, which consists of an ultrasonic spindle system, an air-charged hydraulic feeding system, a coolant system, and a data acquisition system. The ultrasonic spindle system is comprised of an ultrasonic spindle, a power supply, an electric motor, and a control panel. The power supply converts the low frequency (60 Hz) electrical power into a high frequency (20 kHz) AC output that is then converted into mechanical vibrations by the piezoelectric transducer in the ultrasonic spindle. The air-charged hydraulic feeding system includes an actuator, an oil reservoir, a pressure gauge, an oil filter, a pressure regulator, a valve, and a compressor. The coolant system is comprised of a pump, a coolant tank, a pressure regulator, flow rate and pressure gauges, and valves. This system provides coolant to the spindle and machining interface. Data acquisition system consists of a dynamometer, an amplifier, a data acquisition device installed in a computer, and a software to collect data.

5.1.2.2 Tools and workpiece materials

Figure 5.2 shows the five different tools (NBR Diamond Tool Corp., LaGrangeville, NY, USA) used in this study with their specifications listed in Table 5.1. The natural frequencies of the tools are found out by using finite element analysis simulation. Solidworks (Dassault Systems Solidworks Corp. Waltham, MA, USA) is used to create three-dimensional models and analyze the natural frequencies of the tools. A ten-node parabolic (quadratic) 3D solid element is selected to create the mesh for each tool analysis. The size of the mesh is selected to maintain two layers of mesh across the thickness of the cylindrical wall of a tool as shown in Figure 5.3. The top part of the tool is constrained from moving along the X, Y, and Z directions as it is fixed into the tool holder of the ultrasonic spindle.

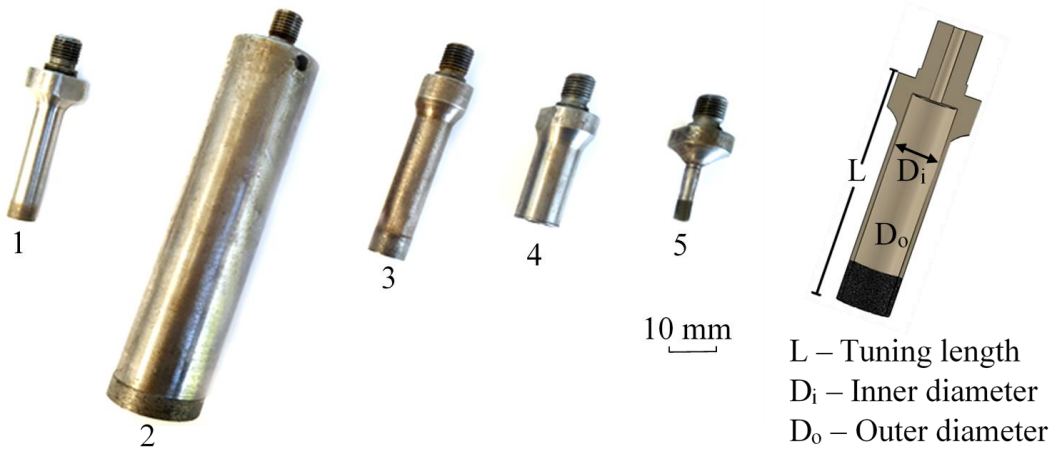

Figure 5.2 Tools used in the RUM experiments

The workpiece used in this study is a titanium alloy (Ti-6Al-4V) plate. Titanium alloy is selected because the machining marks on the surface of the rod cored from each hole drilled on ductile materials (such as titanium alloy) can be seen clearly under a microscope. It is very difficult to observe machining marks on brittle materials like ceramics, glass, or rocks [6]. With titanium alloy as the workpiece, a previously reported measurement method of ultrasonic amplitude in

RUM can be implemented [6]. The dimensions of the workpiece are 15 mm × 15 mm × 10 mm. Selected physical and mechanical properties of the workpiece material are listed in Table 5.2.

Table 5.1 Tool specifications

Tool No.	Natural frequency (Hz)	Outer diameter (mm)	Inner diameter (mm)	Tuning length (mm)	Weight (g)
1	28715	8.93	7.09	50.33	28.39
2	8893	28.61	25.05	120.47	125.48
3	22637	12.69	10.12	61.15	36.8
4	33040	14.03	12.59	38.03	29.31
5	61649	4.68	2.98	29.93	22.25

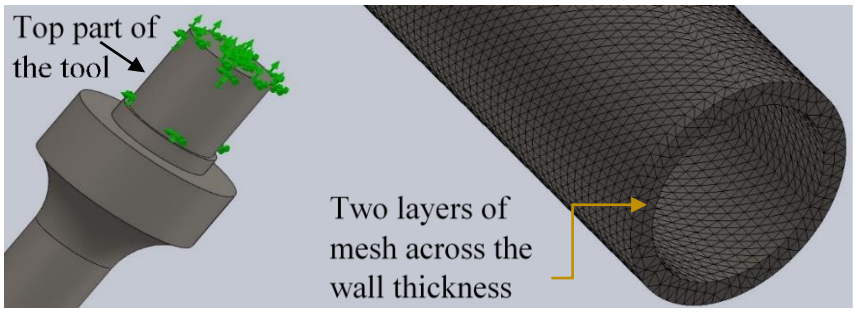

Figure 5.3 Application of mesh and constraints in finite element analysis

Table 5.2 Physical and mechanical properties of titanium alloy (Ti-6Al-4V)

Property	Unit	Value
Density	Kg/m^3	4510
Hardness (Rockwell)	HRC	36
Elastic modulus	GPa	113.8
Tensile strength	MPa	950
Melting point	^oC	1660

5.1.2.3 Measurement procedures

Ultrasonic vibration amplitudes are measured under two circumstances: (1) with RUM: when a workpiece is being machined and (2) without RUM: when the ultrasonic power is turned

on but no tool rotation or workpiece is engaged. Ultrasonic vibration amplitude measurements are taken on different ultrasonic power levels as shown in Table 5.3.

Table 5.3 Ultrasonic power levels and wattages

Ultrasonic power (%)	Ultrasonic power (W)
20	180
30	270
40	360
50	450
60	540
70	630
80	720
90	810
100	900

The workpiece is drilled by using metal-bonded diamond core tools as shown in Figure 5.2. The tools have an abrasive concentration of 100 and abrasives are in the size range of 0.106 – 0.120 mm. During all the experiments, tool rotation speed, feedrate, and coolant flow rate are kept constant at 4000 rpm, 0.01 mm/s, and 10 L/min, respectively. Only ultrasonic power is varied according to Table 5.3.

5.1.2.3.1 Ultrasonic amplitude with RUM

A microscopic imaging method [6] is used to measure the ultrasonic vibration amplitude with RUM. This method can also be used to estimate the ultrasonic vibration frequency during RUM. As illustrated in Figure 1.1, RUM is a core drilling technique and it produces a hole and cores a rod for every machined hole. Diamond abrasive particles are fixed on both the inside and outside of the tool wall; therefore, machining marks are left on both the hole and the rod surfaces. Theoretically, each machining mark is the trajectory of a single diamond abrasive particle against the machined surface. These machining marks are observed under a microscope (Olympus BX51,

Olympus Corporation, Tokyo, Japan). Figure 5.4 shows a microscopic image of the observed machining marks in a sinusoidal form.

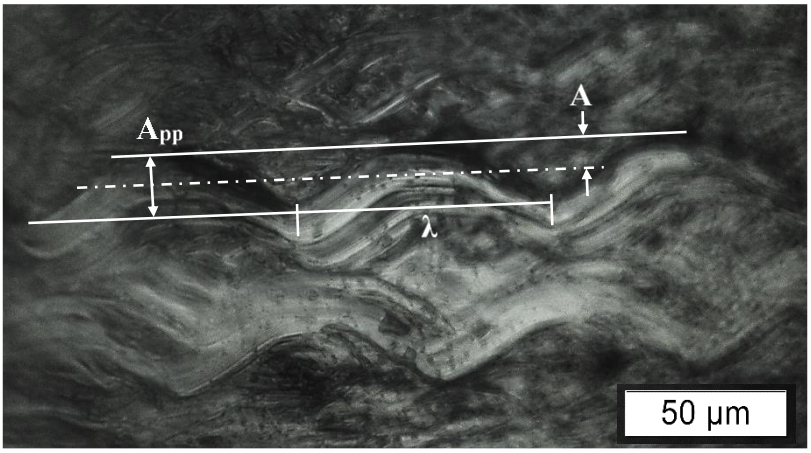

Figure 5.4 A microscopic image of machining marks on a titanium alloy workpiece machined by RUM

The ultrasonic vibration amplitude (A) and wave length (λ) are measured by using the measurement function in the image processing software. The following equation can be used to calculate the frequency of the ultrasonic vibration with RUM:

$$F = \frac{S\pi d}{60\lambda} \tag{1}$$

where S is the spindle speed in rpm, and d is the outer diameter of the tool. Three independent measurements are conducted for each experimental condition.

5.1.2.3.2 Ultrasonic vibration amplitude without RUM

In the industry, ultrasonic vibration amplitude is commonly measured with the dial gauge indicator method [6], which cannot measure the ultrasonic vibration amplitude during machining. A schematic of the dial gauge indicator method is shown in Figure 5.5. A universal magnetic base stand is used to fix the dial gauge indicator to the machine table. The plunger of the dial gauge

indicator is aligned so that the tip of the plunger touches the end plane of the tool. The initial reading of the dial gauge indicator is then recorded. The ultrasonic power is turned on and the corresponding reading of the dial gauge indicator is also recorded. The difference between the two readings is supposed to be the peak-to-peak amplitude of the ultrasonic vibration. In this study, the same procedure is used to obtain the ultrasonic vibration amplitudes of five tools on different ultrasonic power levels. Four measurements are taken at each quadrant of the end plane of a tool.

It is difficult to confirm whether the dial gauge indicator method gives peak-to-peak amplitude values or if it provides other values in the range of the peak-to-peak amplitude. Since the naked eye cannot see the high frequency of the ultrasonic vibration through the dial gauge indicator, a steady displacement is observed instead. Dial gauge indicators give accurate measurements up to about 120 counts per minute (cpm) (2 Hz) [1]. Beyond 120 cpm, it is difficult to obtain a precise reading due to the jump of the gauge plunger especially for ultrasonic vibration, which has 1200,000 cpm (20 kHz) [1]. Therefore, to eliminate the measurement error and to better compare the ultrasonic vibration amplitudes, a non-contact capacitive sensor method is used to obtain peak-to-peak ultrasonic vibration amplitudes.

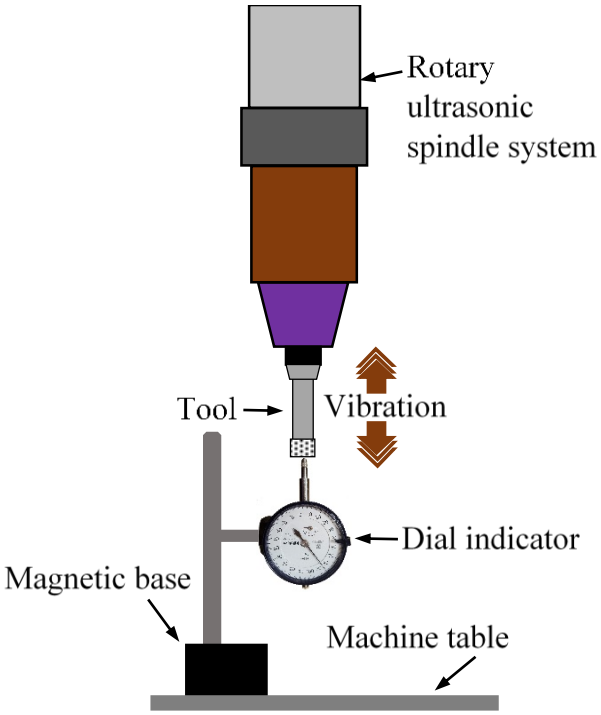

Figure 5.5 Measurement of ultrasonic vibration amplitude by using the dial gauge indicator method

Figure 5.6 illustrates the use of the high precision non-contact capacitive sensor (Elite Series CPL490, Lion Precision, St. Paul, Minnesota, USA) to measure the ultrasonic vibration amplitude without RUM. The capacitive sensor (probe) is fixed on the machine table by using a universal magnetic base stand. The capacitive sensor is aligned until the tip of the probe makes a gap of 25 µm to the end plane of the tool. Then the ultrasonic power is turned on and the corresponding voltage data of the ultrasonic vibration amplitude is recorded by using a data acquisition (DAQ) system (NI-PCIe 6320, National Instruments, Austin, Texas, USA). The capacitive sensor produces and feeds a high frequency voltage signal to the module. The module then converts that signal into a voltage (DC) between –10 V and 10 V. The output voltage of the module has a direct linear relationship with the changes in the gap between the probe and the end surface of the tool. The output voltage of the module then feeds into the DAQ. Corresponding voltage data is recorded

by using the National Instrument NI-max software with a fixed sample rate of 150k/second. The actual ultrasonic vibration amplitudes are calculated by using the sensitivity (0.400 V/μm) provided in the manufacturer's calibration report. Three measurements are conducted for each experimental condition.

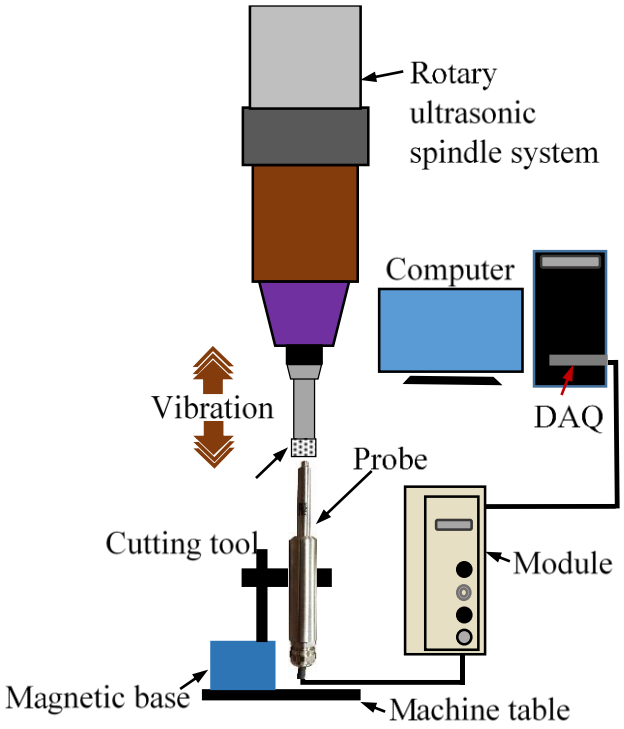

Figure 5.6 Measurement of ultrasonic vibration amplitude by using the capacitive sensor method

5.1.3 Experimental results

Table 5.4 lists the ultrasonic vibration amplitude results with and without RUM at different ultrasonic power levels. Ultrasonic vibration amplitude values are the means of at least three repeated measurements by each method. Ultrasonic vibration amplitudes without RUM of the five tools and the spindle (without tool installed) are measured using both the dial gauge indicator method and the capacitive sensor method. The ultrasonic vibration amplitudes with RUM of

Tool 1 on different ultrasonic power levels are measured by using the microscopic imaging method.

Table 5.4 Ultrasonic vibration amplitude (μm) at different ultrasonic power levels

	Tool No.	Ultrasonic power (%)								
		20	30	40	50	60	70	80	90	100
Without RUM (dial gauge indicator method)	1	6	7	8	9	10	11	12	13	14
	2	2	3	4	4	5	6	6	6	7
	3	12	15	17	20	22	24	26	27	28
	4	3	4	5	6	6	7	8	8	8
	5	3	3	3	4	4	5	5	5	6
	Spindle	1	1.5	2	2.5	2.5	3	3	4	4
Without RUM (capacitive sensor method)	1	15.6	19.1	21.7	24.8	27.4	31.0	32.1	34.1	36.1
	2	7.5	9.2	10.6	12.3	14.2	14.4	15.1	15.8	17.4
	3	27.4	33.7	39.4	41.0	42.1	49.3	52.5	53.2	53.9
	4	9.7	11.7	13.4	15.3	16.7	18.2	19.2	20.7	22.0
	5	7.8	9.6	11.0	13.2	14.0	14.7	15.5	16.7	17.8
	Spindle	5.3	6.6	7.4	8.5	9.2	10.1	10.6	11.4	12.3
With RUM (microscopic imaging method)	1	5.8	6.0	6.2	7.1	7.9	8.1	8.5	9.1	11.7

5.2.4 Discussions

5.2.4.1 Finite element analysis simulation of tool natural frequency

The amplitude of a forced harmonic motion strongly depends on the difference between the driving and the natural frequencies [8]. The amplitude becomes larger when the driving frequency is closer to the natural frequency. When the damping is small, the increase in amplitude when the tool natural frequency comes close to the driving frequency (the input ultrasonic frequency from the power supply, 20 kHz) is very large, which is known as resonance [8]. Natural modes of vibration are described in terms of its modal parameters: natural frequency, the modal

damping factor, and characteristic displacement pattern namely mode shape [9]. The natural frequency of the mode shape that vibrates along the axial direction of the tool is considered in this study, because RUM produces vibration along the tool axis.

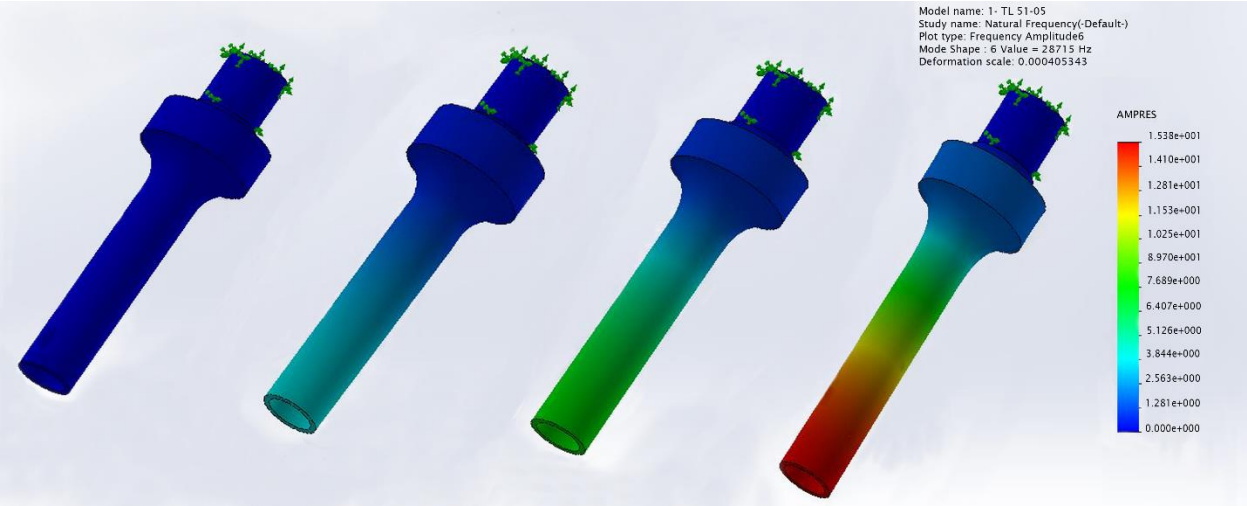

Figure 5.7 Mode shape and its deformation states of Tool 1

Figure 5.7 shows the selected mode shape for Tool 1 and the different deformation states in one cycle of the vibration. Amplitude along the Y axis (AMPY) in Figure 5.7 is a software-generated dimensionless value to compare the different amplitudes in a particular study. The natural frequencies of the other tools are found out in the same way.

5.1.4.2 Ultrasonic vibration amplitude

The ultrasonic vibration amplitudes (without RUM) measured by the dial gauge indicator method and the capacitive sensor method are shown in Figures 5.9 and 5.10, respectively. It is found by both measurement methods that Tool 3 produces the highest ultrasonic vibration amplitude among the five tools at every tested ultrasonic power level. Tool 3 also produces a roughly 4 times higher ultrasonic vibration amplitude than that of Tool 2 on the ultrasonic power level of 100%. Cong and Pei (2011) reported that different tools had different ultrasonic vibration

amplitudes for the same ultrasonic power level (30%) [6]. Cong et al.'s report agreed with the observation in this study for all the measurement methods at all the ultrasonic power levels [6]. In addition, both ultrasonic vibration amplitude measurement methods show that the spindle (without tool installed) produces a lower ultrasonic vibration amplitude than when a tool is installed.

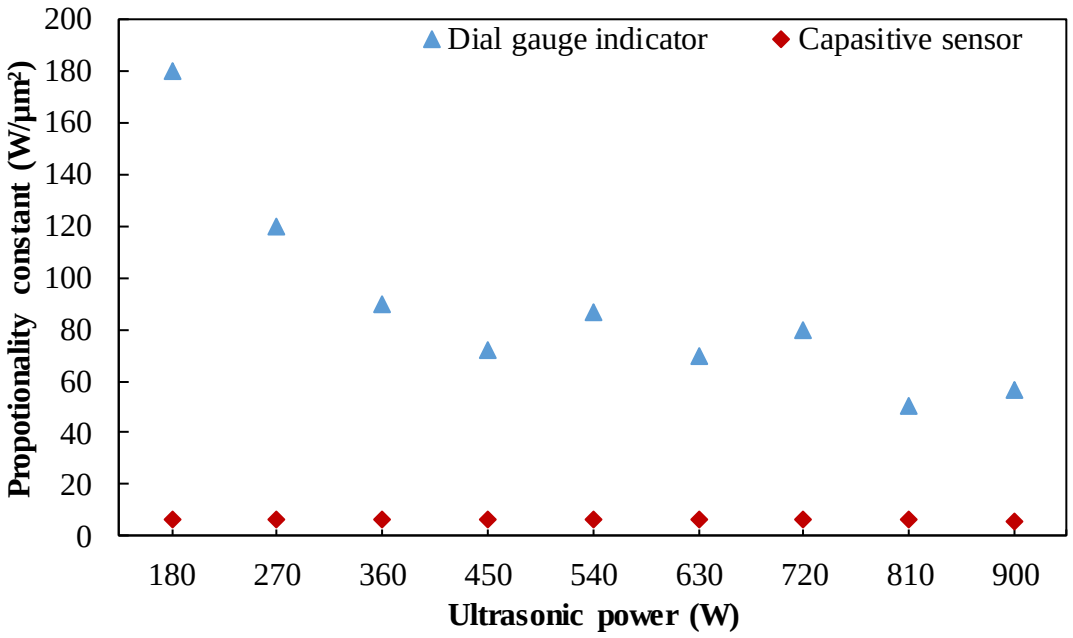

Figure 5.8 Proportional factor of power and ultrasonic vibration amplitude

Ultrasonic vibration amplitude (without RUM) obtained by the capacitive sensor method is more than twice that measured by the dial gauge indicator method. This difference is due to the error of the dial gauge indicator when used as a measurement instrument for a high frequency vibration amplitude. Weiss (1938) reported that when using a dial gauge indicator to measure a high frequency vibration amplitude, the jumping of the gauge plunger caused errors [21]. This error is known as a high frequency error as the gauge plunger cannot stay in contact with the vibrating object [21]. In this case, the dial gauge indicator measures a lower amplitude than the actual amplitude [21]. Thus, the dial gauge indicator is not a precise instrument to measure ultrasonic vibration amplitude. Figure 5.8 provides an observation illustrating such an error as the

amplitudes measured by the dial gauge indicator method do not satisfy the proportional relationship with ultrasonic power levels [17].

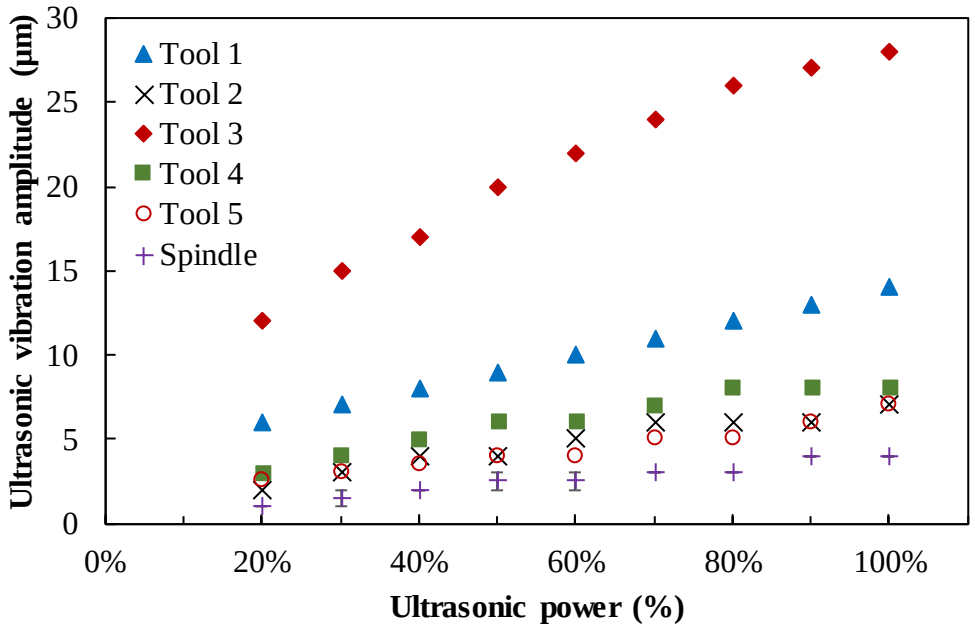

Figure 5.9 Ultrasonic vibration amplitudes measured by the dial gauge indicator method (without RUM)

The vertical displacement of Tool 1 and Tool 3 with time is shown in Figure 5.11 (a) and (b), respectively. It can be seen that the ultrasonic vibration has a sinusoidal vibration pattern versus time, resulting in a simple harmonic motion [8]. Furthermore, the frequency of the ultrasonic vibration is a constant 20 kHz on different ultrasonic power levels and stays constant for different tools. The ultrasonic vibration of tools forms a forced vibration; therefore, tool vibration frequency is the frequency of the input ultrasonic vibration [8].

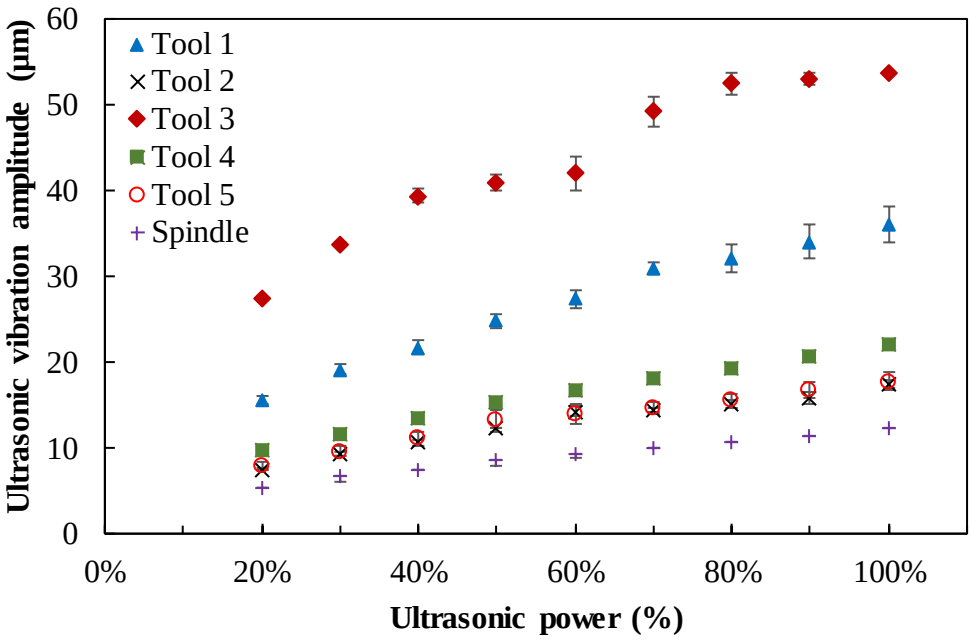

Figure 5.10 Ultrasonic vibration amplitudes measured by the capacitive sensor method (without RUM)

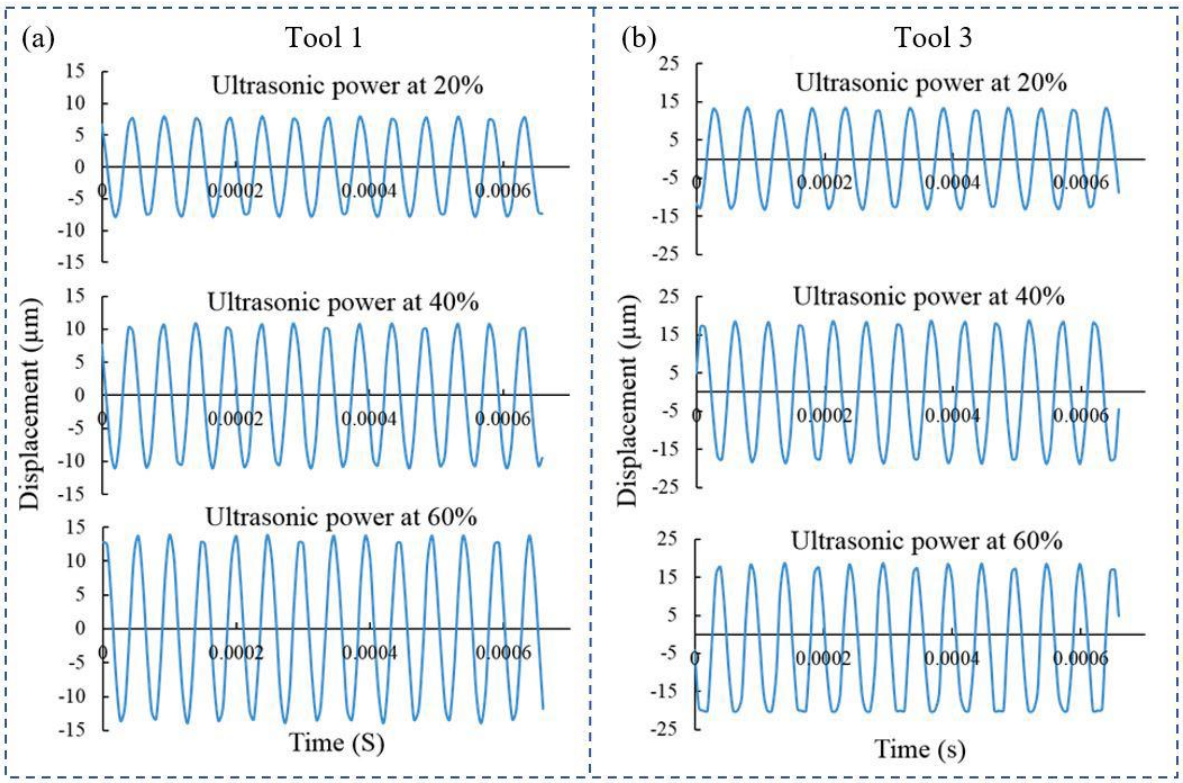

Figure 5.11 Tool displacement with time measured by the capacitive sensor method (without RUM)

Figure 5.12 compares the ultrasonic vibration amplitudes of Tool 1 with and without RUM on different ultrasonic power levels. It can be seen that the ultrasonic vibration amplitude with RUM is smaller than without RUM. Cong and Pei (2011) reported the same findings for five different tools on the ultrasonic power level of 30% [6].

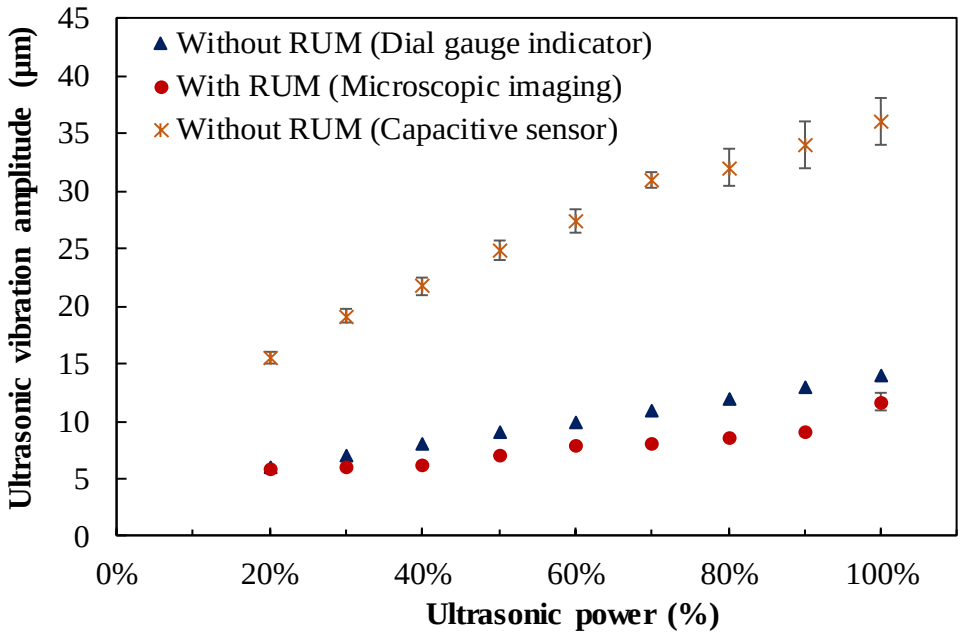

Figure 5.12 Ultrasonic vibration amplitudes with and without RUM of Tool 1

5.1.4.3 Effects of tool natural frequency on ultrasonic vibration amplitude

The effects of tool natural frequency on ultrasonic vibration amplitude measured by the dial gauge indicator method and the capacitive sensor method are compared in Figures 5.13 and 7.14.

The natural frequency of Tool 3 is 22,637 Hz, which is the closest one to the input ultrasonic frequency of 20 kHz among all five tools. Therefore, on every ultrasonic power level, Tool 3 has the highest ultrasonic vibration amplitude when measured by both methods. Tool 1 has the second-closest natural frequency to the input ultrasonic frequency of 20 kHz, and Tool 1 shows the second highest ultrasonic vibration amplitude on every ultrasonic power level. Tool 2 has

closer natural frequency to ultrasonic frequency compared to Tool 4. Even though, Tool 4 has higher ultrasonic vibration amplitude on every ultrasonic power level when measured by both methods. As shown in Figure 5.1, the relationship between amplitude and frequency of a forced vibration is different for the frequencies below the natural frequency compared to those above it. Therefore, two tools with their natural frequencies above or below the ultrasonic frequency cannot be compared without knowing the exact behavior of the relationship between amplitude and tool natural frequency of the ultrasonic vibration. However, in general, ultrasonic vibration amplitude decreases for all tested ultrasonic power levels as the natural frequency of the tool deviates further from 20 kHz. Unlike some other ultrasonic vibration-assisted process, where the input ultrasonic frequency can be tuned according to the natural frequency of a tool or a tool is made as a resonant vibration tool [13, 15], in this RUM system the input ultrasonic frequency is supplied at 20 kHz as a constant and to process holes of different diameters and depths, RUM tools of various sizes have to be chosen. These tools vary greatly in their natural frequencies as shown in Table 5.1.

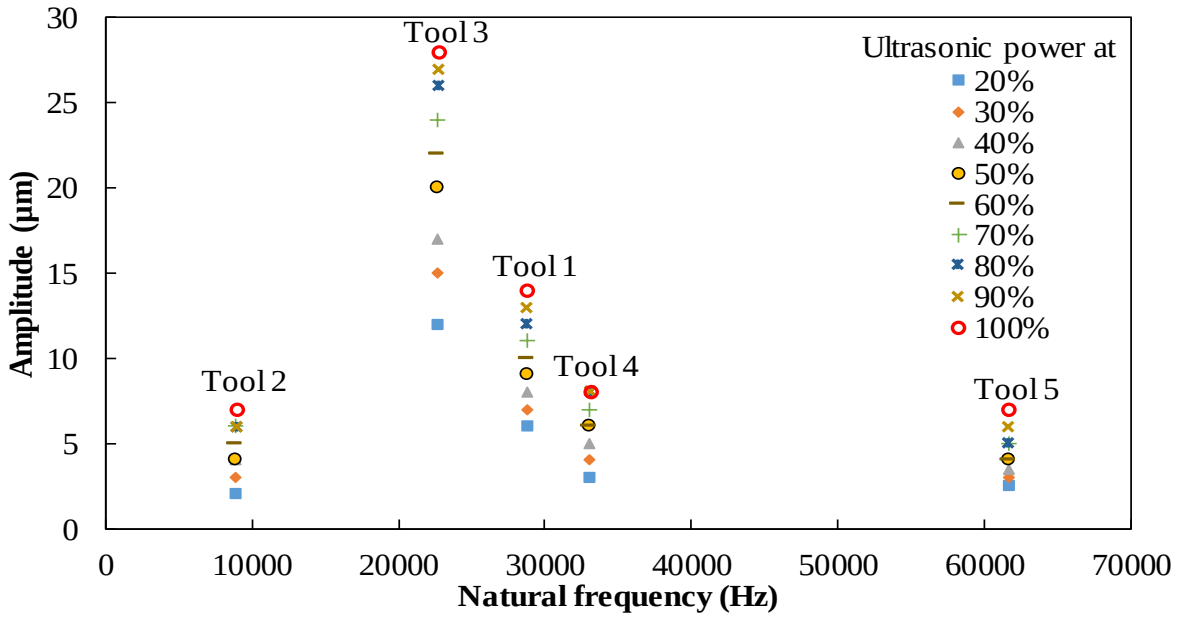

Figure 5.13 Effects of tool natural frequency on ultrasonic vibration amplitude measured by the dial gauge indicator method (without RUM)

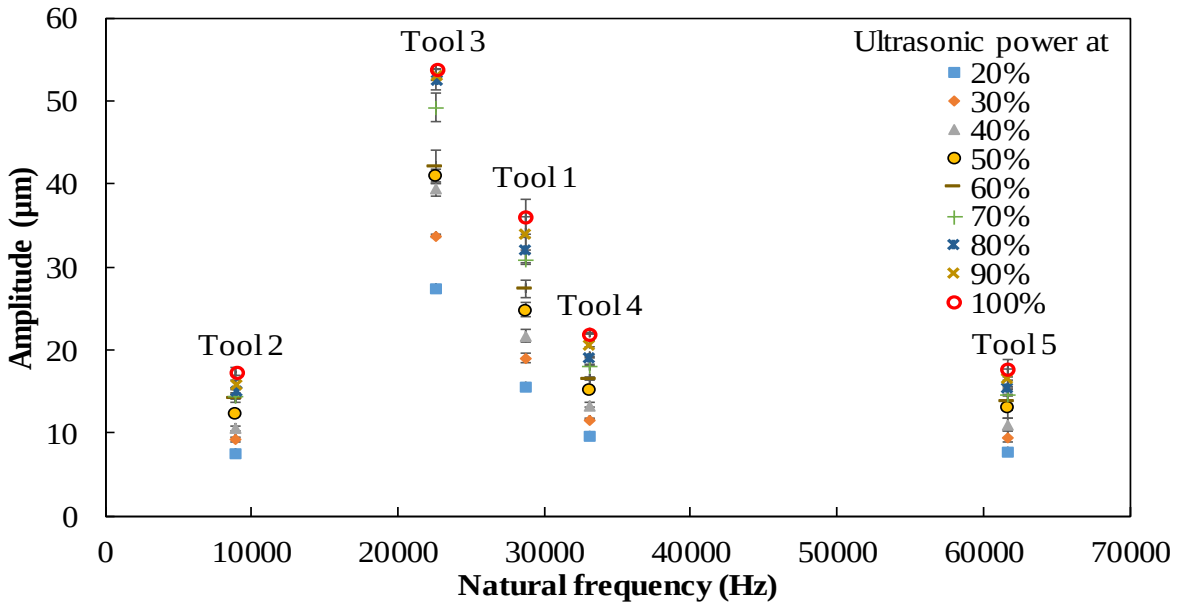

Figure 5.14 Effects of tool natural frequency on ultrasonic vibration amplitude measured by the capacitive sensor method (without RUM)

5.1.5 Concluding remarks

This study, for the first time, investigates the effects of tool natural frequency on ultrasonic vibration amplitudes in rotary ultrasonic machining to explain a reported observation that ultrasonic vibration amplitude differs by tools at the same ultrasonic power level. Natural frequencies of the tools are obtained by using finite element analysis simulation. Three ultrasonic vibration amplitude measurement methods (dial gauge indicator method, microscopic imaging method, and capacitive sensor method) are performed. The ultrasonic vibration amplitude measurements with different methods are compared and discussed. The conclusions drawn from this investigation are as follows:

1. The natural frequency of tool significantly affects the ultrasonic vibration amplitude in RUM.

2. The tool with a natural frequency closest to the input frequency (20 kHz) of the ultrasonic power supply generates the highest ultrasonic vibration amplitude on every ultrasonic power level.
3. Ultrasonic vibration amplitudes (without RUM) measure by the capacitive sensor method are higher than those measure by the dial gauge indicator method.
4. Ultrasonic vibration amplitudes (with RUM) measure by the microscopic imaging method are lower than the ultrasonic vibration amplitudes without RUM.

References

[1]. Chandra, A.; Bastawros, A.F.; Yu, T.Y. (2017) Chemical mechanical paired grinding: a tool for multi-wavelength planarization. International Journal of Advance Manufacturing Technology, 89:611-617.

[2]. Li, Z.; Ding, W.; Liu, C.; Su, H. (2018) Grinding performance and surface integrity of particulate-reinforced titanium matrix composites in creep-feed grinding. International Journal of Advance Manufacturing Technology, 94:3917-3928.

[3]. Dai, C.; Ding, W.; Zhu, Y.; Xu, J.; Yu, H. (2018) Grinding temperature and power consumption in high speed grinding of Inconel 718 nickel-based superalloy with a vitrified CBN wheel. Precision Engineering, 52:192-200.

[4]. Liu, X.; Wang, Z. (2018) Research on high-precision form grinding technology of gear based on ambient temperature adaptability. Mathematical Problems in Engineering, 11:1-13.

[5]. Churi, N.J.; Nikhi J. (2007) Rotary ultrasonic machining of silicon carbide: designed experiments. International Journal of Manufacturing Technology and Management, 12 (1/2/3):284.

[6]. Churi, N.J.; Pei, Z.J.; Shorter, D.C. (2009) Rotary ultrasonic machining of dental ceramics. International Journal of Machining and Machinability of Materials, 6:270-284.

[7]. Cong, W.L.; Pei, Z.J.; Deines, T. (2010) Rotary ultrasonic machining of stainless steels: empirical study of machining variables. International Journal of Manufacturing Research, 5:370-386.

[8]. Feng, Q.; Cong, W.L.; Pei, Z.J.; Ren, C.Z. (2012) Rotary ultrasonic machining of carbon fiber-reinforced polymer: feasibility study. Machining Science and Technology, 16:380-398.

[9]. Jiao, Y.; Ping, P.H. (2005) Rotary ultrasonic machining of ceramics: design of experiments. International Journal of Manufacturing Technology and Management, 7:192-206.

[10]. Wang, Q.; Pei, Z.J.; Gao, H.; Churi, N.J.; Kang, R. (2009) Rotary ultrasonic machining of potassium dihydrogen phosphate (KDL) crystal: an experimental investigation. International Journal of Mechatronics and Manufacturing Systems, 2:414-426.

[11]. Wang, H.; Ning, F.; Hu, Y. (2016) Surface grinding of carbon fiber–reinforced plastic composites using rotary ultrasonic machining: effects of tool variables. Advances in Mechanical Engineering, 8:1-14.

[12]. Fernando, P.; Zhang, M.; Pei, Z.J. (2018) Rotary ultrasonic machining of rocks: an experimental investigation. Advances in Mechanical Engineering, 10:1-9.

[13]. Jain, A.K.; Pandey, P.M. (2016) Experimental investigations of ceramic machining using μ-grinding and μ-rotary ultrasonic machining processes: a comparative study. Materials and Manufacturing Processes, 32:598-607.

[14]. Hu, P.; Zhang, J.M.; Pei, Z.J.; Treadwell, C. (2002) Modeling of material removal rate in rotary ultrasonic machining: designed experiments. Journal of Materials Processing Technology, 129:339-344.

[15]. Li, Z.C.; Jiao, Y.; Deines, T.W.; Pei, Z.J.; Treadwell, C. (2005) Rotary ultrasonic machining of ceramic matrix composites: feasibility study and design experiments. International Journal of Machine Tools and Manufacture, 45:1402-1411.

[16]. Cleave, D.V. (1976) Ultrasonics gets bigger jobs in machining and welding. Iron Age, 218:69-72.

[17]. Treadwell, C.; Pei, Z.J. (2003) Machining ceramics with rotary ultrasonic machining: rotary ultrasonic machining provides a fast, high-quality machining method for many ceramic and glass applications. Ceramic Industry, June, pp. 39-42.

[18]. Lv, D.; Huang, Y.; Wang, H.; Tang, Y.; Wu, X. (2013) Improvement effects of vibration on cutting force in rotary ultrasonic machining of BK7 glass. Journal of Material Processing Technology, 213:1548-1557.

[19]. Cong, W.L.; Pei, Z.J. (2011) Vibrational amplitude in rotary ultrasonic machining: a novel measurement method and effects of process variables. Journal of Manufacturing Science and Engineering, 133:34501.1-34501.5.

[20]. Srinivasan MR. Physics for engineers. 1st ed. New Delhi, India: New Age International; 2009.

[21]. Vivekananda, K.; Arka, G.N.; Sahoo, S.K. (2014) Design and analysis of ultrasonic vibratory tool (UVT) using FEM, and experimental study on ultrasonic vibration-assisted turning (UAT). Procedia Engineering, 97:1178-1186.

[22]. Cong, W.L.; Pei, Z.J.; Deines, T.W.; Liu, D.F.; Treadwell, C. (2013) Rotary ultrasonic machining of CFRP/Ti stacks using variable feedrate. Composites: Part B, 52:303-310.

[23]. Buscarello, R.T. (2002) Practical solutions to machinery and maintenance vibration problems. 4th ed. Online text book: Update International.

[24]. Giancoli, D.C. (1989) Physics for scientists and engineers with modern physics. 2nd ed. New jersey: Prentice Hall.

[25]. He, J.; Fu, Z.F. (2001) Modal Analysis. 1st ed. Jordan Hill, Oxford: Butterworth-Heinemann.

[26]. Weiss, H.K. (1938) Errors of the dial gauge as an instrument for measuring amplitudes of vibration. Review of Scientific Instruments, 9:365-369.

[27]. Sang, D.; Jones, G.; Chadha, G.; Woodside, R. (2014) Cambridge international AS and A level physics. 1st ed. Cambridge, United Kingdom: University Printing House.

[28]. Liu, Y.; Chen, W.; Liu, J.; Shi, S. (2011) A cylindrical standing wave ultrasonic motor using bending vibration tranducer. Ultrasonics, 51:527-531.

[29]. Nishimura, T.; Hosaka, H.; Morita, T. (2012) Resonant-type smooth impact drive mechanism actuator using a bolt-clamped langevin transducer. Ultrasonics, 52:75-80.

Chapter 6 - Conclusions and contributions

6.1 Conclusions

In this dissertation, difficult-to-machine materials including CFRP composites, K9 glass, rocks (travertine, marble, and basalt), and titanium had been drilled by rotary ultrasonic machining. The summary of the investigations presented in this dissertation are shown in Figure 6.1.

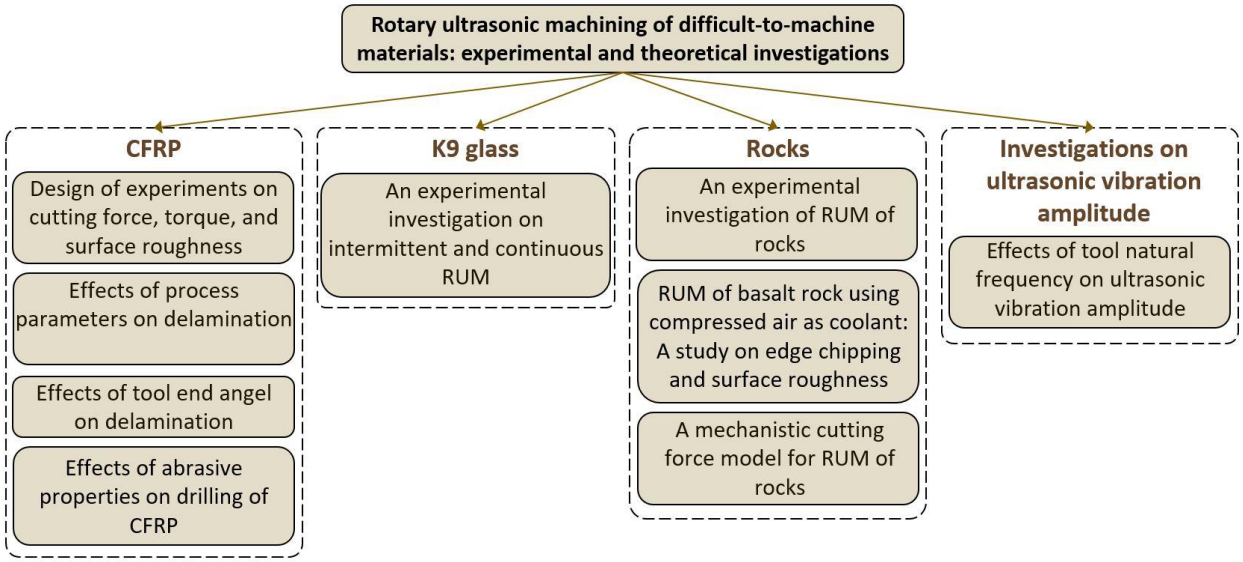

Figure 6.1 Summary of the studies of this dissertation

The following conclusions are drawn from this dissertation.

1. When RUM of CFRP, higher tool rotation speed, lower ultrasonic power, and lower abrasive size and concentration led to smaller cutting force and surface roughness decreased as feedrate increased. Use of backing plate under the exit surface prevented delamination completely and reduced feedrate at the exit surface benefitted to decrease delamination. Positive tool end angle was the best tool end angle to reduce delamination with respect to zero and negative tool end angles. The average surface roughness at the exit of a drilled hole on CFRP was always greater than that at the entrance.

2. When RUM of K9 glass, intermittent RUM led to a lower cutting force than using continuous RUM and chipping size in intermittent RUM was smaller than that in continuous RUM when other input variables stayed constant. It was found that higher cutting force resulted in a larger chipping size, and this relationship was close to linear.
3. Investigations on RUM of rocks demonstrated that RUM is capable of drilling hard rocks with a feedrate comparable to that of existing drilling procedures. A higher feedrate and larger drill bit diameter led to a higher cutting force. When RUM of basalt and marble, an abrasive concentration of 100 gave the lowest cutting force and cutting force decreased as tool rotation speed increased. Higher feedrate and higher ultrasonic power led to a larger torque. The surface roughness (R_a) at the exit of the drilled holes had larger R_a values compared to that at the entrance and higher feedrate led to a higher surface roughness. The increase of the tool rotation speed had a tendency to decrease the average edge chipping thickness and maximum edge chipping diameter.
4. A physics-based mechanistic model to predict the cutting force for RUM of rocks was developed considering the ductile mode and brittle fracture mode removal of rock under the indentation of a single abrasive particle and input variables. It could be concluded that cutting force increased as feedrate, mesh size, abrasive concentration, and tool size increased and cutting force decreased as tool rotation speed and ultrasonic vibration amplitude increased.
5. The investigation of the effects of tool natural frequency on ultrasonic vibration amplitudes in rotary ultrasonic machining was carried out to explain a reported observation that ultrasonic vibration amplitude differs by tools at the same ultrasonic power level. The study found out that a tool with a natural frequency closest to the input frequency (20 kHz) of the ultrasonic

power supply generates the highest ultrasonic vibration amplitude on every ultrasonic power level.

6.2 Contributions of this dissertation

The major contributions of this dissertation are:

1. This research presented studies on RUM of CFRP: the effects of input variables (machine variables and abrasive properties) on cutting force, torque, and surface roughness; the effects of tool end angles on delamination; and use of backing plate to eliminate delamination.
2. This research conducts intermittent RUM on K9 glass, and compares its performance against continuous RUM from the perspectives of cutting force, surface roughness, and chipping size.
3. This research reports feasibility and experimental studies on RUM of natural rocks, which are inhomogeneous materials, studies on edge chipping and surface roughness in RUM of basalt rock using cold compressed air as coolant, and developed a cutting force model for rotary ultrasonic machining of rock considering the ductile mode removal and brittle fracture mode removal of rock under the indentation of a single abrasive particle and input variables.
4. This research provides an explanation to the observation, different tools show different vibration amplitudes on the same ultrasonic power level, and verification of measurement methods, and also to guide tool design and selection in RUM.

Appendix A - Publications during Ph.D. research

Journals and transactions

1. **Fernando, P.**, Zhang, M., Pei, Z., 2019, "Rotary Ultrasonic Machining: Effects of Tool Natural Frequency on Ultrasonic Vibration Amplitude," Machining Science and Technology, Vol. 23, pp. 595-611.
2. **Fernando, P.**, Zhang, M., Pei, Z., 2018, "Rotary Ultrasonic Machining of Rocks: An Experimental Investigation," Advances in Mechanical engineering, Vol. 10, pp. 1-9.
3. **Fernando, P.**, Zhang, M., Pei, Z., Cong, W., 2017, "Intermittent and Continuous Rotary Ultrasonic Machining of K9 Glass: An Experimental Investigation," Journal of Manufacturing and Materials Processing, Vol. 1, pp. 20.
4. Ning, F., Wang, H., Cong, W., **Fernando, P.**, 2017, "A mechanistic ultrasonic vibration amplitude model during rotary ultrasonic machining of CFRP composites," Ultrasonics, Vol. 76, pp. 44-51.
5. Wang, H., Ning, F., Hu, Y., **Fernando, P.**, Pei, Z., Cong, W., 2016, "Surface grinding of carbon fiber–reinforced plastic composites using rotary ultrasonic machining: effects of tool variables," Advances in Mechanical Engineering, Vol. 8.

Proceedings

6. **Fernando, P.**, Zhang, M., Pei, Z., Owns, A., 2018, "Rotary Ultrasonic Machining of basalt rock using compressed air as coolant: A study on edge chipping and surface roughness," ASME 2019 14th International Manufacturing Science and Engineering conference, Vol. 1.

7. **Fernando, P.**, Zhang, M., Pei, Z., 2018, "Rotary Ultrasonic Machining of CFRP: Effects of abrasive properties," ASME 2018 13th International Manufacturing Science and Engineering conference, Vol. 1.
8. **Fernando, P.**, Zhang, M., Pei, Z., Cong, W., 2017, "Rotary Ultrasonic Machining: Effects of Tool End Angle on Delamination of CFRP Drilling," ASME 2017 12th International Manufacturing Science and Engineering conference, Vol. 1.
9. **Fernando, P.**, Pei, Z., Zhang, M., Song X., 2016, "Rotary Ultrasonic Drilling of CFRP: Effect of Process Parameters on Delamination," ASME 2016 11th International Manufacturing Science and Engineering conference, Vol. 1.
10. **Fernando, P.**, Zhang, M., Pei, Z., Cong, W., Song, X., 2015, "Rotary Ultrasonic Machining of Carbon Fiber Reinforced Plastics: A Design of Experiment," ASME 2015 10th International Manufacturing Science and Engineering conference, Vol. 1.

Submitted to journals and transactions

11. **Fernando, P.**, Zhang, M., Pei, Z., 2020, "Mechanistic cutting force model for rotary ultrasonic machining of rocks," Submitted to The International Journal of Advanced Manufacturing Technology.
12. Parandoush, P.†, **Fernando, P.**†, Zhang, M., Lin, D., 2019, "Ultrasonic Drilling of Additively Manufactured Continuous Carbon Fiber Reinforced Polymers: A Finishing Process," Submitted to Rapid Prototype Journal.

Posters

13. “Rotary Ultrasonic Machining of rocks: Effects of machining variables on cutting force”, Poster presentation at ASME 2018 13th International Manufacturing Science and Engineering conference.
14. “Rotary Ultrasonic Machining: Effects of Tool Natural Frequency on Ultrasonic Vibration Amplitude”, Poster presentation at ASME 2017 12th International Manufacturing Science and Engineering conference.
15. “Rotary Ultrasonic Machining: Effects of Tool Natural Frequency on Ultrasonic Vibration Amplitude”, Poster presentation at 2017 Open house, Department of Industrial and Manufacturing Systems Engineering, Kansas State University.
16. “Rotary Ultrasonic Drilling of CFRP: Effect of Process Parameters on Delamination”, Poster presentation at ASME 2016 11th International Manufacturing Science and Engineering conference.
17. “Effects of Tool Design on Delamination in Rotary Ultrasonic Drilling of CFRP”, Poster presentation at ASME 2015 10th International Manufacturing Science and Engineering conference.